



Alexander Fröhlich, B.Sc.

Non-invasive sensor prototype for flux measurement in power transformers

MASTERARBEIT

zur Erlangung des akademischen Grades

Diplom-Ingenieur

Masterstudium Elektrotechnik

eingereicht an der

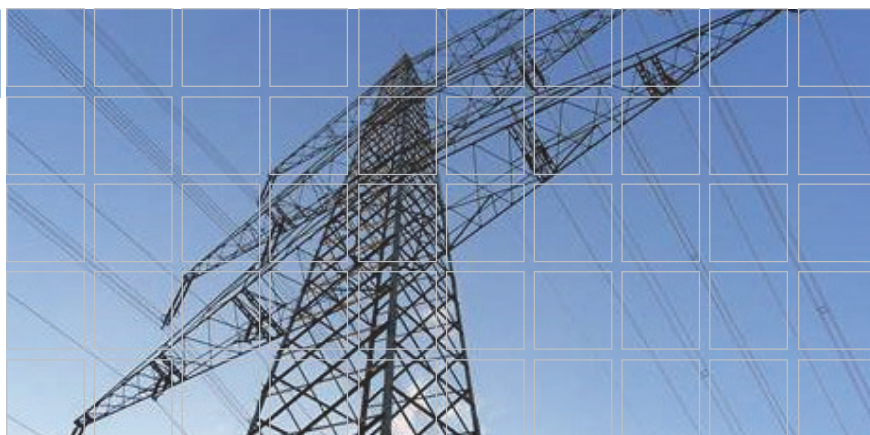
Technischen Universität Graz

Betreuer

Ao.Univ.-Prof. Dipl.-Ing. Dr.techn. Herwig Renner

Institut für Elektrische Anlagen und Netze

Dr.techn. Dennis Albert, B.Sc. M.Sc.



Non-invasive sensor prototype for flux measurement in power transformers

A Master thesis by
Alexander Fröhlich, B.Sc.

Supervisor
Dr.techn. Dennis Albert, B.Sc. M.Sc.

Reviewer
Ao.Univ.-Prof. Dipl.-Ing. Dr.techn. Herwig Renner

April 2023

Graz University of Technology
Institute of Electrical Power Systems
Inffeldgasse 18/I
8010 Graz
Austria

Head of Institute

Univ.-Prof. DDipl.-Ing. Dr.techn. Robert Schürhuber

Reviewer

Ao.Univ.-Prof. Dipl.-Ing. Dr.techn. Herwig Renner

Supervisor

Dr.techn. Dennis Albert, B.Sc. M.Sc.

A Master thesis by
Alexander Fröhlich, B.Sc.

April 2023

Acknowledgements

At the beginning, I would like to thank all those who supported and motivated me during the completion of this master's thesis.

My deepest gratitude goes to my supervisor, Dr.techn. Dennis Albert, for his support and helpfulness at all times of the day. Your irreplaceable advice and expertise have been of essential importance to this work. Furthermore, I would like to thank you for giving me the opportunity to work on the neutral point project as a student project assistant at the Institute for Electrical Power Systems. At this point, I would also like to thank all colleagues of the project for the warm welcome, support, and the good atmosphere among you.

Many thanks also to Prof. Dr.techn. Herwig Renner for grading and supervising this master thesis and for the professional feedback, which made new approaches to problems possible.

I would like to express my heartfelt thanks to my parents for their continuous love and support, without which this study would not have been possible. Your confidence in me and my abilities have been a constant source of motivation. A special thanks to my girlfriend Chiara for your exerted patience during my studies and support during mathematical challenges.

Last but not least, I would like to thank all my fellow students and friends who made this study period an unforgettable memory.

Danksagung

Zu Beginn möchte ich mich bei all denjenigen bedanken, die mich während der Anfertigung dieser Masterarbeit unterstützt und motiviert haben.

Mein aufrichtiger Dank gebührt meinen Betreuer Dr.techn. Dennis Albert, für seine Unterstützung und Hilfsbereitschaft zu jeder Tageszeit. Deine unersetzlichen Ratschläge und Expertise waren von entscheidender Bedeutung. Außerdem möchte ich mich bei Dir bedanken, dass Du mir die Chance gegeben hast, am Institut für Elektrische Anlagen und Netze als studentischer Projektmitarbeiter am Sternpunktprojekt mitzuarbeiten. An dieser Stelle auch ein Dank an alle Kollegen des Projekts, für die herzliche Aufnahme, Unterstützung und der guten Atmosphäre unter Euch.

Herzlichen Dank auch an Prof. Dr.techn. Herwig Renner für die Benotung und Übernahme dieser Masterarbeit und für das fachliche Feedback, welches neue Ansätze bei Problemen ermöglicht hat.

Weiters möchte ich meinen herzlichen Dank an meine Eltern aussprechen, für eure unerschütterliche Liebe und Unterstützung, ohne welcher dieses Studium nicht möglich gewesen wäre. Euer Vertrauen in mich und meine Fähigkeiten war eine ständige Quelle der Motivation. Ein besonderer Dank gilt meiner Freundin Chiara, für deine aufgebrachte Geduld während des Studiums und Unterstützung bei mathematischen Herausforderungen.

Zu guter Letzt möchte ich mich bei allen Kommilitonen und Freunden bedanken, welche diese Studienzeit zu einer unvergesslichen Erinnerung gemacht haben.

Eidesstattliche Erklärung

Ich erkläre an Eides statt, dass ich die vorliegende Arbeit selbstständig verfasst, andere als die angegebenen Quellen/Hilfsmittel nicht benutzt, und die den benutzten Quellen wörtlich und inhaltlich entnommenen Stellen als solche kenntlich gemacht habe. Das in TUGRAZonline hochgeladene Textdokument ist mit der vorliegenden Masterarbeit identisch.

Affidavit

I declare that I have authored this thesis independently, that I have not used other than the declared sources/resources, and that I have explicitly indicated all material which has been quoted either literally or by content from the sources used. The text document uploaded to TUGRAZonline is identical to the present master's thesis

14.04.2023

Datum

Fröhlich Alexander

Unterschrift

Abstract

The master thesis deals with the investigation of a non-invasive sensor prototype, for the measurement of alternating and constant magnetic fluxes in power transformers. The sensor is placed between two legs on the yoke of a transformer. It experiences part of the transformer main and leakage flux and can infer the magnetic flux using the fluxgate principle. The construction, testing, and verification of the sensor are covered in the thesis. For the realization of the sensor an electronic circuit is designed, moreover, two different core materials for the sensor are compared. The applied core material and the geometrical dimensions of the sensor are of crucial importance for proper operation. A necessary signal processing is carried out by an electronic circuit, which enables the recording of the measured quantity in the laboratory. Finally, the sensor is tested on a 60 kVA five-leg transformer with superimposed direct current. The measurement of direct and alternating magnetic fluxes in the transformer core could be successfully determined. The sensor must, however, be calibrated to the specific transformer, in order to provide an accurate and absolute indication of the magnetic flux. The advantage of this sensor, compared to conventional measurement methods, is that the transformer does not have to be energized. Which allows measuring pure constant flux or remanence. The thesis also includes the experience gained during the engineering and measurement process.

Kurzfassung

Die Masterarbeit behandelt die Untersuchung eines nicht-invasiven Sensor Prototypen, zur Messung von alternierenden und konstanten magnetischen Flüssen in Leistungstransformatoren. Der Sensor wird dazu zwischen zwei Schenkeln auf dem Joch eines Transformators platziert. Dieser erfährt einen Teil des Transformator Haupt- und Streufluss und kann mithilfe des Fluxgate Prinzips auf den magnetischen Fluss rückschließen. Der Aufbau, die Testung und Verifikation des Sensors werden in der Arbeit behandelt. Zur Verwirklichung des Sensors wird im ersten Schritt eine elektronische Schaltung entworfen, weiters werden zwei verschiedene Kernmaterialien für den Sensor verglichen. Das verwendete Kernmaterial und die geometrischen Abmessungen des Sensors sind von entscheidender Bedeutung für eine korrekte Funktionsweise. Eine notwendige Signalverarbeitung wird durch eine elektronische Schaltung durchgeführt, welche die Aufzeichnung der Messgröße im Labor ermöglicht. Abschließend wird der Sensor auf einem 60 kVA fünf-Schenkel Transformator mit überlagertem Gleichstrom getestet. Die Messung von direkten und alternierenden magnetischen Flüssen im Transformator Kern konnte erfolgreich durchgeführt werden. Der Sensor muss jedoch auf den verwendeten Transformator kalibriert werden, um eine absolute Aussage über den magnetischen Fluss zu ermöglichen. Der Vorteil dieses Sensors ist, im Vergleich zu herkömmlichen Messmethoden, dass der Transformator nicht eingeschalten sein muss, um Gleichflüsse oder Remanenz zu messen. Die Arbeit beinhaltet zudem die Erfahrungswerte, die während des Aufbaus und den Messungen errungen wurden.

List of abbreviations

AC	alternating current
ADC	analog digital converter
APG	Austrian Power Grid
DC	direct current
EMC	electromagnetic compatibility
EMF	electromotive force
FEM	finite elements method
FPGA	field programmable gate array
GIC	geomagnetically induced current
GND	ground
GUI	graphical user interface
IC	integrated circuit
LED	light emitting diode
LUT	lookup table
MCU	micro-controller unit
MOSFET	metal-oxide-semiconductor field-effect transistor
OPAMP	operational amplifier
PCB	printed circuit board
PWM	pulse width modulation
RMS	root mean square
SCADA	supervisory control and data acquisition
SiC	silicon carbide
SFRA	sweep frequency response analysis
SMD	surface mounted devices
TVS	transient voltage suppressor
VNA	vector network analyzer

List of Symbols

A	transfer function
A_{fe}	cross section of core
A_L	inductance per turn
A_r	gain factor of filter
B	magnetic flux density
B_{ext}	external magnetic flux density
B_{fr}	bandwidth of bandpass filter
B_s, B_{sat}	saturation flux density
C	capacitor
C_b	boot capacitor
C_g	gate capacitor
C_l	load capacitor
C_s	stray capacitor
E	electric field strength
E_{cap}	stored energy in capacitor
E_L	stored energy in inductance
F	Lorentz force
f	frequency
f_c	cutoff frequency
$f_{excitaiton}$	excitation frequency
H	magnetic field strength
H_f	saturation field strength of ferrite core material
H_m	amplitude of magnetic field strength
H_n	saturation field strength of nanocrystalline core material
H_s	saturation field strength
I	current
I_1	primary side current
I_2	secondary side current
I_{DC}	superimposed direct current
I_h	Hall current
I_{m1}	magnetization current
I_{supply}	supply current
j	imaginary number

L	inductance
l_{airgap}	height of air gap
l_{fe}	length of magnetic path
l_{lv}	length of magnetic path of low-voltage winding
L_{sensor}	inductance of sensor
l_{sensor}	length of magnetic path inside sensor rod
$l_{\text{transformer,section}}$	length of magnetic path inside transformer core
n	number of turns
$n_1, n_p, n_{\text{transf.,lv}}$	number of turns primary side
n_2, n_s	number of turns secondary side
$n_{\text{excitation}}$	number of turns excitation coil
P_1	power losses
Q	quality factor
q	particle of charge
R	resistance
R_m	reluctance
$R_{m,\text{air}}$	reluctance of air gap
$R_{m,\text{sensor}}$	reluctance of sensor rods
$R_{m,\text{transformer,section}}$	reluctance of transformer section
R_{sensor}	resistance of sensor
s_n	complex variable of Laplace function
t	time
$t_{\text{excitation}}$	excitation time of the sensor
T_p	pulse width of excitation frequency
v	velocity of charge
V	voltage
V_{CC}	semiconductor supply voltage
V_{in}	input voltage
$V_{\text{ind}}, V_{\text{induced}}$	induced voltage
V_h	Hall voltage
V_{out}	output voltage
$V_{\text{sensor,AC}}$	processed output voltage of fluxgate sensor which represents the alternating 50 Hz magnetic flux amplitude
$V_{\text{sensor,DC}}$	processed output voltage of fluxgate sensor which represents the directional magnetic flux amplitude
V_{supply}	supply voltage
V_{source}	source voltage

X	reactance
$X_{1,\sigma}$	leakage reactance primary side
$X_{2,\sigma}$	leakage reactance secondary side
X_{m1}	main reactance
Z	impedance
Z_{imag}	imaginary part of impedance
Z_{real}	real part of impedance
Z_{sensor}	impedance of sensor
μ_0	magnetic permeability in vacuum
μ_r	relative permeability
τ_{sensor}	time constant of sensor
φ	phase shift
ϕ	magnetic flux
ϕ_{rod}	magnetic flux inside sensor rod
ω	angular frequency
ω_r	ressonance angular frequency

Contents

1	Introduction	1
1.1	Motivation	1
1.2	Objective of the Thesis	1
1.3	Organisation of the Thesis	2
2	Theory	3
2.1	Flux measure Technologies in Power Transformers	3
2.1.1	Saturation Detection	4
2.1.2	Dynamic Flux Measurement	5
2.1.3	Continuous Flux Measurement	5
2.1.4	Direct Current Compensation	9
2.2	Fluxgates	10
2.2.1	Fluxgate Principle	10
2.2.2	Non-linear Measurand at the Intermediate Main and Leakage Flux	12
2.2.3	Calculation of external Field	13
2.2.4	Auxiliary Core Design	15
3	Sensor Design	17
3.1	Core Materials and Sensor Coils	20
3.2	Electronic Design	27
3.2.1	H-Bridge	27
3.2.2	Signal processing	37
3.3	Improvements	42
3.4	Prototype PCB	44
4	Sensor Proof-of-concept Laboratory Test	46
4.1	Measurement Setup	46
4.2	Ramp superimposed DC Test	48
4.3	Long superimposed DC Test	49
5	Conclusion and Outlook	54
5.1	Conclusion	54
5.2	Future Research and Improvements	54
A	Circuit schematic and electronic components	58
A.1	Supply Board	58
A.2	H-bridge Board	59
A.3	Signal Processing Board	60
A.4	Symmetrical Voltage Supply Board	61

A.5 Electrical Components	62
B Datasheet	63
C Programming	64

1 Introduction

1.1 Motivation

Due to the energy transition and the resulting increased use of power electronics, direct currents (DCs) can occur more and more frequently in the European interconnected grid. DCs can cause a positive or negative offset or an increasing amplitude of the alternating flux in the transformer core. Recently, the activity in the research topic of direct currents and induced direct magnetic fluxes and their effects on transformers has increased. The origin of these additional DC currents is investigated in more detail and attempts are made, to reduce magnetic fluxes in transformers or to increase their resilience against these currents. [1, 2]

External caused magnetic fluxes inside transformer cores are manifested by a distortion of the current and voltage waveforms, higher sound emissions, and a higher reactive power demand. At very high DCs, it is also possible, that the transformer core becomes deeply saturated and thus the power transmission is reduced to a minimum and can also be destroyed under certain circumstances [3].

There are different methods to measure a magnetic flux inside a transformer core. It can be distinguished whether a sensor can only detect the presence of flux or saturation, or whether it is able to measure the flux. The majority of measurement methods can only detect or measure an alternating flux and only a few can measure a direct flux. Using the fluxgate principle, a sensor is developed in this thesis that is able to measure alternating, direct and remanent flux. Fluxgate technologies have so far mainly been used in space science and geophysics to determine the position of satellites via the earth's magnetic field [4]. The fluxgate principle is also commonly used by sensors for current measurement in conductors. Since this is a non-invasive measurement method, the magnetic and mechanical properties of the transformer core are not affected.

With the use of flux monitoring an active flux reduction can be realized. Through constant flux reduction, the previously mentioned effects can be reduced and grid operators can rely on higher reliability. It is suspected that the life expectancy of this power equipment increases. This project verifies the possibility to use Fluxgates also for magnetic flux measurements in transformers.

1.2 Objective of the Thesis

The aim of this thesis is to develop a non-invasive sensor that can be placed between two legs on a transformer yoke. The intention is to test whether the fluxgate principle can or cannot be used to measure directional and alternating magnetic fluxes in transformer cores, due to a superimposed current between two neutral points. The measured signal can be used to infer the direct magnetic flux with the aid of synchronous demodulation (Chapter 3.2.2) and an alternat-

ing magnetic flux (if the frequency is known) is inferred with the aid of a bandpass filtering. In the first step, a prototype circuit board is developed, which is able to generate an excitation current to saturate the sensor rods in such a way that they are periodically reaching positive and negative saturation. Two different ferromagnetic materials are investigated in order to enable an optimal signal output and with regard to future applications in transformers.

In addition, analog signal processing is implemented on the board, which allows displaying the signals with the help of a mixed signal power analyzer directly in the laboratory. A proof-of-concept test in the laboratory is performed, where two transformers are connected in series and a superimposed DC through the neutral points is applied. The correct sensor operation is discussed and the gained experience during engineering and measurements in the laboratory is shown.

This thesis does not discuss the improvement of the excitation electronics or the signal processing improvement of fluxgate sensors. Also, the exact influence of superimposed direct currents on transformers is not covered.

1.3 Organisation of the Thesis

This thesis is divided into four chapters as follows:

In the **second chapter**, an overview of different magnetic flux measurement methods in transformers is presented. The fluxgate principle used in this work is explained and the mathematical derivation of the measured signal is derived. In addition, the necessary conditions for the realization of the sensor are described.

The **third chapter** deals with the suitable selection of ferromagnetic cores and a suitable electronic design, to provide an excitation current and analysis of the sensor. The necessary signal processing is explained to obtain the information for the directly proportional signal of the magnetic flux out of the measurement voltage waveform. In addition, improvements during the engineering are discussed.

In the **fourth chapter**, the proof-of-concept laboratory test is performed. For this purpose, the measurement setup with two transformers and the superimposed DC is explained. This is followed by an overview of the measured signal waveforms and their interpretation.

The **fifth chapter** is about the conclusion of the thesis and some improvements to the further development of the sensor.

2 Theory

In the high voltage transmission system in Europe, the neutral point of transformers must be grounded in order to generate a high error current in the event of a fault and thus be able to detect it quickly. Grounding allows DCs to flow across the transformer, which can cause a directional flux inside the transformer core [5]. The use of grain-oriented steel sheets as core material also increases the susceptibility of the transformers to low amplitude DCs [6].

Causes for the occurrence of direct currents can originate from power electronics. This is due to unbalanced switching times of semiconductors, component properties, and a too small difference between the trigger frequency of the pulse width modulation (PWM) and the required frequency of the output voltage/current. [7] Another origin is where power lines are oriented in the direction of the earth's magnetic field, which can also induce currents inside the grid. [8]

DCs can also be caused by earth magnetic field changes, affected by the solar activity of the sun. They are called geomagnetically induced currents (GICs). Charged particles of solar flares compress and stretch the earth's magnetic field, which causes induced currents in the grid infrastructure. In addition, DCs inside the grid can occur after switching operations in power grids or through the supply of public transport systems, such as subways or trains [9]. Further information about this topic is given in [10].

DC biasing can cause the following impacts:

- higher environmental sound,
- lowered power factor, due to core saturation,
- half-cycle-saturation and the resulting distortion of the current and voltage waveforms,
- higher core losses → heating of the core and coils.

Currently, it is not common practice to continuously monitor the directional flux inside transformer cores. The flux distribution is only determined offline, using Epstein frames, single sheet measurements, or finite elements method (FEM). [11]

2.1 Flux measure Technologies in Power Transformers

Various methods have been explored for determining or measuring the magnetic flux within a transformer core. The flux measurement methods can be divided into three categories: saturation detection, dynamic flux monitoring, and continuous flux measurement. An overview is shown in Figure 1.

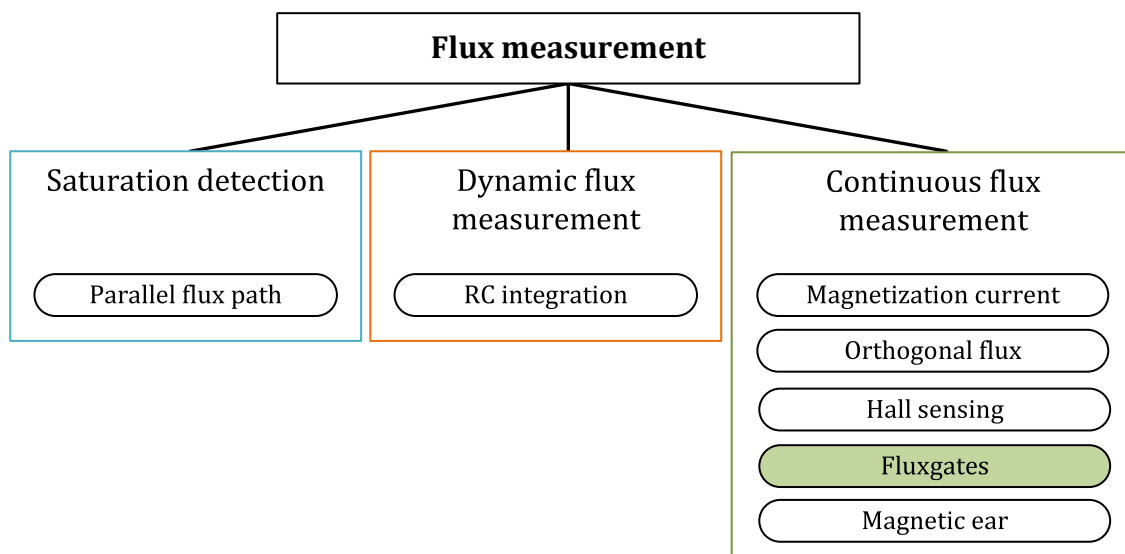


Figure 1: Overview of flux sensing methods adopted from [7].

2.1.1 Saturation Detection

There are two ways to detect core saturation. For this purpose, two E-shaped cores are placed on top of each other for a single-phase transformer. A schematic diagram is shown in Figure 2 a.). The primary and secondary windings are located on the middle leg. The left leg closes the magnetic circuit during operation in the quasi-linear section of the hysteresis curve. The right leg has a small air gap and a pickup winding. When the transformer reaches saturation, a larger part of the flux will also go through the right leg and over the air gap. This flux induces a voltage V_i across the sense coil. [7]

Another way to detect a saturation state is to create an additional magnetic path by means of U-shaped cores in the direction of the transformer core. This is shown schematically on the yoke of the transformer in Figure 2 b.). It requires removing a part of the transformer core below the U-cores to increase the cross-sectional area. As a result, this area saturates faster compared to the rest of the core. The flux must therefore move into the U-core and subsequently leads to an induced voltage V_i in the pickup coil. [7]

These methods only allow determining whether the transformer core is in saturation or not. This is not sufficient for a possible DC flux measurement and subsequently balancing application.

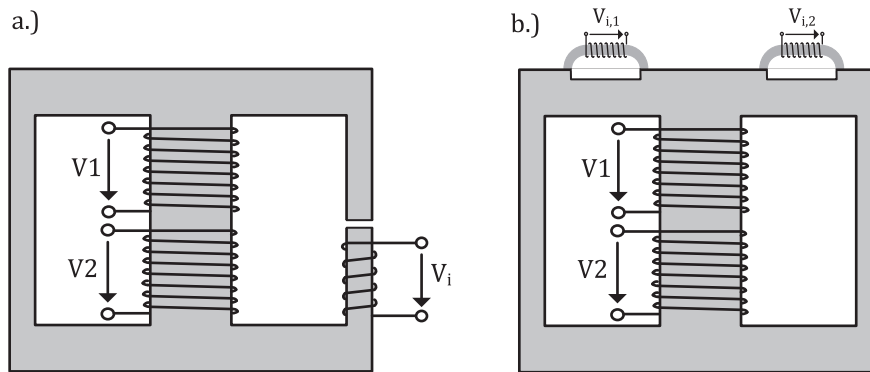


Figure 2: Schematic of saturation detection adopted from [7].

2.1.2 Dynamic Flux Measurement

The dynamic flux measurement is used to detect differences in flux loading by integrating the supply voltage of the transformer. The integration can be implemented using passive or active components. A schematic representation of an active integration is shown in Figure 3. A disadvantage of this method is that only flux changes are detectable and no static nor remanent flux. [12]

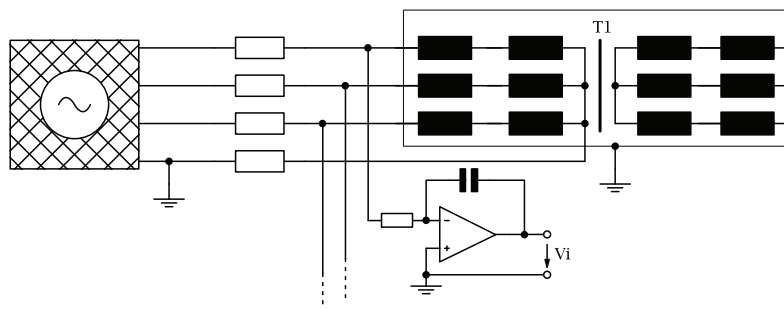


Figure 3: Schematic of dynamic flux measurement.

2.1.3 Continuous Flux Measurement

In order to continuously measure and monitor the desired and undesired magnetic flux inside a transformer core, the following methods are developed. These would also provide a sufficient measuring signal for the implementation of a flux balancing system.

Magnetization Current

The magnetization current \underline{I}_{m1} can be used to make a statement about the magnetic flux density inside the transformer core. This current can be calculated using the basic equivalent circuit diagram of a transformer, shown in Figure 4. The resulting primary and secondary voltages are $\underline{V}_1, \underline{V}_2$, Equation 1. The current \underline{I}_0 calculates by the subtraction of the primary current \underline{I}_1 and the secondary current \underline{I}'_2 . The magnetization current \underline{I}_{m1} itself calculates with the vectorial relation Equation 3. n_1 and n_2 are the number of turns of the primary and secondary side respectively. Further information can be found in [12, 13].

$$\underline{V}_1 = (R_1 + jX_{1\sigma})\underline{I}_1 + \frac{(R_{fe} \cdot jX_{m1})}{(R_{fe} + jX_{m1})}\underline{I}_0 \quad (1)$$

$$\underline{V}_2 = (R'_2 + jX'_{2\sigma})\underline{I}'_2 + \frac{(R_{fe} \cdot jX_{m1})}{(R_{fe} + jX_{m1})}\underline{I}_0$$

$$\underline{I}_0 = \underline{I}_1 - \underline{I}_2 \frac{n_1}{n_2} \quad (2)$$

$$\underline{I}_{m1} = \sqrt{\underline{I}_0^2 - \underline{I}_{fe}^2} \quad (3)$$

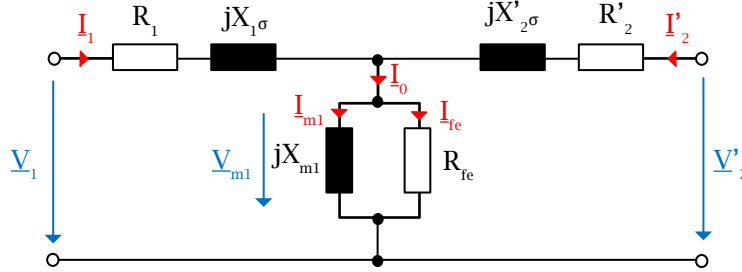


Figure 4: Basic transformer equivalent circuit.

Another method of measuring magnetizing current is shown in Figure 5 a.). An additional toroidal core with primary and secondary winding using the same winding ratio as for the large transformer is utilized. One of the two windings has a reversed winding sense. This allows the flux inside the toroid to be zero at a symmetrical load. If this symmetry is no longer given, e.g. due to a direct flux in the transformer, a voltage V_i is induced in the pickup coil. The downside of this technique is the enormous amount of material required for power transformers and the complex insulation. The advantage is that the sensor can be used for directional flux measurement. [7, 14, 15]

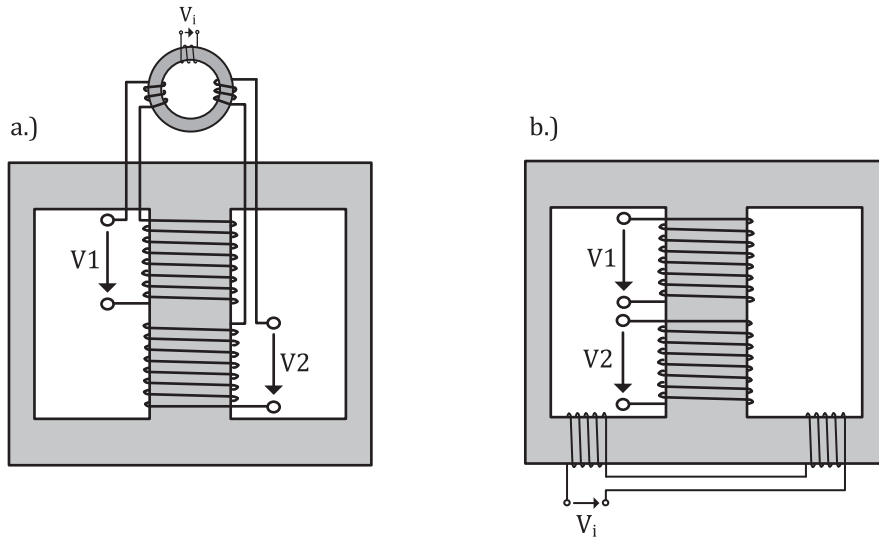


Figure 5: Schematic of continuous flux sensing methods adopted from [7].

Orthogonal Flux

The flux within a transformer core can also be determined with the help of an additional winding that is orthogonal to the main winding. In the additional winding a DC current I_o is injected which causes an orthogonal flux Φ_o in the core, schematically shown in Figure 6. Due to the orthogonality between the additional winding and the main flux, no voltage is induced. If the main flux Φ_m increases so that the core material reaches saturation, the BH properties of the core material are changing. This change will also be experienced by the additional winding and result in an induced voltage V . The disadvantage of this method is that only changes of the main flux Φ_m in the non-linear region of the hysteresis curve lead to an induced voltage V in the orthogonal winding. [7, 16, 17]

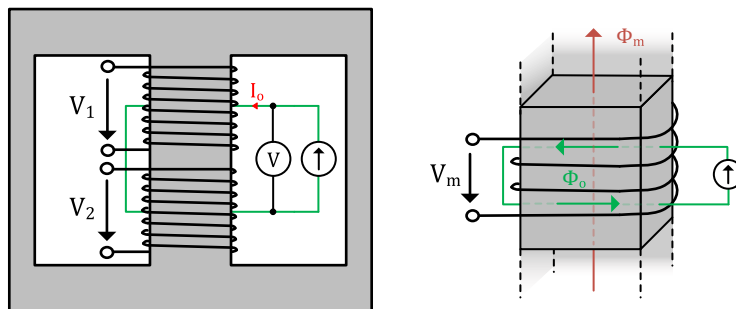


Figure 6: Schematic of orthogonal flux.

Hall sensing

Hall sensors are commonly used for current measurement by measuring the magnetic field of a current-carrying conductor. On charge carriers q , which move in a magnetic field B , the Lorentz force F acts (Equation 4). The Hall effect states that through the deflection of the charge carriers q a Hall voltage V_h is generated. n represents the charge carrier density and d the thickness of the element, as depicted in Equation 5. [18]

$$\mathbf{F} = q(\mathbf{E} + \mathbf{v} \times \mathbf{B}) \quad (4)$$

$$V_h = \frac{I_h B}{n \cdot d} \quad (5)$$

Hall elements (Figure 7 a.) can also be used for flux measurement in a transformer core by placing them in an air gap, as schematically shown in Figure 7 b.). The disadvantage of this method is the creation of an additional air gap, which increases the reluctance of the whole transformer core. Hall elements are also very temperature-dependent and must be temperature corrected, since the magnetic flux of the magnetic core increases with higher iron losses, resulting in higher temperatures.

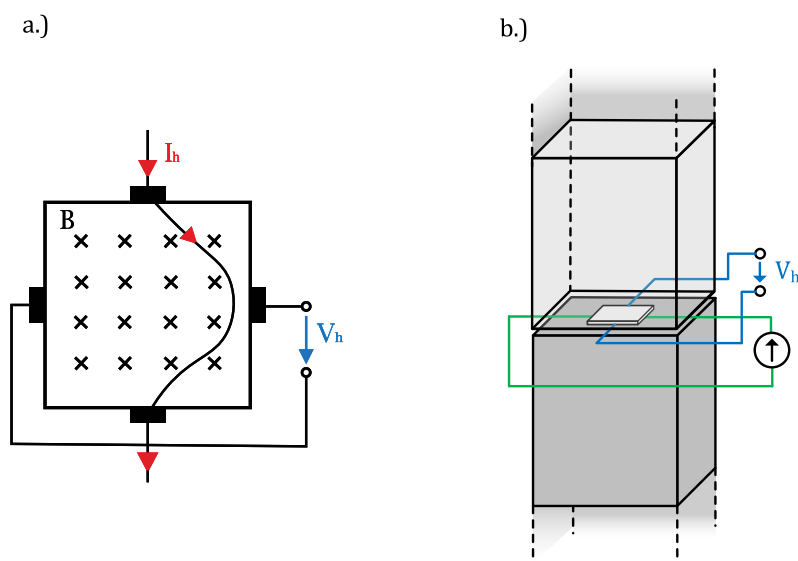


Figure 7: Schematic of hall effect sensor adopted from [18] and sensor application inside magnetic cores.

Fluxgates

Fluxgates are capable of vectorial magnetic field measurement. They are also frequently used for current measurements. In Figure 5 b.), a method for measuring a direct magnetic flux is shown. For this purpose, the primary and secondary windings of a transformer are attached to the center leg. On both yokes, two windings are attached in different winding directions. A direct flux in the transformer core would change the inductance between the two terminals. By measuring the inductance, the direct flux can be determined. [7]

In this thesis, a different fluxgate method is used, which allows inferring the DC flux by two additional U-shaped cores, which are periodically driven into positive and negative saturation. For more information see Chapter 2.2.

Magnetic Ear

The magnetic ear method was presented in [7]. For this purpose, an external U-shaped core with additional winding is placed on the main core. The two magnetic cores share the reluctance R_m , as shown in Figure 8. Changing the magnetic flux in the main core leads to a change in the inductance of the additional U-shaped core and the winding. The change in inductance is measured using an electronic circuit. The measurement signal V_1 provides a direct statement about the main magnetic flux.

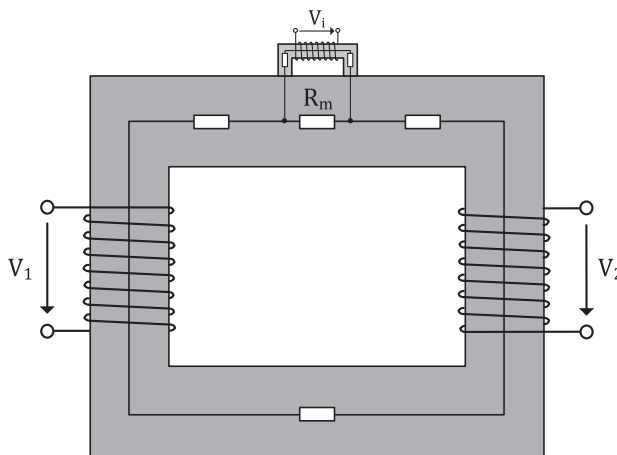


Figure 8: Schematic of magnetic ear adopted from [7].

2.1.4 Direct Current Compensation

Knowing the actual direct and alternating flux within transformers provides significant benefits. For example, a constant flux inside the core can be reduced. There are different types of flux balancing, as follows:

- (1.) passive control,
- (2.) saturation correction,
- (3.) active control. [7]

One method is the direct current compensation, which belongs to the category: active control. By adding an additional winding and a control system that delivers current surges through the coil, the direct flux inside the transformer core can be reduced. The pulses cause a magnetic flux in the opposite direction which counteracts the flux to be decreased. This method was patented by [19]. It is used in a five-leg 400/110/30 kV 300 MVA transformer in the substation Zurdorf of the Austrian Power Grid (APG) [10]. The flux reduction only works with an energized transformer, therefore a reduction of a remanent flux is not possible.

2.2 Fluxgates

Fluxgate sensors or also called Fluxgates are devices sensitive to the influence of external magnetic fields applied to the sensor. They consist of ferromagnetic cores, in this case of two sensor rods with at least two coils, the excitation coil and the pickup coil. The excitation coil is excited with an alternating current and the pickup coil generates an electromotive force (EMF) proportional to the external field. An additional winding is called the feedback coil which is explained in Chapter 5. Fluxgates are a kind of active transformers, which are operated with two magnetic fields within the cores. First with the external magnetic field applied to the sensor, for example, the earth magnetic field or the stray field of transformers, coils, etc. The fields to be measured are either constant or change at a low frequency. On the other hand, the Fluxgates are operated with the higher changing field produced by the excitation current. Across the sense, also called pickup coil, an EMF is generated, which depends on the counteraction of the two magnetic fields inside the ferromagnetic cores. Through the induced voltage it is possible to infer the external magnetic field. [4]

2.2.1 Fluxgate Principle

Without an external field, there is no induced voltage across the pickup coil. To explain the fluxgate principle, the following two graphics in Figure 9 and Figure 10 are divided into four steps, listed below. At first, the scenario with a constant external magnetic field is explained. Afterward, the same steps are explained for an alternating external magnetic field in Figure 10.

- (a) excitation voltage waveforms and external constant/alternating field on each core,
- (b) two-segment linear saturation characteristic of cores,
- (c) flux behavior inside the two rods in dependence on an external field,
- (d) induced voltage across the pickup coil due to the counteraction of two magnetic fields.

In Figure 9 a.) the excitation signals, which are driving the sensor rods periodically into positive and negative saturation through the excitation coil, are shown. The green line represents an additional direct magnetic flux B_{ext} inside the two rods, coming from a constant external magnetic field H_{ext} . Figure 9 b.) shows schematically the saturation curve of the sensor core materials. Next, the external field is applied to the sensor (Figure 9 c.), which causes a flux offset in both cores and this changes the time instant when each sensor rod reaches the saturation flux density. As a result the induced voltages across the pickup coil no longer cancel each other out, which leads to a voltage signal across the pickup coil. The voltage signal is after a synchronous demodulation process (see Chapter 3.2.2), directly proportional to the external field applied to the sensor, shown in Figure 9 d.).

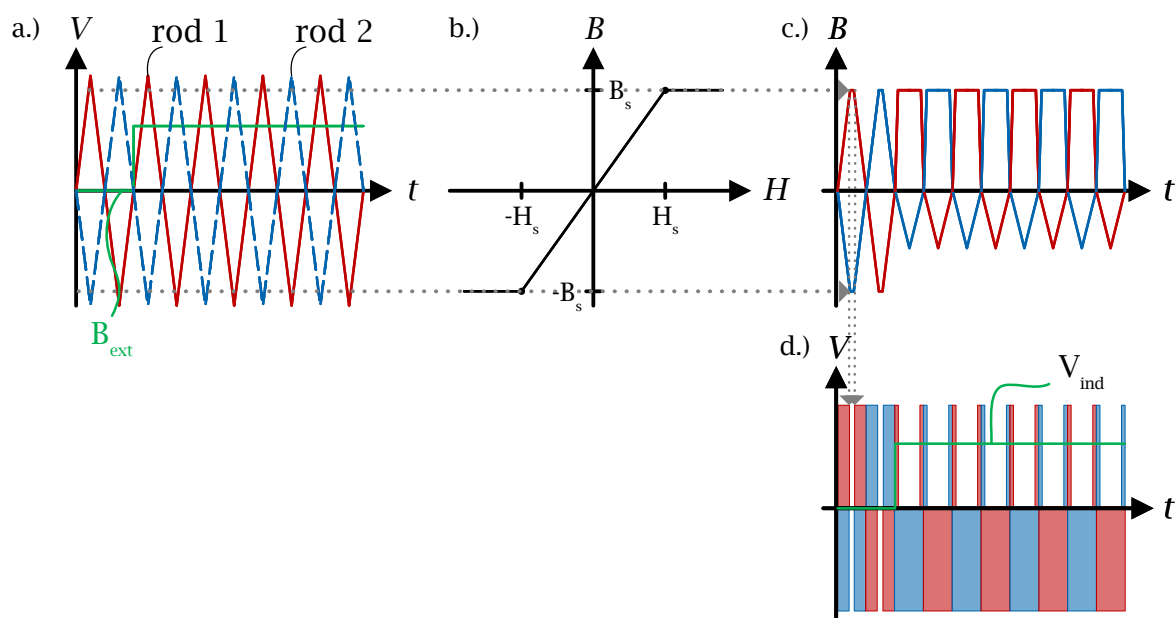


Figure 9: Schematic representation of the voltage and field characteristics while the sensor experiences a constant external magnetic field H_{ext} , which leads to a magnetic flux B_{ext} inside the sensor rods.

Consideration of an alternating external Field

Instead of a direct external field, the sensor experiences an alternating external magnetic field H_{ext} , which leads to an alternating flux B_{ext} inside the sensor rods. Figure 10 a.) depicts the drive voltage applied to the excitation coil, which leads to the excitation flux inside the core. The green line represents the externally induced alternating flux inside the rods, which changes the point of time when the sensor rods reach the saturation flux density. Figure 10 b.) shows schematically the saturation curve of the sensor core materials. The external alternating field is applied to the sensor (Figure 10 c.), which causes an alternating flux offset in both cores. The flux offset induces a voltage across the pickup winding, as depicted in Figure 10 d.). Using bandpass

filtering, as long as the corresponding frequency is known, and subsequently integrating the voltage-time areas, it is possible to infer the alternating externally induced flux.

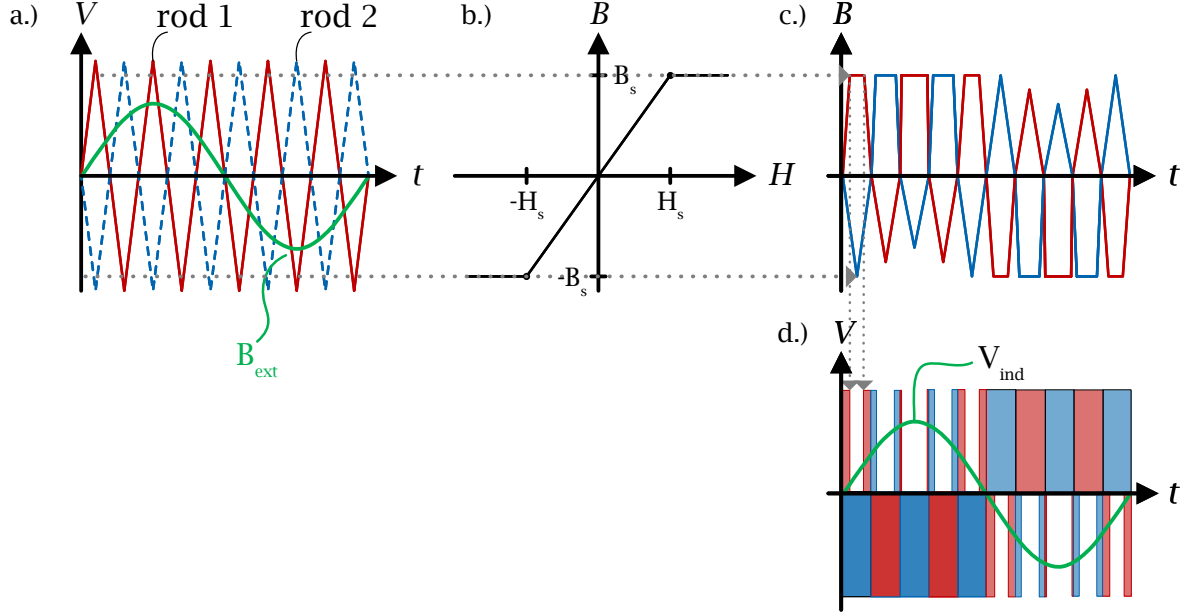


Figure 10: Schematic representation of the voltage and field characteristics while the sensor experiences an alternating external magnetic field H_{ext} , which leads to a magnetic flux B_{ext} inside the sensor rods.

2.2.2 Non-linear Measurand at the Intermediate Main and Leakage Flux

Measuring the flux outside the probe core, the sensor experiences different types of flux. Part of the main flux and the leakage flux over air. The hysteresis curve is not linear, therefore the transition from main flux to leakage flux also leads to a non-linearity of the sensor signal to the magnetic field. Figure 11 schematically illustrates the different flux paths of a single-phase transformer inside the iron core during normal operation and deep saturation, according to the saturation curve on the right-hand side. An ideal transformer would have no leakage flux since all main flux occurs within the ferromagnetic core material. In reality, such transformers cannot exist. During normal operation, there is also a leakage flux due to the two coils and the ferromagnetic core material properties which mainly close over air [13]. This flux is shown in Figure 11 by the thinner green line, but for simplicity, only the lines from the primary side are shown.

If the transformer experiences a flux offset, for example, by a superimposed DC, and thus the saturation flux density B_{sat} of the sensor core material is exceeded, part of the main flux is closed via air, shown through the orange filed lines. The fluxgate sensor itself experiences part of the main flux, as the highly permeable sensor core material compared to the air, has created a parallel magnetic path. When the transformer reaches the non-linear part of the hysteresis

curve, the sensor experiences a rising leakage flux. The amplitudes of both fluxes across the sensor depend on the load, respectively on the operating point in the hysteresis curve of the transformer.

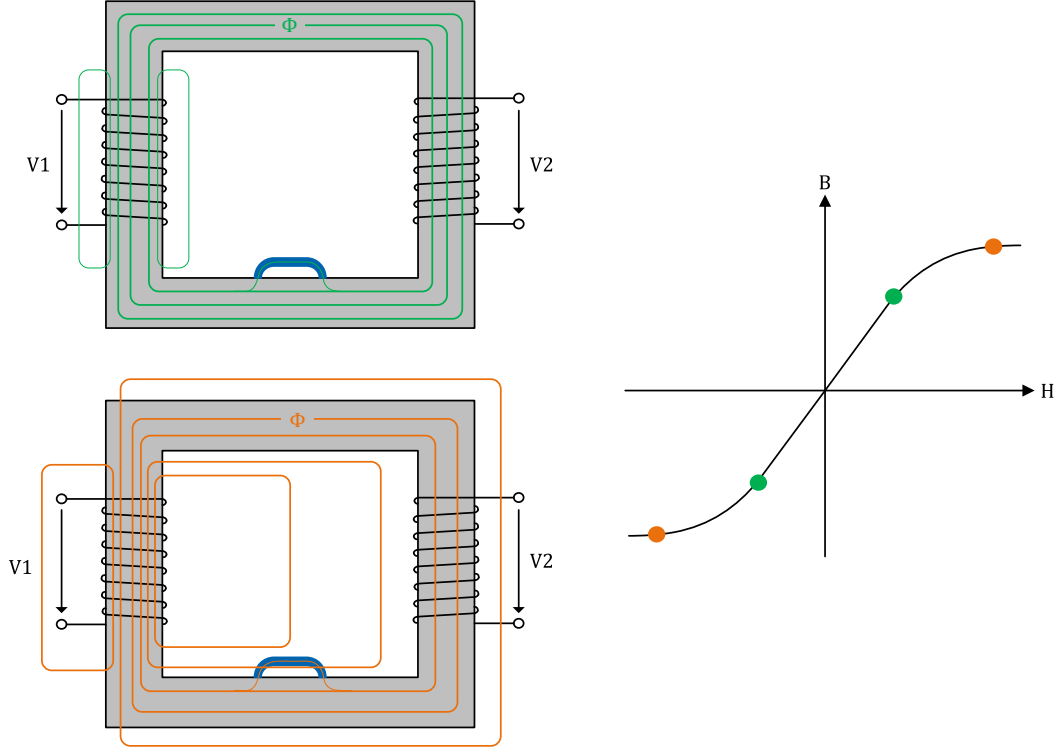


Figure 11: Magnetic flux line comparison between normal operation and saturated transformer core.

2.2.3 Calculation of external Field

The direct magnetic flux inside the transformer core cannot be measured directly. The fluxgate technology is therefore used for the measurement, in which the information of the magnetic flux is modulated onto a carrier frequency (see Chapter 2.2.1). To determine the information contained in the measurement signal, the mathematical relationship is derived below. The following calculations and explanations are described in more detail in [4].

The sensor experiences two magnetic fields: the external magnetic field $\mathbf{H}_0(t)$ and the drive magnetic field \mathbf{H}_1 produced by the excitation coil:

$$\mathbf{H}_\Sigma(t) = \mathbf{H}_0 + \mathbf{H}_1(t). \quad (6)$$

The induced magnetic flux \mathbf{B} can be calculated with Equation 7. Where the vector function ξ represents the correlation of anisotropic, hysteresis, and non-linear properties of magnetic materials. To simplify the determination of the generated EMF in the pickup coil, the hysteresis

and anisotropic effects are neglected and only the non-linear part of the core magnetization is considered:

$$\mathbf{B} = \xi([\mathbf{H}_\Sigma]) \rightarrow f([\mathbf{H}_\Sigma]). \quad (7)$$

In this thesis, a sensor with two parallel ferromagnetic cores is used. Subsequently, the calculations are performed in one dimension only, since the magnetic flux in the direction of the transformer core material is of relevance $\mathbf{B} \rightarrow B$. Two parallel magnetic fields are produced (magnetic flux B_1 in the first sensor rod, respectively, magnetic flux B_2 in the second sensor rod). The magnetic induction in each core can be summarized, taking into consideration the previously described simplification (Equation 7), with:

$$\begin{aligned} B_1 &= f(H_0 + H_1), \\ B_2 &= f(H_0 - H_1). \end{aligned} \quad (8)$$

To explain the magnetic correlations, a sinusoidal signal is assumed as the excitation signal. With the help of the law of induction (Equation 16) and the relationship between magnetic flux, magnetic flux density, and the cross-sectional area of a material (Equation 17), the induced voltage across a pickup coil can be calculated as follows:

$$V_{\text{pickup}}(t) = -nA_{\text{fe}} \frac{d}{dt} (B_1 + B_2). \quad (9)$$

Where n represents the number of turns and A_{fe} is the cross-section of the used core. Due to the non-linearity, the dependence $B(H)$ is now approximated with a third-order polynomial, in Equation 10. Where a and b are coefficients.

$$B = aH - bH^3 \quad (10)$$

The approximation leads to Equation 11. The third term represents the correlation of the external and excitation magnetic fields. For this reason, it leads to an induced voltage in the pickup coil, Equation 12. The non-linear part of the magnetization process $B(H)$ is responsible for inducing a voltage that provides information about the external magnetic field H_0 . [4]

$$B_1 + B_2 = 2aH_0 - 2bH_0^3 - \underline{6bH_0H_1^2} \quad (11)$$

$$V_{\text{pickup}}(t)|_{H_0 = \text{const} \neq 0} = 6bA_{\text{fe}}nH_0 \frac{dH_1^2(t)}{dt} \neq 0 \quad (12)$$

Assuming the drive field is composed of two independent fields (where H_1 is the drive field and H_2 is the external field) and considering the case where the frequency of the second field is zero ($\omega_2 = 0 \frac{1}{s}$), a constant field is superimposed to the drive field. Where H_m , $H_{m,1}$ and $H_{m,2}$ represent the amplitudes and ω_1 and ω_2 the angular frequencies of the corresponding magnetic

fields.

$$\begin{aligned} H_1(t) &= H_{m,1} \sin(\omega_1 t) + H_{m,2} \cos(\omega_2 t) \\ &= H_{m,1} \sin(\omega_1 t) + H_{m,2} \end{aligned} \quad (13)$$

Now Equation 13 is inserted into Equation 12, and from this results the Equation 14. It is shown that the induced voltage V_{pickup} depends directly on the drive frequency, which means that the accuracy of the sensor is directly proportional to the drive frequency. The assumed constant field is modulated to a higher frequency, which corresponds to the second harmonic. The second harmonic of the signal is used to demodulate the signal and to extract the external field H_{ext} information out of the measured signal (see Chapter 3.2.2). [4]

$$V_{\text{pickup}}(t) = 6\omega_1 b A_{\text{fe}} n H_0 [2H_{m,1} H_{m,2} \cos(\omega_1 t) + H_{m,1}^2 \sin(2\omega_1 t)] \quad (14)$$

2.2.4 Auxiliary Core Design

The geometry and magnetic properties of the additional cores have a major influence on the sensitivity of the sensor. In the case of the magnetic properties, the relative permeability of the sensor core is considered. The geometry of an additional core influences the length of the magnetic path. To achieve high sensitivity, the reluctance of the transformer $R_{m,t}$ must be significantly greater than the reluctance of the sensor $R_{m,s}$. Thus lead to $R_{m,t} \gg R_{m,s}$. [7]

Equation 15 describes the relation of the magnetic resistance, between the magnetic path l_m cross-sectional area A_{fe} and the permeability in vacuum μ_0 and relative permeability μ_r of a material.

$$R_m = \frac{l_m}{\mu_0 \mu_r A_{\text{fe}}} \quad (15)$$

To achieve a low reluctance $R_{m,s}$ of the additional sensors the magnetic path l_s has to be as low as possible. This can be influenced by the height h_s and length f_s of the sensor cores. Figure 12 shows schematically the sensor core geometry. The relative permeability of the material μ_r and the cross-sectional area $A_{\text{fe},s}$ should be as large as possible to reduce the reluctance $R_{m,s}$. The cross-sectional area $A_{\text{fe},s}$ can be influenced by the width w_s of the sensor cores.

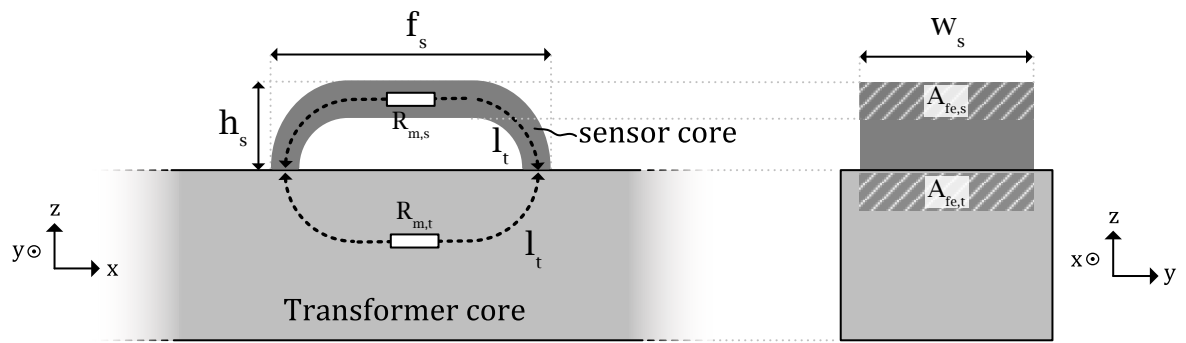


Figure 12: Geometric design of sensor core to achieve low reluctance R_m adopted from [7].

3 Sensor Design

The sensor consists of two ferromagnetic core rods, a pickup coil, and an excitation coil. For the assembly of the sensor, the design process includes:

1. ferromagnetic core material investigation and design,
2. drive circuit design,
3. excitation and pickup coil dimensioning,
4. signal processing board design.

A suitable ferromagnetic material and geometric shape have to be found, to enable the proper functionality of the sensor. Boundary conditions on this matter are explained in Chapter 2.2.4. The circuit board handles the control, excitation of the core rods, and signal processing. Requirements for the sensor and the board for a successful experimental setup are listed as follows:

- sensor must not exceed certain dimensions (width between two legs and clearance to transformer coils to ensure insulation),
- core material must be able to saturate in a specified amount of time with the help of an external current,
- should be able to measure small magnetic fields,
- possibility of direct measurement in the lab of the signal.

The excitation coil has to be wound around each sensor rod in opposite direction. The pickup coil has to be wound around both rods. Through the excitation current, a magnetic flux is generated within the sensor cores, which has the same amplitude in each half. Due to the different winding sense of the coils, the fluxes in each rod are shifted by 180° . Both induced voltages across the pickup coil cancel each other out if no external field is applied (see Chapter 2.2.1). Figure 13 shows the coil and rod arrangement of the used sensor.

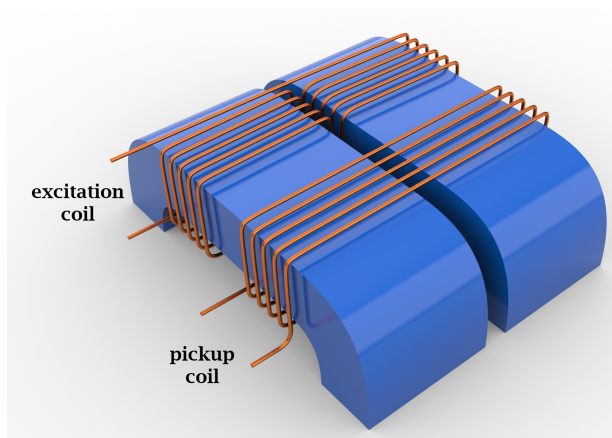


Figure 13: Two sensor rods with both windings.

During the lab test, the sensor is placed on the yoke of a 60 kVA five-leg laboratory transformer without a tank, as depicted in Figure 14. Depending on where the magnetic field respectively magnetic fluxes of the transformer need to be measured, the sensor can be placed in all yokes and legs. Around each bottom yoke, a search coil is wound to measure the induced voltage due to the alternating flux through the cross-section of the transformer core. The search coil is a wire that is wound with a certain number of turns n around a ferromagnetic material. The magnetic flux through the search coil cross-section can be inferred through the law of induction shown in Equation 16 with the connection between the flux ϕ the magnetic flux density B through a cross-section A in Equation 17.

$$V_{\text{ind}} = -n \cdot \frac{d\phi}{dt} \quad (16)$$

$$\phi = B \cdot A \quad (17)$$

This flux measurement type is a non-invasive variant. This means that the sensor does not make any mechanical changes to the core and therefore does not limit the functionality of the transformer. As can be seen in Figure 14, the two rods are only placed on the surface of the core sheets. An advantage of this method is that it can be used, for example, to retrofit energy converters with a flux measurement and thus enable monitoring. With the sensor, it is possible to measure constant, alternating, and mixed fluxes inside the core.

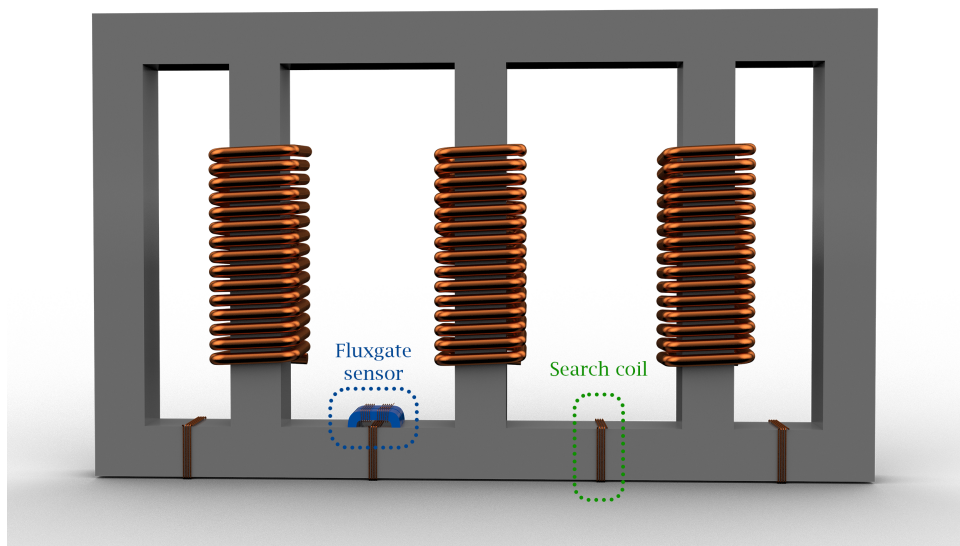


Figure 14: Schematic five-leg transformer with flux sensor laying in one yoke.

During the construction, several tests were carried out to saturate the core halves. If these tests were not successful, the process was partly restarted from scratch or improvements were investigated. The flowchart in Figure 15 shows an overview of the design process.

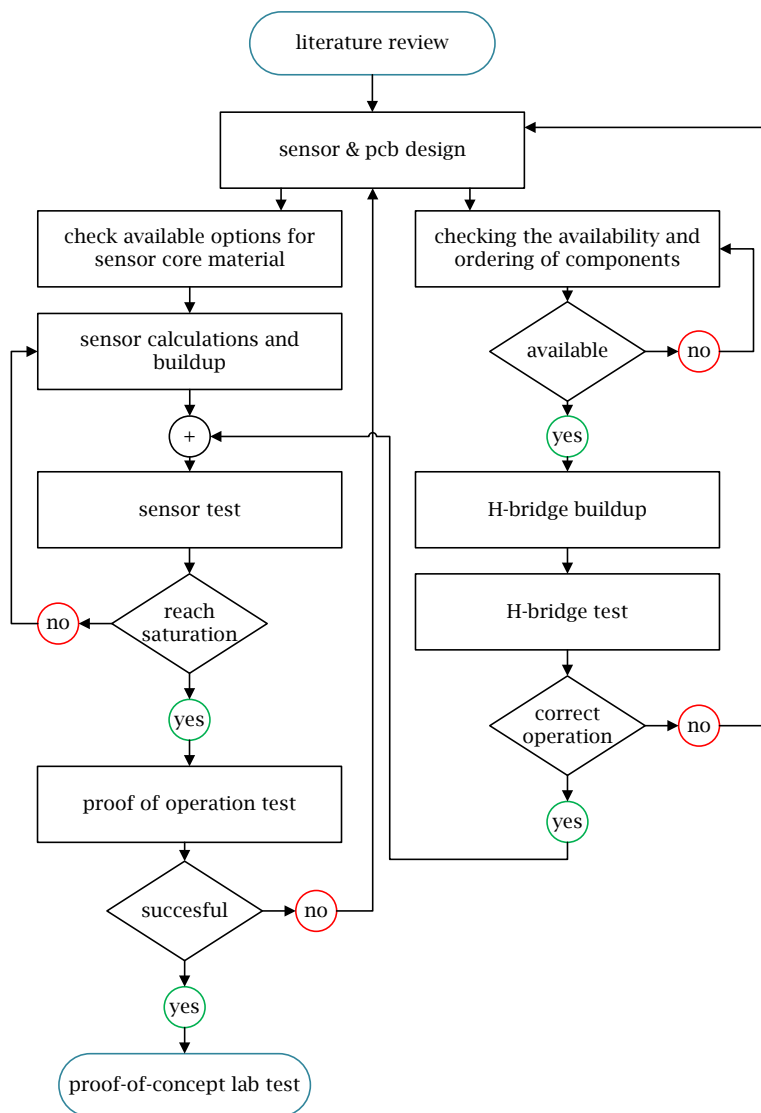


Figure 15: Sensor design approach.

3.1 Core Materials and Sensor Coils

To operate the Fluxgate the main task is to drive the two sensor rods periodically into positive and negative saturation. In order to achieve that as quickly and reliably as possible, two different ferromagnetic materials are examined in the following chapter. In order to enable flux measurement, the sensor must have a lower reluctance $R_{m,s}$ than the transformer core area $R_{m,s}$, Chapter 2.2.4. A starting point is the use of a highly permeable material so that a low reluctance can be achieved. Sometimes the used core material of a transformer is unknown, hence the reluctance of the sensor should be as low as possible. It is relatively difficult to obtain such materials in a usable form since it is mostly used for custom-made products and is not available in small geometric shapes at specialized retailers. Another requirement is the size of the sensor. It must not exceed a width of 140 mm so that it can be placed between two legs on the yoke.

A ferrite U-shaped core, which is available for high-frequency applications, is used as first sensor material. After initial saturation tests, it was determined, that the magnetic properties are unsuitable to drive the material very quickly into positive and negative saturation. For comparison, nanocrystalline cores are investigated, which meet the sensor requirements better than the ferrite material. Nanocrystalline cores are tape-wounded toroidal cores and are a composite of iron, copper niobium silicon, and born. The cores are produced in circular and oval shapes. For the sensor, an oval core has been riled up in the middle. The dimensions of the two core rings are illustrated in Figure 16.

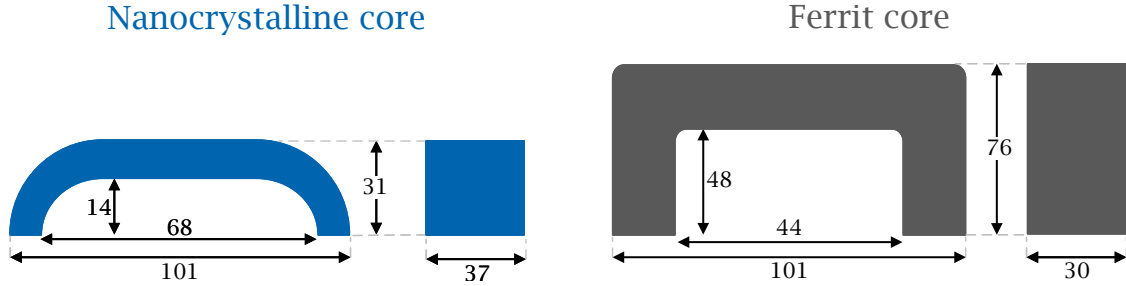


Figure 16: Nanocrystalline and ferrite core (dimensions in mm).

The nanocrystalline core material data sheet is available in Appendix B.1. The data sheet of the ferrite core can be found in [20]. Table 1 depicts the comparison of magnetic core properties between the two materials.

Table 1: Properties of used materials for the fluxgate sensor from [20], [21] and Appendix B.1.

	μ_r	B_{sat}	A_L	P_1	magnetostriction	L_{fe}	A_{fe}
material	1	$\frac{\text{Vs}}{\text{m}^2}$	μH	$\frac{\text{W}}{\text{kg}}$	ppm	mm	mm^2
ferrit N27	1580	0.5	4.6	10.3 (0.1 $\frac{\text{Vs}}{\text{m}^2}$, 25 kHz)	-	184	840
nanocrystalline	30000	1.2	24.1-48.2	80 (0.3 $\frac{\text{Vs}}{\text{m}^2}$, 10 kHz)	0.5	112	190

The main benefit of the nanocrystalline material is the higher relative permeability. A faster saturation of the cores is achieved, although the maximum saturation flux density $B_{\text{sat}} = 1.2 \text{ Vs/m}^2$ is more than twice as high as the ferrite material. This can be explained by the fact, that with higher relative permeability, the slope of the hysteresis curve gets much steeper, and therefore the sensor can be saturated with a lower magnetic field strength $H_n < H_f$, as shown in Figure 17.

The nanocrystalline cores have another advantage over the ferrite material:

- low-temperature dependency,
- low magnetostriction,
- isolating oil resistivity,
- low dependency of magnetic properties to external force.

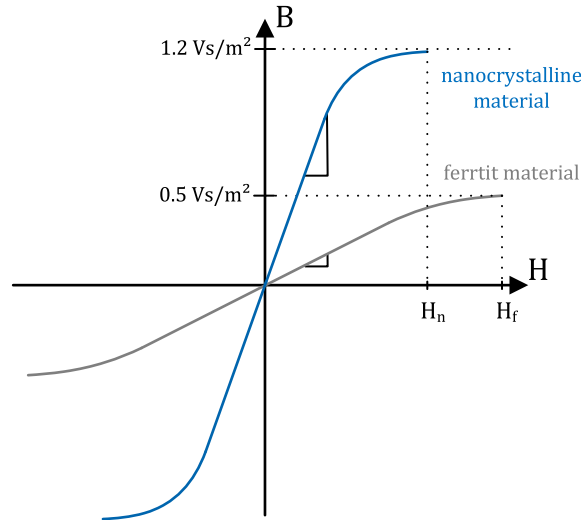


Figure 17: Schematic representation of the different material hysteresis curves.

Impedance Spectrum

To illustrate the differences between the two core materials (nanocrystalline and ferrite), Figure 18 depicts the impedance spectrum of the nanocrystalline core (Blueferrite D0080O30N01) and the ferrite core (TDK B67370A0002X027). The impedance between 100 Hz and 8 kHz is practically constant for the nanocrystalline core in comparison to the ferrite core. The required power to drive the nanocrystalline cores into saturation is lower, which allows a more efficient excitation circuit design. The reluctance of the series magnetic circuit, consisting of the two air gaps (between the half nanocrystalline core and the transformer yoke) and the sensor core (schematic series circuit shown in Figure 30), is lower. The reduced reluctance is coming from the enhanced magnetic properties of the nanocrystalline material. Thus, increasing the sensitivity

of the sensor.

The impedance spectrum was recorded while the cores were placed on the yoke with the transformer powered off. The vector network analyzer (VNA) was connected to the excitation coil.

Table 2 lists characteristic points of the bode measurement, which are used during the sensor design process for sensor coil calculation and the power electronics design.

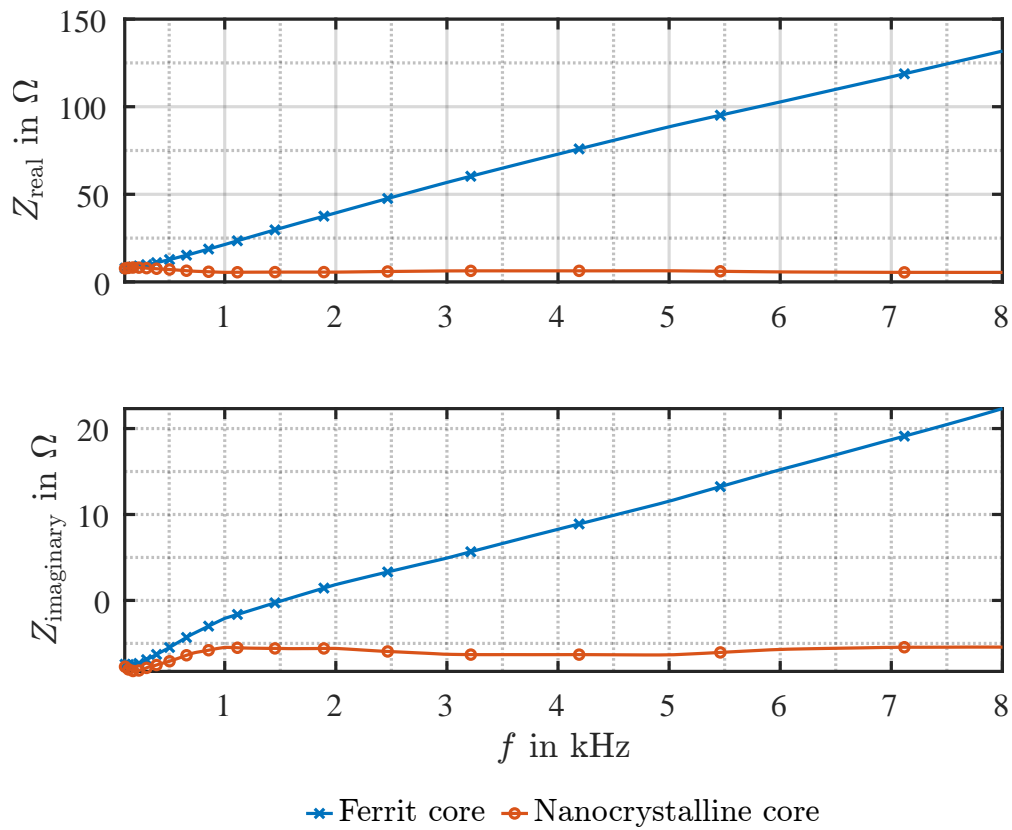


Figure 18: Measured impedance spectrum of the used materials.

Table 2: Comparison between the used materials, showing some significant points of the impedance spectrum.

material	f	Z_{real}	$Z_{\text{imag}} = X$	Magnitude	Phase
	Hz	Ω	Ω	Ω	$^{\circ}$
nano-crystalline	100.00	9.29	0.08	9.29	179.48
	1002.19	6.82	1.00	6.90	171.66
	2049.21	6.68	1.97	6.96	163.54
	4080.57	7.14	3.83	8.10	151.80
	10043.75	5.32	8.71	10.21	121.40
ferrit	100.00	-7.42	2.39	7.80	162.12
	1002.19	-2.07	21.27	21.37	95.57
	2049.21	2.00	40.21	40.26	87.15
	4080.57	8.54	73.70	74.19	83.39
	10043.75	30.81	157.78	160.76	78.95

Coil Dimensioning

The sensor is excited through an excitation coil which is fed by a rectangular voltage signal. The rectangular signal is used due to the comparative simple generation with a H-bridge. There are four levels of freedom for calculating the number of turns to ensure reliable saturation of the sensor core rods:

- supply voltage V_{supply} respectively current through the excitation coil,
- excitation frequency,
- number of turns of the excitation coil,
- adjustment of R and L parameters to adapt the time constant τ_{sensor} .

To drive the sensor rods into saturation it is necessary to have a high current through the excitation coil. The bridge circuit instead, delivers a rectangular voltage signal, because metal-oxide-semiconductor field-effect transistors (MOSFETs) are able to switch high voltages easily but can get destroyed through high currents. A transformer is connected between the H-bridge and the excitation coil which transforms the supply voltage V_{source} to a lower amplitude V_{supply} to achieve a higher current through the sensor excitation coil. The drive voltage at the sensor is calculated according to Equation 18.

$$V_{\text{supply}} = V_{\text{source}} \cdot \frac{n_2}{n_1} = 66 \text{ V} \cdot \frac{6}{13} \approx 30.5 \text{ V} \quad (18)$$

With the law of induction, shown in Equation 16, and the correlation of the peak value of the magnetic flux $\hat{\Phi}$, magnetic saturation flux density B_{sat} , and cross-section A_{fe}

$$\hat{\Phi} = B_{\text{sat}} \cdot A_{\text{fe}}, \quad (19)$$

Equation 20 can be obtained. The necessary turns of the excitation coil, to ensure the saturation of the two rods, can be calculated. Factor four in the denominator of the Equation 20 depends on the supply voltage waveform. It describes the difference in the area underneath the voltage curve between sine, rectangular, and triangle signals. For the used rectangular supply voltage the factor is four, a sine wave for example requires a factor of $\sqrt{2}\pi$. [22]

$$n_{\text{excitaiton}} = \frac{V_{\text{supply}}}{4 \cdot f \cdot B_{\text{sat}} \cdot A_{\text{fe}}} = \frac{30.5 \text{ V}}{4 \cdot 4000 \text{ Hz} \cdot 1.2 \frac{\text{Vs}}{\text{m}^2} \cdot 1.9 \cdot 10^{-4} \text{ m}^2} \approx 8.3 \quad (20)$$

The calculation leads to 5.9 turns for the excitation winding. Due to various trials during the sensor build, seven turns were applied.

Time Constant Investigation

The previously measured values of the impedance spectrum can be used to calculate the resistance and inductance of the sensor laying on the transformer yoke. This allows to determine the time constant τ_{sensor} (Equation 21) of the RL series circuit and ensures that the excitation time $t_{\text{excitation}}$ is sufficient to drive the core material into saturation. The excitation time $t_{\text{excitation}}$ and period time T_{P} of the signal are shown schematically in Figure 19.

$$\tau_{\text{sensor}} = \frac{L}{R} = \frac{L_{1-1} + L_{1-2}}{R_{2-1} + R_{2-2}} \quad (21)$$

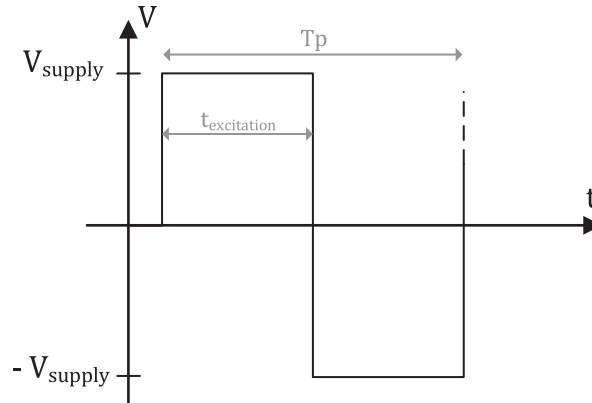


Figure 19: Schematic of excitation time $t_{\text{excitation}}$ and period time T_{P} .

Starting with the following Equation 22 which shows the connection between the real and imaginary parts of the sensor.

$$Z_{\text{sensor}} = Z_{\text{real}} + jZ_{\text{imag}} = R + jX = R + j\omega L \quad (22)$$

By converting the Equation 22, the frequency-dependent inductance of the entire sensor can be

determined. In this case, only the value at the excitation frequency $f_{\text{excitation}} = 4 \text{ kHz}$ is of interest. The required values for the calculation are from Table 2.

$$L_{\text{sensor}}(f) = \frac{Z_{\text{imag}}}{2 \cdot \pi \cdot f} \quad (23)$$

$$L_{\text{sensor}}(4080.57 \text{ Hz}) = \frac{3.83 \ \Omega}{2 \cdot \pi \cdot 4080.57 \text{ Hz}} \approx 1.49 \cdot 10^{-4} \text{ H} \quad (24)$$

In order to achieve the fastest possible saturation in the cores, the time constant of the entire sensor τ_{sensor} is now calculated using the previously determined values for the inductance and the resistance. The time constant must be smaller than five times a half period, as depicted in Equation 25, otherwise, the core material would not reach the saturation flux density of $1.2 \frac{\text{Vs}}{\text{m}^2}$ in the given period of time $\frac{T_p}{2}$.

$$\tau_{\text{sensor}} = \frac{L}{R} = \frac{L_{1-1} + L_{1-2}}{R_{2-1} + R_{2-2}} < 5 \cdot \frac{T_p}{2} \quad (25)$$

Using the Equation 26, the duration of a half period can be determined depending on the used excitation frequency.

$$t_{\text{excitation}} = \frac{T_p}{2} = \frac{1}{2 \cdot f_{\text{excitation}}} = \frac{1}{2 \cdot 4000 \text{ Hz}} = 1.25 \cdot 10^{-6} \text{ s} \quad (26)$$

For verification, the time constant τ_{sensor} of the sensor can now be calculated as follows:

$$\tau_{\text{sensor}} = \frac{L_{\text{sensor}}}{R_{\text{sensor}}} = \frac{1.49 \cdot 10^{-4} \text{ H}}{7.14 \ \Omega} \approx 2.09 \cdot 10^{-5} \text{ s} \quad (27)$$

In addition, the time constant $\tau_{\text{sensor}, R_1}$ with a further resistor R_1 connected in series to the excitation coil, illustrated in Figure 20, is calculated.

$$\tau_{\text{sensor}, R_1} = \frac{L_{\text{sensor}}}{R_1 + R_{\text{sensor}}} = \frac{1.49 \cdot 10^{-4} \text{ H}}{6.8 \ \Omega + 7.14 \ \Omega} \approx 1.06 \cdot 10^{-5} \text{ s} \quad (28)$$

Figure 20 shows the equivalent circuit of the sensor. Thereby, R_{2-1} and R_{2-2} are the resistors, and L_{1-1} and L_{1-2} the inductances of the windings around the first sensor rod respectively the second rod. The resistor R_1 was added to decrease the time constant.

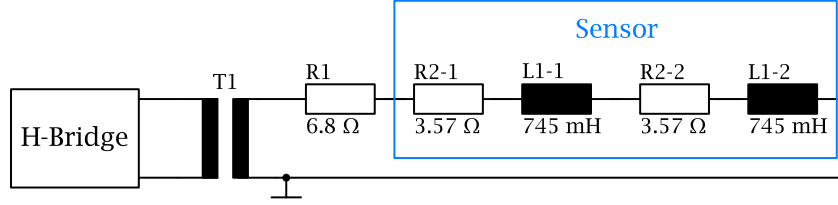


Figure 20: Sensor equivalent circuit.

Since both time constants τ_{sensor} and τ_{sensor,R_1} are now known, the current as function of time can be calculated with Equation 29.

$$i(t) = \frac{V_{\text{supply}}}{R_1 + R_{\text{sensor}}} (1 - e^{-\frac{t}{\tau}}) \quad (29)$$

Figure 21 shows the current over time for two different time constants. The violet line marks the time of a half excitation period $t_{\text{excitation}}$. With the additional resistor R_1 it is possible to drive the sensor rods even faster into saturation. Note that the additional resistance increases the power demand of the sensor, as follows:

$$P_{R_1} = \frac{V_{\text{supply}}^2}{R} = \frac{(30.5 \text{ V})^2}{6.8 \Omega} \approx 137 \text{ W}. \quad (30)$$

The delivered power of the laboratory power supply is calculated using Equation 31 and the measured supply current $I_{\text{source}} = 3.6 \text{ A}$.

$$P_{\text{source}} = V_{\text{source}} \cdot I_{\text{source}} = 66 \text{ V} \cdot 3.6 \text{ A} \approx 238 \text{ W} \quad (31)$$

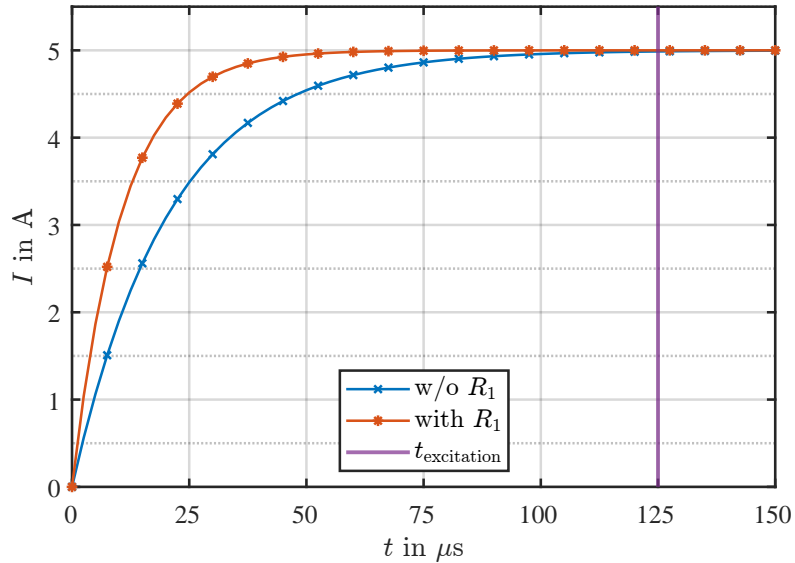


Figure 21: Comparison between the time constants τ_{sensor} and τ_{sensor,R_1} in dependence of an additional resistor.

3.2 Electronic Design

The electronic design includes a circuit to energize the sensor and a circuit to process the measured signal. The drive circuit provides a square wave signal as an excitation current for the sensor. With a H-bridge, the generation of a rectangular signal is easy to realize. For comparison, to produce a sinusoidal drive signal the bridge would have to work with a much higher switching frequency and PWM, see Figure 22. A higher clock frequency is necessary to simulate a sine signal with single steps. The higher the clock frequency of the PWM signal is, the more accurately the sine signal can be formed. Additional filters would have to be designed, which would result in more complex frequency analysis. The following chapters give an overview of the used H-bridge structure which is controlled by a micro-controller unit (MCU).

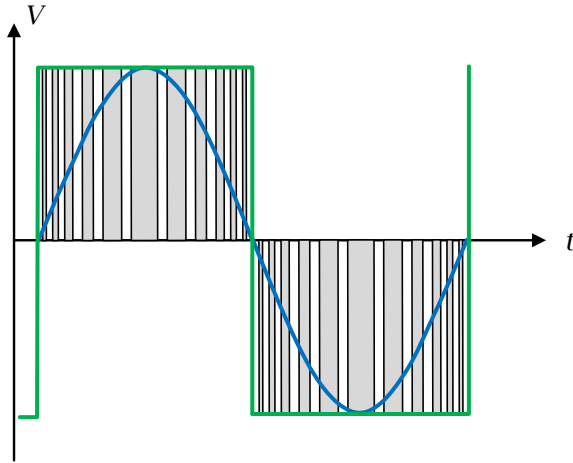


Figure 22: Rectangular and PWM produced sine signals.

3.2.1 H-Bridge

The H-bridge consists of four n-channel metal-oxide-semiconductor field-effect transistors (MOSFETs) which are controlled by two half-bridge drivers. They receive the excitation signals from the MCU. Figure 23 depicts the schematic circuit of the bridge. The used power-MOSFETs are from the manufacturer Infineon (type IRFB4620PBF), which have internal free-wheeling diodes. The sensor is an ohmic-inductive load, which requires special attention during the switching-off process, e.g. due to voltage overshooting. During excitation, the inductance L stores the energy E_L , according to Equation 32. When switching off, the stored energy in the magnetic field of the inductance must be dissipated. [23]

$$E_L = \frac{L_{\text{sensor}} i^2}{2} \quad (32)$$

Due to this self-induction, a voltage overshoot occurs. The overshooting amplitude has a higher peak value, the larger the inductance and the current change Δi is, respectively the smaller the

time of the current change $\frac{di}{dt}$ is, depicted in Equation 33.

$$u(t) = L_{\text{sensor}} \frac{di}{dt} \quad (33)$$

To reduce the voltage overshooting of the sensor during the switching cycles, free wheel diodes are included inside power-MOSFETs. To support the task of these free-wheeling diodes, fast-switching silicon carbide (SiC)-Schottky diodes (type C3D03060F) are added in parallel to the MOSFETs. Three bipolar transient voltage suppressor (TVS) diodes are used to dissipate high voltages to ground (GND).

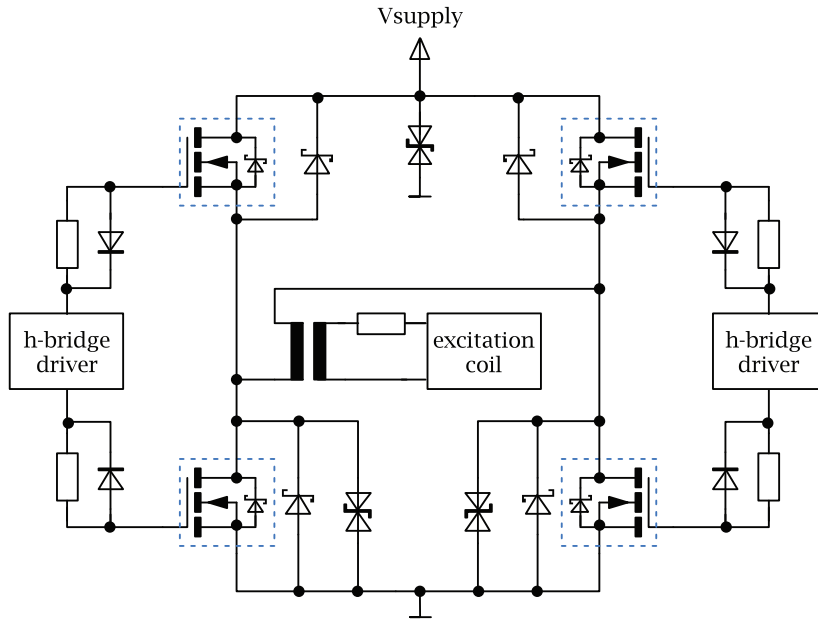


Figure 23: H-bridge equivalent circuit.

To use four n-channel MOSFETs in one H-bridge, they must be controlled by suitable gate drivers. One half-bridge driver is used for each bridge side. A schematic diagram of the integrated circuit (IC) is shown in Figure 24. The upper two MOSFETs are operated as source followers. For this purpose, it is necessary that the bootstrap capacitor C_{boot} has at least a certain size. Further information on this topic can be found in [18].

The calculation of the bootstrap capacitor C_{boot} is explained in more detail in the design guide [24]. For correct operation, the capacitor must be at least ten times larger than the gate capacitor C_g , as depicted in Equation 35. The gate capacitor can be calculated with the gate charge ($Q_g = 25 \text{ nC}$ [25]) of one MOSFET and the voltage V_Q , as depicted in Equation 34. $V_{\text{boot,diode}} = 2.5 \text{ V}$ is the forward voltage drop across the boot diode [26].

$$V_Q = V_{CC} - V_{\text{boot,diode}} = 12 \text{ V} - 2.5 \text{ V} = 9.5 \text{ V} \quad (34)$$

$$C_{\text{boot}} > 10 \cdot C_g = 10 \cdot \frac{Q_g}{V_Q} = 10 \cdot \frac{25 \text{ nC}}{9.5 \text{ V}} \approx 26.3 \text{ nF} \quad (35)$$

A sufficiently large bootstrap capacitor $C_{\text{boot}} = 0.1 \mu\text{F}$ is included within the circuit.

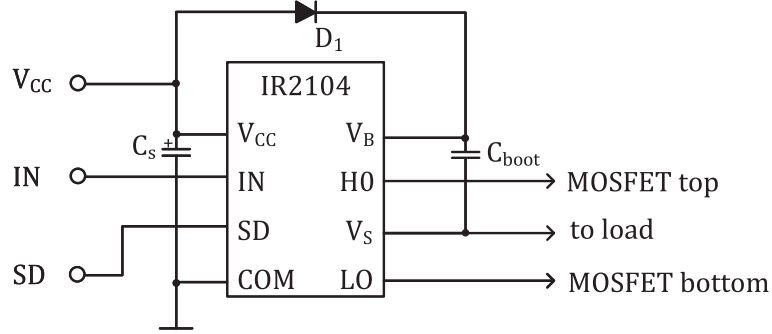


Figure 24: Half bridge driver IR2104 [25].

Excitation Control with Crystal Oscillator

In the beginning the Arduino Nano was used as a microcontroller, however, it quickly became obvious that using its internal clock signal was not sufficient to operate the H-bridge reliably with the desired frequency $f_{\text{excitation}}$. Because of that disadvantage, the circuit was modified to use a controller from the manufacturer STM32, which offers the possibility to connect an external crystal oscillator up to a frequency of 72 MHz.

The connection impedance of an external oscillator must be matched to the circuit to suppress resonances. Using Equation 36 the load capacitance C_1 is calculated, which represents the oscillator circuit terminal capacitance [27]. This value is given by the crystal manufacturer and is $C_1 = 18 \text{ pF}$ for the used 16 MHz crystal (QCL16.0000F18B23B) [26]. C_s is the stray capacitance of the printed circuit board (PCB) including wire connections and terminals. It is assumed to be $C_s = 7 \text{ pF}$, according to the design guide [27].

$$C_1 = \frac{C_1 C_2}{C_1 + C_2} + C_s \quad (36)$$

By transforming the Equation 36, the capacitors C_1 , C_2 can now be determined.

$$C_1 - C_s = \frac{C_1 C_2}{C_1 + C_2} \rightarrow 11 \text{ pF} = \frac{22 \text{ pF} \cdot 22 \text{ pF}}{22 \text{ pF} + 22 \text{ pF}} \quad (37)$$

Figure 25 depicts the circuit of the crystal oscillator X_1 and the two capacitors C_1 and C_2 connected to the MCU input pins PF0 and PF1.

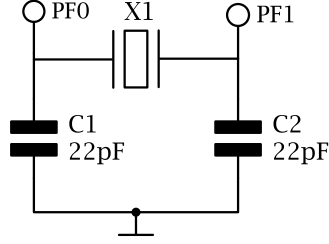


Figure 25: Circuit of external crystal oscillator.

The following table 3 lists the used pins of the controller and the equivalent pins of an Arduino Nano.

Table 3: Connected pins of STM32 Nucleo microcontroller.

STM32 pins	Arduino Nano pins	usage
PA0	A0	4 kHz clock signal to demodulation chip
PA1	A1	input 1: button switch on
PA4	A3	2 kHz left H-bridge excitation signal
PA6	A5	2 kHz right H-bridge excitation signal
PA7	A6	input 2: button switch off
PB0	D3	output 1: red status LED
PB1	D6	output 2: H-bridge driver enable
PF0	D7	external clock 1
PF1	D8	external clock 2

An advantage of this microcontroller is the easy configuration of the timers by using a graphical user interface (GUI). To trigger the H-bridge, each diagonal requires an excitation signal, which is now provided by two timers of the chip. Two signals are triggered in such a way that a necessary dead time is maintained to prevent a short circuit of the H-bridge.

The calculations (Equations 38 to 41) are required to set the two timers for the excitation control. Further information and the description of the clock calculations and configuration for the STM32 MCU timers can be found in [28]. TIM1 and TIM2 CLK are used to generate the control signals. The source clock for both APB TIM1 and TIM2 CLK is the externally connected crystal oscillator. The frequency difference between the two APB clocks has its origin in the internal timer wiring within the MCU.

$$TIM1\ CLK = \frac{APB\ TIM1\ CLK}{Prescaler} = \frac{32\ MHz}{16 - 1} = 2\ MHz \quad (38)$$

$$Frequency_1 = \frac{TIM1\ CLK}{ARR} = \frac{2\ MHz}{500 - 1} = 4\ kHz \quad (39)$$

$$TIM2\ CLK = \frac{APB\ TIM2\ CLK}{Prescaler} = \frac{64\ MHz}{16 - 1} = 4\ MHz \quad (40)$$

$$Frequency_2 = \frac{TIM2\ CLK}{ARR} = \frac{4\ MHz}{1000 - 1} = 4\ kHz \quad (41)$$

ARR ... auto reload register

APB ... advanced peripheral bus

TIM CLK ... timer clock

Prescaler ... divides timer clock to user-defined value

The prescaler and the auto reload register requires the value one to be subtracted from the desired value since both are starting to count at zero.

Both timers deliver an output frequency of 4 kHz. They differ in terms of the pulse width. TIM1 is used for synchronous demodulation. A duty cycle of 50 % is required for this. TIM2 is used to control the H-bridge. It provides a duty cycle of 24.75 % and generates two signals with different polarity, which are center aligned, as depicted in Figure 26.

Table 4: Timer 1 and 2 settings on MCU.

	TIM CLK	PWM Channel	Prescaler	Polarity	Counter period	Pulse
TIM1	2 MHz	1	16-1	High	500	250
TIM2	4 MHz	1	16-1	High	1000	250
	4 MHz	2	16-1	Low		750

The complete code for configuring the timers for excitation signals and other implemented functions can be found in Appendix C.

Before the MOSFETs are triggered, the correct operation of the timers is checked by using a logic analyzer to avoid damage to the semiconductors. Figure 26 displays the recorded excitation pulses, where the blue waveform represents the in-phase signal for the synchronous demodulation and the orange and violet curves represent the excitation of each diagonal of the bridge. Via the pulse width, the dead time is defined. The successful functionality of the signal can thus be confirmed.

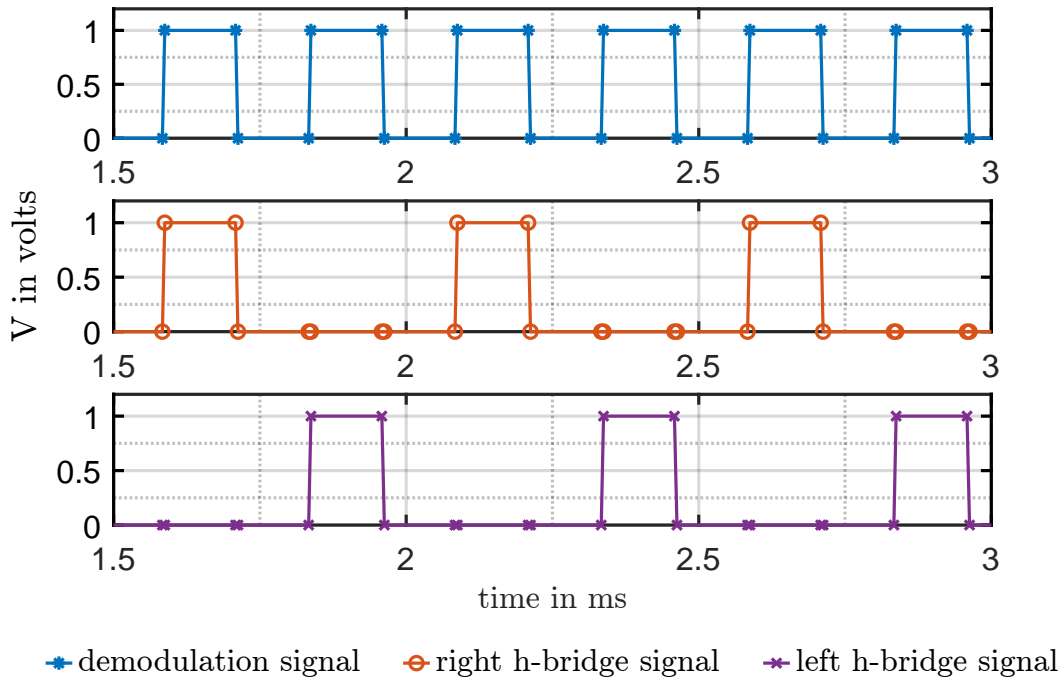


Figure 26: H-bridge excitation signals.

Saturation Investigation

In the next step, the supply bridge is completely assembled and connected to the sensor, which is already located on the yoke. During the excitation of the sensor, the current and voltage waveforms of the supply and the induced voltage across the pickup coil are recorded. These are shown in Figure 27.

Due to the waveform characteristic of the current flowing through the excitation coil and the collapsing induced voltage across the pickup coil, it can be assumed that the rods are reaching saturation.

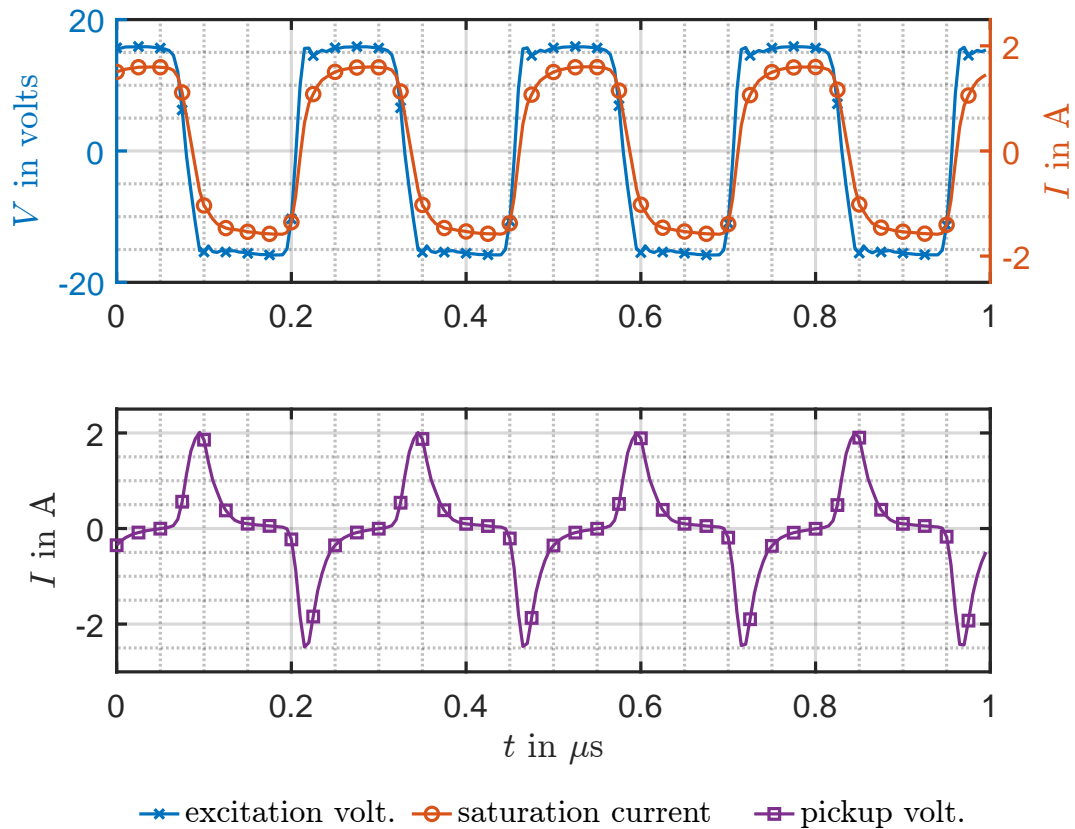


Figure 27: H-bridge supply voltage, supply- and pickup-current.

To prove the correct behavior of the sensor during excitation it is possible to investigate the hysteresis curve. Therefore, the sensor is mounted on one transformer yoke and is excited through the excitation coil. The laboratory transformers are de-energized during the measurement. It is necessary to measure the excitation current and the induced voltage of a coil, which is wound around one sensor rod.

Figure 28 shows the hysteresis curve of the fluxgate sensor. Due to the periodic positive and negative maximum saturation of each individual core, it can be assumed that the sensor is always operated on the outer envelope curve in the hysteresis curve. This has the advantage that a remanent flux, for example from the transformer core, has no effect on the sensor.

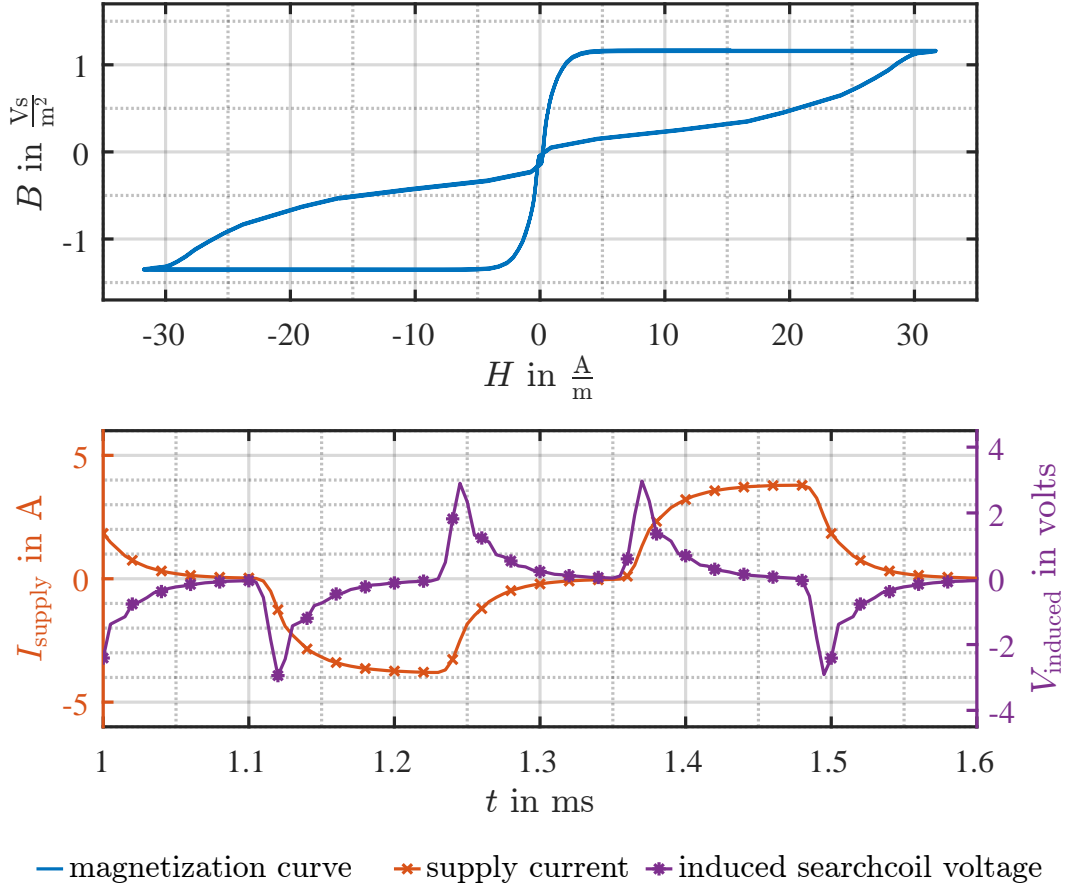


Figure 28: Hysteresis loop of the fluxgate sensor.

The magnetic field strength H is calculated with the following Equation 43, where n_1 represents the number of turns of the first winding, I_{supply} is the current through this coil and $l_{\text{coil,excitation}}$ describes the length of the coil (part of the coil wound around the sensor rod, as depicted in Figure 29).

$$l_{\text{coil,excitation}} = n_1 \cdot 2(\text{length} + \text{width}) = 14(40.13 \text{ mm} + 19.63 \text{ mm}) \approx 836 \text{ mm} \quad (42)$$

$$H = \frac{n_1 \cdot I_{\text{supply}}}{l_{\text{coil,excitation}}} = \frac{7 \cdot I_{\text{supply}}}{836 \text{ mm}} \quad (43)$$

The magnetic flux density B is calculated with the Equation 44, where V_{induced} is the induced voltage across the search coil, wound around one sensor rod. The factor n_1 describes the number of turns. A_{fe} represents the effective cross-section of one sensor rod, taking the fill-factor of into account.

$$B = \frac{\int_{t_1}^{t_2} V_{\text{induced}}(t) dt}{n_1 \cdot A_{\text{fe}}} = \frac{\int_{t_1}^{t_2} V_{\text{induced}}(t) dt}{7 \cdot 1.9 \cdot 10^{-4} \text{ m}^2} \quad (44)$$

The different hysteresis courses in Figure 28 can be explained by the periodic excitation of the

core rods followed by non-excited sections (excitation signals are shown in Figure 26). While the sensor is excited by V_{supply} , the core rods are quickly driven into saturation. Afterward, they are discharged via the free-wheeling diodes (circuit diagram shown in Figure 23) before they are saturated again in the opposite direction.

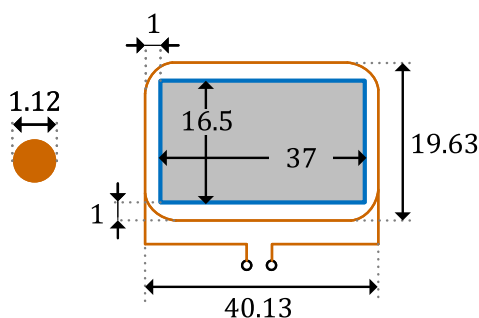


Figure 29: Nanocrystalline cross-section inclusive excitation coil (dimensions in mm). The datasheet can be found in Appendix B.1.

Characterisation of Magnetic Properties

Since the sensor is mounted on the transformer core, there are two narrow air gaps between the contact surfaces per rod. Three different materials - air, layered high grain-oriented steel (ET 110-30 LS, [29]), and nanocrystalline material - result in different reluctances. Figure 30 shows the sideways arrangement of the sensor placed on the transformer core and the equivalent connection of the occurring reluctances.

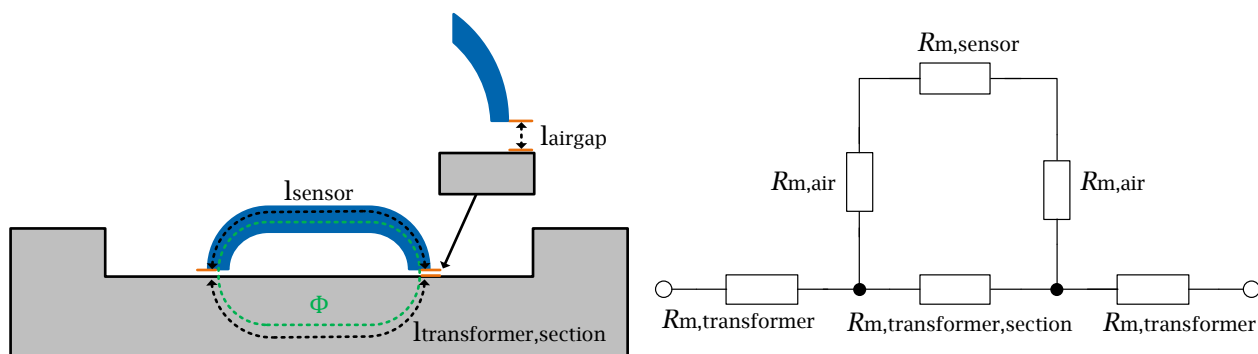


Figure 30: Magnetic circuit of transformer with sensor laying on the transformer yoke.

The air gap reluctance is calculated in Equation 45. Equation 46 shows the calculated sensor reluctance value.

$$\begin{aligned}
R_{m,\text{air}} &= \frac{l_{\text{airgap}}}{\mu_0 \cdot \mu_{r,\text{air}} \cdot A} = \\
&= \frac{0.1 \text{ mm}}{4\pi \cdot 10^{-7} \frac{\text{Vs}}{\text{Am}} \cdot 1 \cdot 1.9 \cdot 10^{-4} \text{ m}^2} \approx 41.9 \cdot 10^4 \frac{1}{\text{H}}
\end{aligned} \tag{45}$$

$$\begin{aligned}
R_{m,\text{sensor}} &= \frac{l_{\text{sensor}}}{\mu_0 \cdot \mu_{r,\text{nanocrystalline}} \cdot A_{\text{fe}}} = \\
&= \frac{112 \text{ mm}}{4\pi \cdot 10^{-7} \frac{\text{Vs}}{\text{Am}} \cdot 30 \cdot 10^3 \cdot 1.9 \cdot 10^{-4} \text{ m}^2} \approx 1.56 \cdot 10^4 \frac{1}{\text{H}}
\end{aligned} \tag{46}$$

The relative permeability $\mu_{r,\text{transformer}}$ of the transformer core material depends on the magnetic excitation field $H_{\text{transf.,lv}}$ of the low voltage coil, as indicated in Equation 47. The windings of the used transformer consist of two two-layer windings per phase. The cross-section of one coil is shown schematically in Figure 31. The magnetic excitation field $H_{\text{transf.,lv}}$ is calculated using Equation 49, where l_{lv} is the length of the low-voltage coil and $\hat{I}_{\text{a}} = 1.5 \text{ A}$ the maximum primary current of phase A at no-load operation. The low and high voltage windings have a number of turns of $n_{\text{lv}} = n_{\text{hv}} = 112$, according to [30].

$$\mu_{r,\text{transformer}} = f(H_{\text{transf.,lv}}) \tag{47}$$

The low voltage winding length l_{lv} is determined with Equation 48 assuming a rectangular winding and since it is a two-layer winding, the distance is averaged for simplicity as shown in Figure 31 using the dashed purple line.

$$\begin{aligned}
l_{\text{lv}} &= 2 \cdot n_{\text{lv}} \cdot (w_{\text{avg}} + h_{\text{avg}}) \\
&= 224 \cdot [(137.45 \text{ mm} + 13.54 \text{ mm}) \\
&\quad + (87.45 \text{ mm} + 13.26 \text{ mm})] \approx 56 \text{ m}
\end{aligned} \tag{48}$$

w_{avg} ... average width

h_{avg} ... average height

$$H_{\text{transf.,lv}} = \frac{n_{\text{transf.,lv}} \cdot \hat{I}_{\text{a}}}{l_{\text{lv}}} = \frac{112 \cdot 1.5 \text{ A}}{56 \text{ m}} = 3 \frac{\text{A}}{\text{m}} \tag{49}$$

The used grain orientated steel has a relative permeability of $\mu_{r,\text{transformer}} = 21000$ at a magnetic excitation field strength of $H_{\text{transf.,lv}} = 3 \text{ A/m}$, according to [29]. The reluctance of the core section underneath the sensor can now be calculated using Equation 50. The average iron path in the transformer core $l_{\text{transformer,section}}$ is assumed to be the same as in the sensor rods. The

average iron path is shown in Figure 30.

$$\begin{aligned}
 R_{m,\text{transformer,section}} &= \frac{l_{\text{transformer,section}}}{\mu_0 \cdot \mu_{r,\text{transformer}} \cdot A_{\text{fe}}} = \\
 &= \frac{112 \text{ mm}}{4\pi \cdot 10^{-7} \frac{\text{Vs}}{\text{Am}} \cdot 21 \cdot 10^3 \cdot 1.9 \cdot 10^{-4} \text{ m}^2} \approx 2.23 \cdot 10^4 \frac{1}{\text{H}}
 \end{aligned} \tag{50}$$

From the comparison of the three reluctances $R_{m,\text{air}}$, $R_{m,\text{sensor}}$ and $R_{m,\text{transformer,section}}$, it is observed that the air gap, although very small, causes the highest magnetic resistance. To increase the sensitivity of the sensor it is useful to increase the cross-sectional area of the air gap to reduce the reluctance $R_{m,\text{air}}$ (see Chapter 2.2.4).

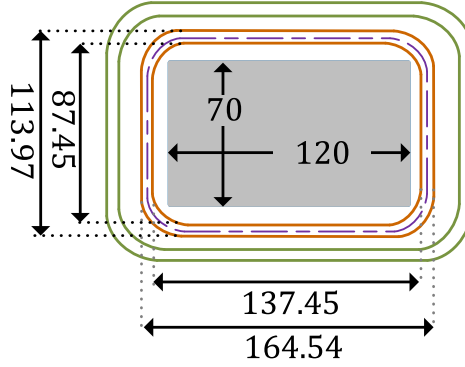


Figure 31: Cross section of five-leg transformer with two two-layer windings (dimensions in mm). The inner coil is the low voltage and the outer the high voltage winding [30].

3.2.2 Signal processing

Within the sensor core, the combination of the excitation flux and the flux induced by an external magnetic field leads to an induced voltage across the pickup coil, as explained in more detail in Chapter 2.2.1. The induced pickup signal behaves, due to the excitation, as an amplitude-modulated signal. The excitation signal is the carrier ($f_{\text{excitation}} = 4 \text{ kHz}$) and the external field, which is constant or has a much lower frequency, is modulated to it. To recover the information of the external field a synchronous demodulation process has to be performed, as depicted for a sine carrier in Figure 32 part a). $s(t)$ is the time-dependent input variable and $x(t)$ is the time-dependent output variable of the demodulation. For demodulation the double frequency $2f$ is used, as shown in Figure 32. This approach allows the extraction of the second harmonic, which is a measure of the directional flux in the sensor rods. More detailed explanations and the derivation of the second harmonic approach can be found in Chapter 2.2.3.

Synchronous demodulation multiplies the modulated carrier signal (pickup signal) by the unmodulated carrier signal which has the same frequency and phase. The unmodulated carrier

signal also can be demodulated with a square wave signal, in this case, no multiplier is used, just a simple switch. The additional parts of the switching process are suppressed by the following low-pass filter. This technique is very similar to amplitude modulation, only the used filters are different. [18]

In our case a rectangular signal is used for the excitation, therefore only a switch and a lowpass filter are necessary, which is schematically shown in Figure 32 part b).

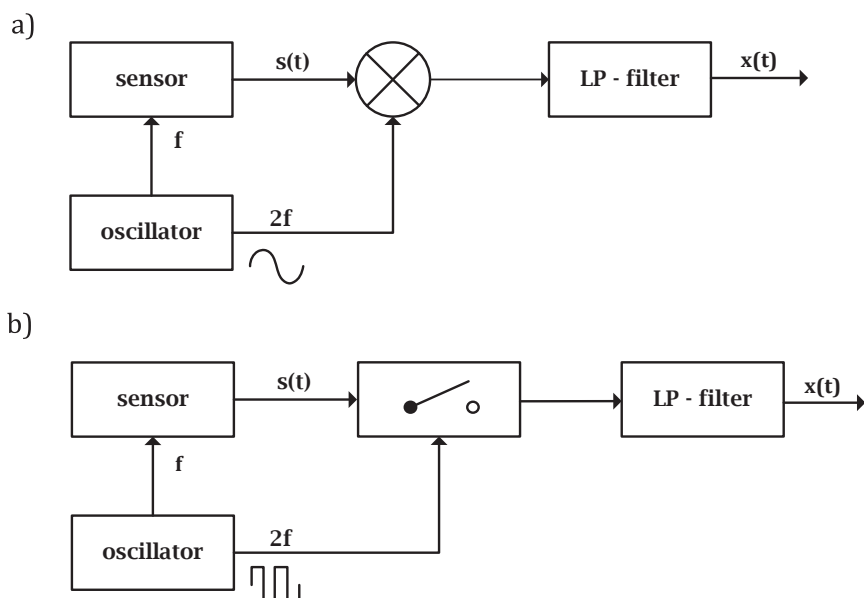


Figure 32: Synchronous demodulation: difference between sine and rectangle demodulation.

For the test setup, the signal processing is partly placed on the board and partly realized directly with the help of a power analyzer or the evaluation in MATLAB. Bandpass filtering and synchronous demodulation are performed on the board. In the laboratory, the power analyzer is the analog digital converter (ADC). The Figure 33 shows the schematic block diagram of the signal processing.

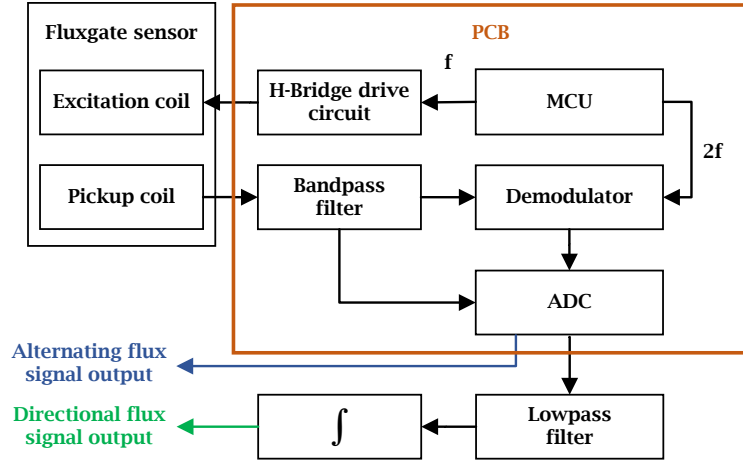


Figure 33: Schematic of signal processing.

Synchronous Demodulation and Filtering

To differentiate between the different parts of the pickup voltage signal caused by alternating and directional flux inside the sensor rods, the signal has to be filtered with two band pass filter circuits. A filter with multiple coupling is realized. The electronic circuit of this filter is shown in the Figure 34. The filter consists of an operational amplifier (OPAMP), two capacitors, and three resistors. The advantage of this circuit is that the quality Q , the gain factor k , and the resonance frequency f_c can be adjusted independently. [18]

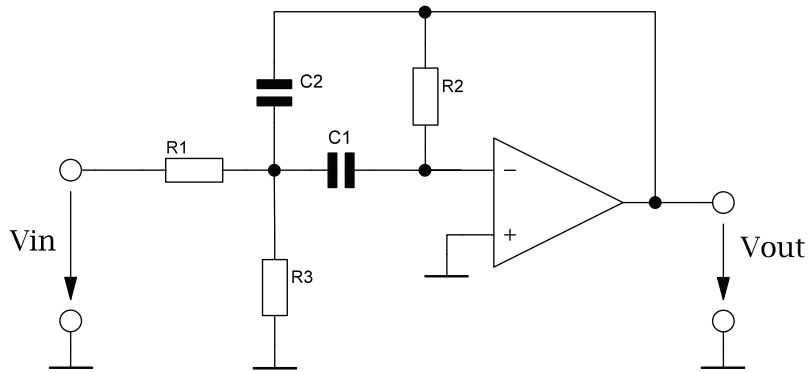


Figure 34: Band pass filter 2nd order.

Equation 51 describes the transfer function \underline{A} of the implemented band pass filter circuits. By transforming this response function, the required resistance values can then be calculated.

$$\underline{A}(s_n) = \frac{-\frac{R_2 R_3}{R_1 + R_3} C \omega_r s_n}{1 + \frac{2R_1 R_3}{R_1 + R_3} C \omega_r s_n + \frac{R_1 R_2 R_3}{R_1 + R_3} C^2 \omega_r^2 s_n^2} \quad (51)$$

For both filters a quality factor of $Q = 10$ and capacitors of $C = C_1 = C_2 = 10 \text{ nF}$ are used. The following calculations consider a resonance frequency of $f_{r1} = 50 \text{ Hz}$ for the alternating flux measurements. The gain factor is set to $A_r = -2$.

$$R_{2,fr1} = \frac{Q}{\pi f_{r1} C} = \frac{10}{\pi \cdot 50 \text{ Hz} \cdot 10 \text{ nF}} \approx 6.36 \text{ M}\Omega \rightarrow 6.2 \text{ M}\Omega \quad (52)$$

$$R_{1,fr1} = \frac{R_2}{-2 \cdot A_r} = \frac{6.2 \text{ M}\Omega}{4} \approx 1.55 \text{ M}\Omega \rightarrow 1.5 \text{ M}\Omega \quad (53)$$

$$R_{3,fr1} = \frac{-A_r R_1}{2Q^2 + A_r} = \frac{2 \cdot 1.55 \text{ M}\Omega}{200 + (-1)} \approx 15.56 \text{ k}\Omega \rightarrow 15 \text{ k}\Omega \quad (54)$$

The bandwidth B_{fr1} of the filter can be calculated with Equation 55. B_{fr1} is not affected by $R_{1,fr1}$ and $R_{3,fr1}$, which has the advantage that $R_{3,fr1}$ can be used to change the resonance frequency of the filter without changing the bandwidth. The filter is also operational without the resistor R3, but in this case, the quality depends on the gain factor A_r , Equation 56. [18]

$$B_{fr1} = \frac{f_r}{Q} = \frac{1}{\pi R_{2,fr1} C} = \frac{1}{\pi \cdot 6.36 \text{ M}\Omega} \approx 5 \text{ Hz}. \quad (55)$$

$$A_r = -2Q^2 \quad (56)$$

The filter of the directional flux voltage signal has a resonance frequency of $f_{r2} = 4000 \text{ Hz}$ and a gain factor of $A_r = -1$. With the Equations 52, 53 and 54, used above, the following resistance values are obtained to realize the second filter with the resonance frequency f_{r2} :

$$\begin{aligned} R_{1,fr2} &= 39.2 \text{ k}\Omega \\ R_{2,fr2} &= 80.6 \text{ k}\Omega \\ R_{3,fr2} &= 196 \text{ }\Omega \\ B_{fr2} &\approx 395 \text{ Hz} \end{aligned} \quad (57)$$

The signal processing circuit needs a symmetrical voltage supply of $V = \pm 15 \text{ V}$. The voltage is delivered by an external PCB which was developed in the bachelor's thesis [31]. The voltage supply board is shown in Appendix A.1 and is optimized for a ripple-free symmetrical voltage. The board fulfills the following features:

- electronic ripple filtering of full bridge rectifier voltage,
- passive 2nd order filtering of step-down converters,
- electromagnetic compatibility (EMC) designed board.

Before the implementation of the signal processing circuit, the correct function is checked by using a spice simulation. For this purpose, the following circuit is shown in Figure 35. As voltage input, a square wave signal with a frequency of 4000 Hz, an amplitude of 40 V_{pp} and a superimposed 50 Hz sinusoidal signal with an amplitude of 5 V are used.

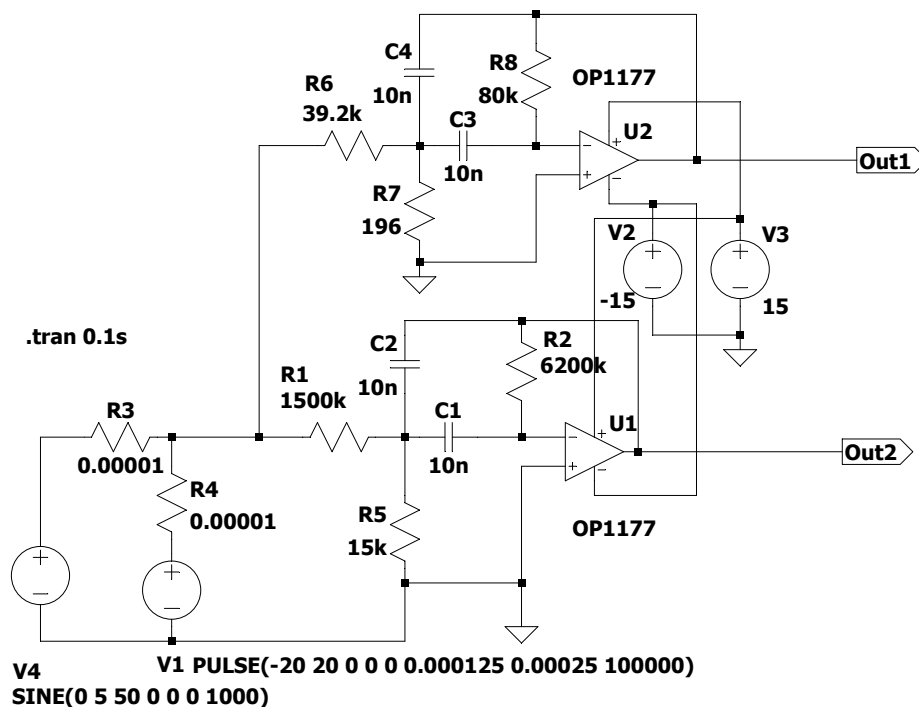


Figure 35: Spice circuit of bandpass filters.

Figure 36 shows the simulated signal waveforms. The blue curve indicates the superimposed input voltage, which corresponds to the induced voltage across the pickup coil. The orange curve represents the output signal with a frequency of 4000 Hz. In the first 2 ms a transient response of the circuit is clearly visible. The violet curve corresponds to the 50 Hz signal. The previously discussed gain factors $A_r = -2$ for 50 Hz bandpass respectively $A_r = -1$ for 4000 Hz bandpass are correctly simulated. Due to the successful simulation, signal processing can be implemented with these two filters on the board.

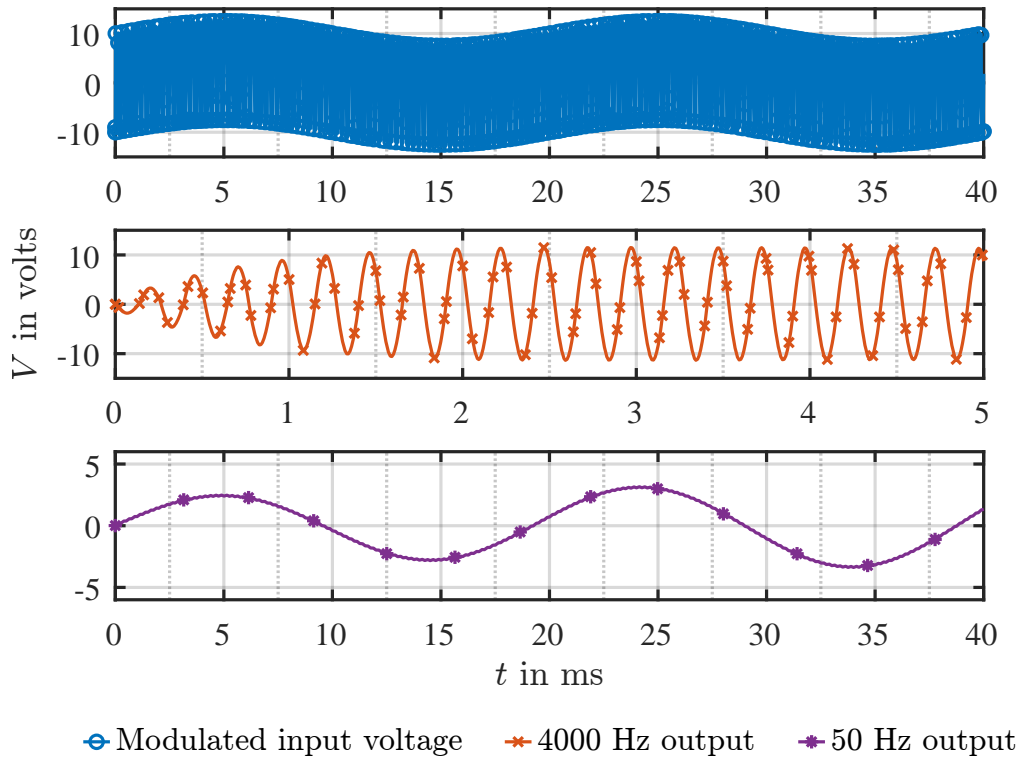


Figure 36: Simulated signal waveforms of bandpass filters.

3.3 Improvements

During an initial test of the H-bridge, it was noticed that the over-current protection of the used laboratory power supply no longer operates properly. The generated square wave voltage also sends pulses in the direction of the supply source. Due to these pulses, the laboratory power supply unit can no longer calculate the current correctly. Thereby the overcurrent protection gets a not conclusive signal and interrupts the current cyclically. To prevent this behavior, a second-order low pass filter is additionally implemented on the board. The calculation of the inductivity and capacitance are shown in the following Equation 58.

$$C = \frac{1}{L \cdot (f_c \cdot 2\pi)^2} = \frac{1}{100 \mu\text{H} \cdot (500 \text{ Hz} \cdot 2\pi)^2} \approx 1000 \mu\text{F} \quad (58)$$

To achieve a cut-off frequency of $f_c = 500 \text{ Hz}$ an inductance with $100 \mu\text{H}$ and a capacitor with $1000 \mu\text{F}$ is needed.

Capacitor Discharge Circuit

With the circuit shown in Figure 37 it is possible to discharge the supply stability capacitor $C1$ within 1 second to a lower voltage level.

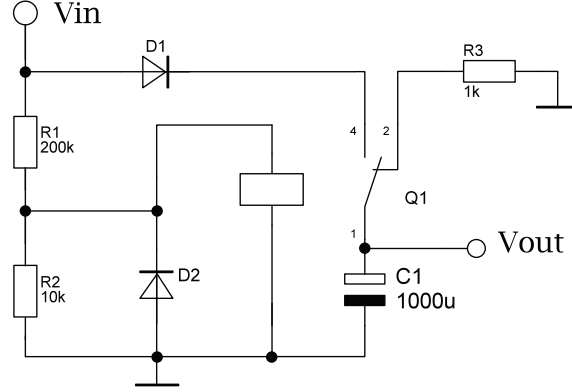


Figure 37: Discharge switch circuit.

$$E_{\text{cap}} = \frac{1}{2} \cdot V_{\text{supply}}^2 \cdot C = \frac{1}{2} \cdot (66 \text{ V})^2 \cdot 1000 \text{ } \mu\text{F} \approx 2.2 \text{ J} \quad (59)$$

$$\begin{aligned} V(1) &= V_{\text{supply}} \cdot e^{-\frac{t}{RC}} = \\ &= 66 \text{ V} \cdot e^{-\frac{1}{1 \text{ k}\Omega \cdot 1000 \text{ } \mu\text{F}}} \approx 24.3 \text{ V} \end{aligned} \quad (60)$$

Although the experimental setup is in a high-voltage test cell, and the stored energy in the capacitor is reduced during the time it takes to get into the test cell, this circuit ensures that the capacitor is safely and quickly discharged.

Due to the discharge, the resistor must have a certain thermal load capacity. To calculate the power the resistor must withstand, Equation 61 is used.

$$P_{\text{resistor}} = \frac{V_{\text{supply}}^2}{R} = \frac{(66 \text{ V})^2}{1 \text{ k}\Omega} \approx 4.4 \text{ W} \quad (61)$$

Although this power only has to be withstood during the first moments, a resistor with a maximum power dissipation of 5 W is selected.

3.4 Prototype PCB

For the experimental setup, the circuit is built on a breadboard, in order to have certain flexibility for improvements or additional components. The board itself also provides a supply for two fans to cool the MOSFETs of the H-bridge and the additional resistor R_1 of the sensor. In addition, two buttons are attached to the board, which are used to activate and deactivate the excitation.

During laboratory tests, it is helpful to get a quick indication of the condition of the test setup. Since the board is located in the high-voltage test cell, it is not possible to measure any inconsistencies immediately. For a quick status display, three status light emitting diodes (LEDs) are provided, which describe the following states:

1. green LED: indicates available source voltage V_{source} ,
2. yellow LED: indicates available control voltage for the MOSFETs,
3. red LED: indicates current excitation of the sensor.

Figure 38 depicts a top view of the used circuit board. On the left side of the breadboard the supply for different voltage levels (66 V for H-bridge supply, 12 V for MOSFET control, and 5 V for MCU supply), the excitation control and the H-bridge is placed. The signal processing is located on the right side of the board to prevent possible interference.

As discussed previously, a breadboard is used due to its flexibility, although it also has major drawbacks, such as poor solder joints, use of large components, and long wiring paths that significantly decrease EMC. In order to minimize the parasitic inductances of long wire connections, all voltage-carrying wires were twisted with a GND wire on the bottom side of the board. In general, attention was paid to short cable runs.

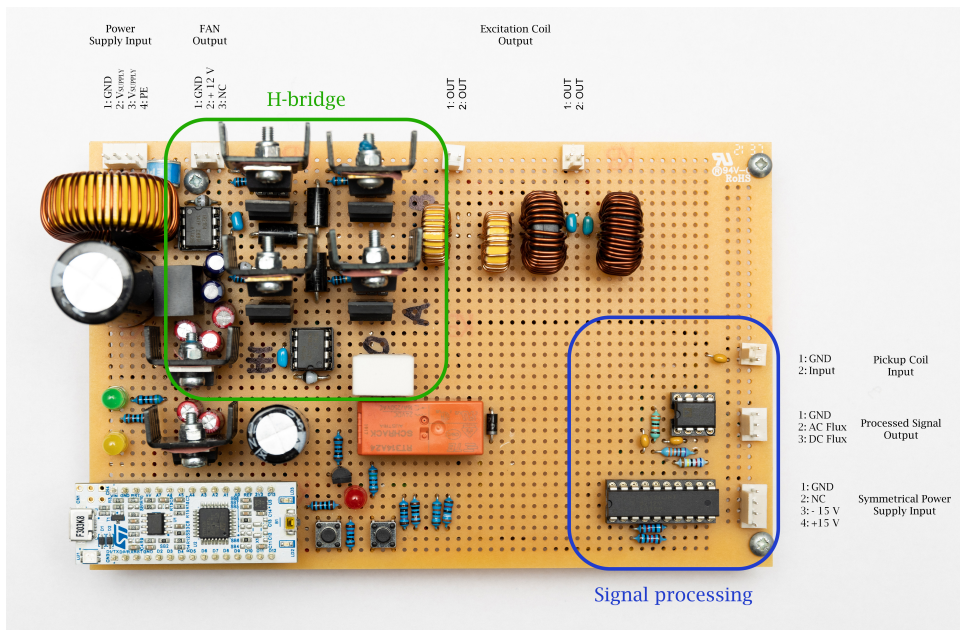


Figure 38: Top view of prototype PCB.

The following Figure 39 shows the final test setup in the laboratory, with the fluxgate sensor placed at the yoke of the five-leg transformer. On the left side of Figure 39 the search coils for detecting the alternating flux in the yoke are visible. In the lower area, the current transformer and the PCB can be identified for the excitation.

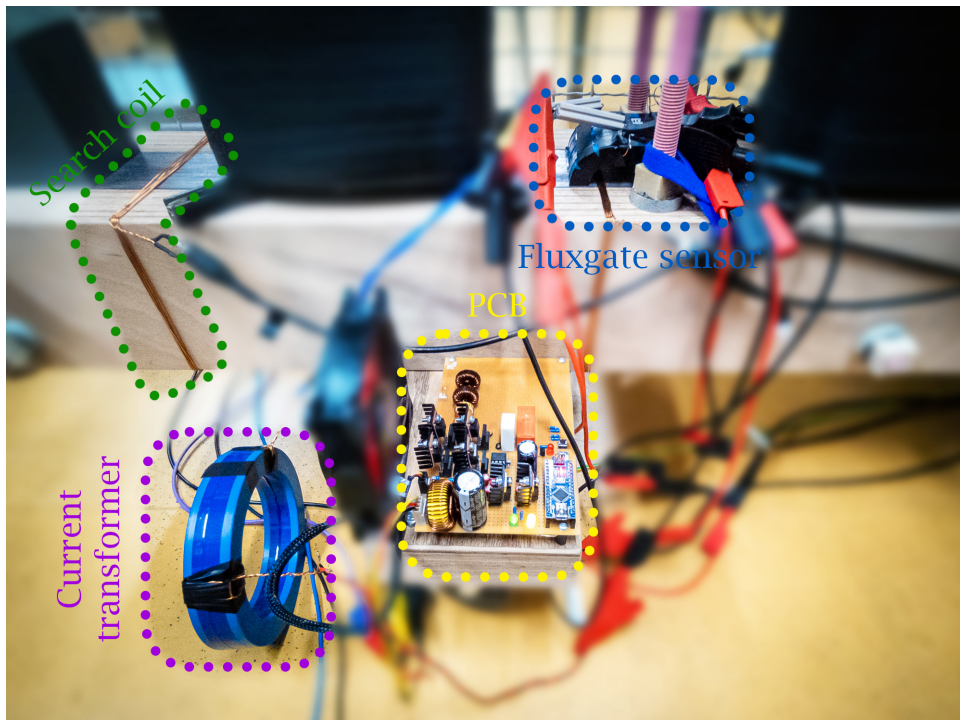


Figure 39: Prototype sensor setup.

4 Sensor Proof-of-concept Laboratory Test

4.1 Measurement Setup

The sensor prototype is mounted on a laboratory transformer to prove its functionality. Therefore the two sensor rods are placed on a transformer yoke of a 60 kVA five-leg laboratory transformer (T1) without a tank. Figure 40 depicts the schematic of the measurement setup. Transformer 1 is energized on the primary side with a power amplifier and on the secondary side connected to a 50 kVA three-leg power transformer through a start-star connection. A constant magnetic flux inside the transformer core is achieved with a superimposed DC source, which is connected between the two neutral points (the high-voltage side of the first transformer to the low-voltage side of the second transformer). The direct current is generated through a variable isolating transformer with a connected full bridge converter.

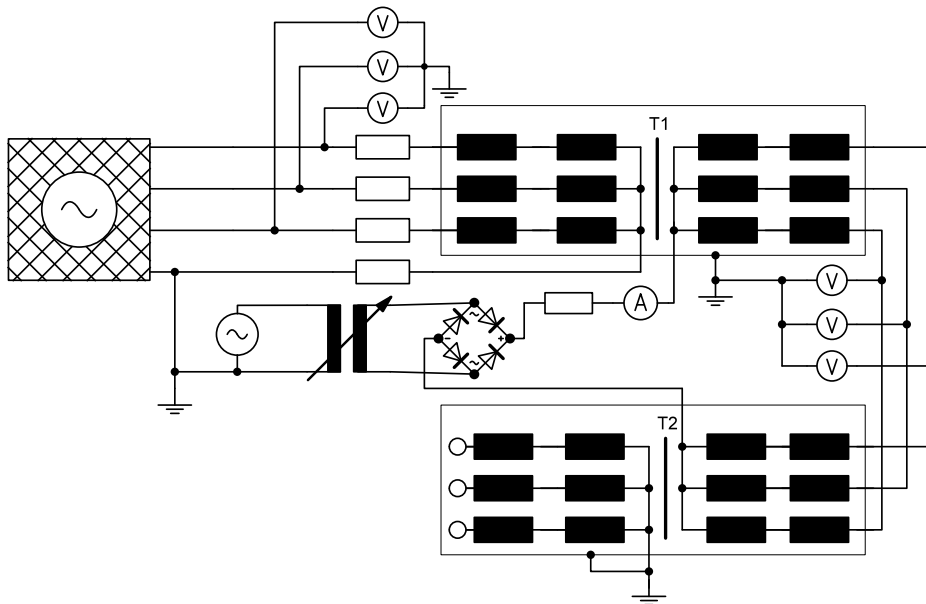


Figure 40: Schematic of measurement setup with two transformers and a superimposed DC.

During the test, the supply (current and voltage) of the laboratory transformer and the supply of the fluxgate sensor (current and voltage) are measured. For the excitation current measurement, the voltage drop across the additional resistor R_1 is used (see Chapter 3.1). The current measurement of the transformer supply is calculated using alternating current (AC) current clamps. The induced voltages in all five search coils (four at the lab transformer and one at a sensor rod) are recorded. To prove the correct behavior of the implemented signal processing, the pickup voltage is measured before and after the signal processing. In addition, the output signals of the signal processing for the alternating and direct flux are recorded. The injected current between the neutral points is recorded via AC/DC current clamp.

Before each measurement with a superimposed DC, the transformers are demagnetized. All magnetic paths have to be driven into saturation. A three-leg and a five-leg transformer are used, which have a different demagnetization process. The demagnetization of the three-leg transformer is carried out with the help of a periodic polarity-changing increasing rectangular curve, also called toggling DC. This supply is provided by a demagnetizing device by means of power electronics, which is connected to the B-N terminals of the three-leg transformer. For the five-leg variant, it is first necessary to short-circuit the terminals A-N and C-N and demagnetize via terminals B-N and next demagnetize through A-N, B-N, and C-N in parallel. Afterward short circuit the B-N terminal and demagnetize through A-C. Further information about this topic can be found in [10].

A recent sweep frequency response analysis (SFRA) and winding resistance analysis of the five-leg transformer revealed that the three main legs (phases A, B, and C) are no longer symmetrical. This means that the winding resistance of the middle leg (phase B) is higher than that of phases A and C. It must be assumed that the demagnetization prior to the measurements was not successful. The SFRA method applies a sinusoidal voltage with varying frequency to one phase of an investigated transformer. With the help of two voltage measurements, the voltage curve V_{ref} on the phase to be examined and the voltage curve V_{ref} on the other side of the phase winding (neutral point) are measured. The measurement setup is depicted in Figure 41. The transfer function is formed from the ratio between $V_{\text{meas.}}$ and $V_{\text{ref.}}$ [32]

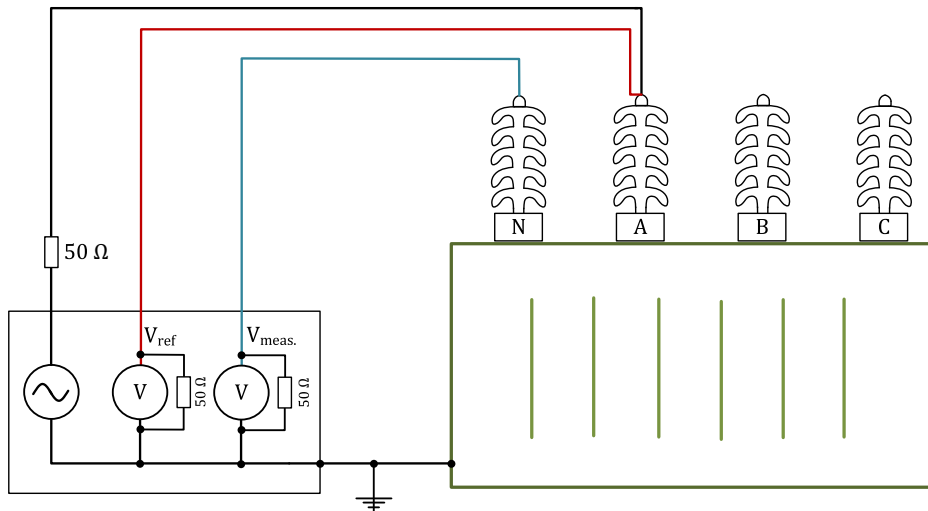


Figure 41: Schematic of SFRA measurement setup [32].

In the laboratory test, two transformers are connected to each other. To illustrate which components can cause a leakage flux, the following equivalent circuit diagram shows the hysteresis

model, investigated by [10]. For simplification, only phase A of the five-leg transformer (T1) and the three-leg transformer (T2) is shown. It can be noted that the reactance of the legs L_{Leg} and yokes L_{Yoke} have hysteretic behavior. The air gap reactance L_{gap} , which occurs during the layering of the transformer core at the joints, has a saturation behavior.

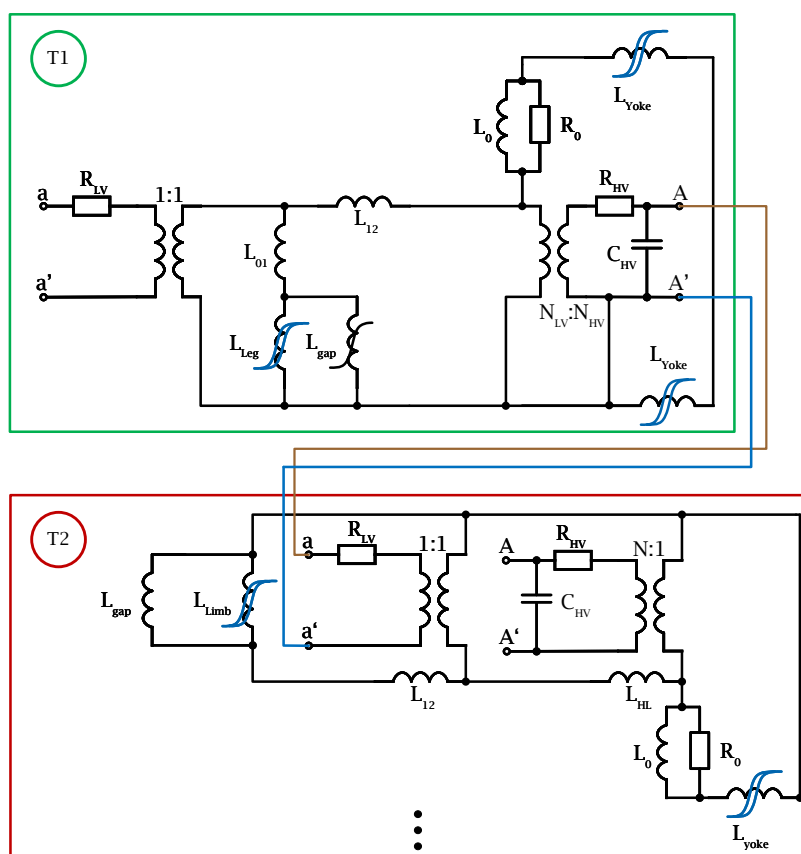


Figure 42: Hysteresis model of connected five- and three-leg transformers [10].

4.2 Ramp superimposed DC Test

The first test is a superimposed stepped DC current in the range ± 1.5 A injected via the two neutral points. All relevant signal waveforms are recorded by a power analyzer with a sampling rate of 200 kHz. Figure 43 depicts the recorded waveforms of the direct and superimposed DC. The blue curve represents the direct magnetic flux signal, which is the output voltage of the signal processing circuit on the PCB. In MATLAB only the integral of the signal was calculated, (see Chapter 3.2.2).

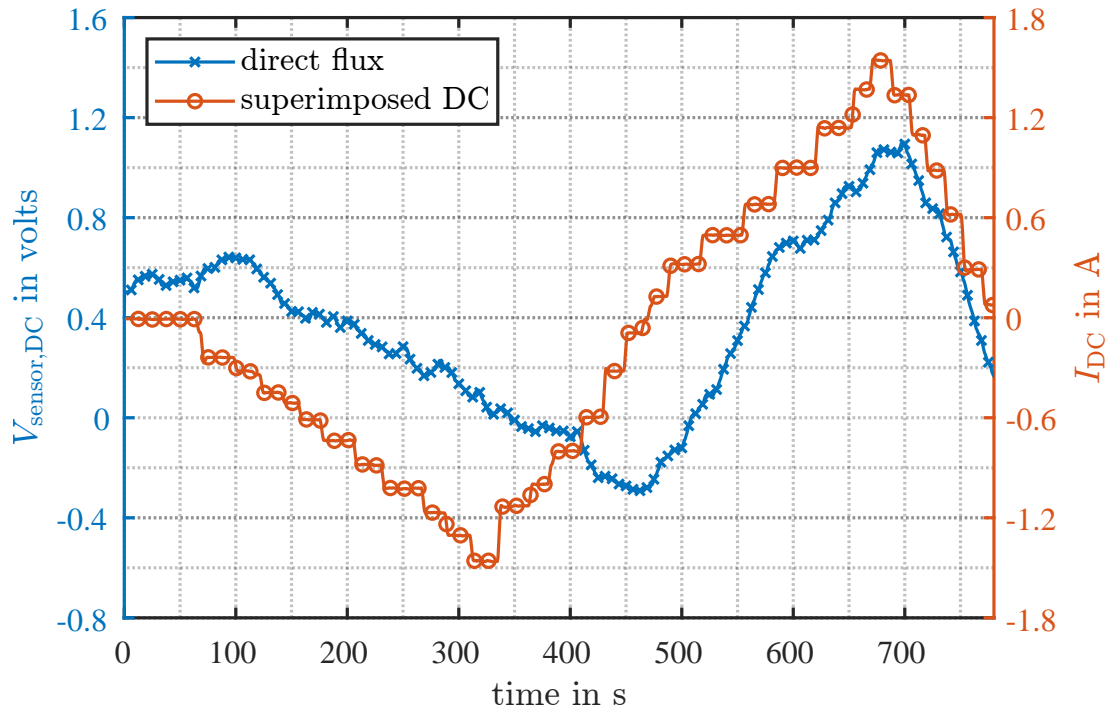


Figure 43: Superimposed DC ramp test.

The measured sensor output approximately follows the course of the superimposed current. It was noticed during the measurement that the five-leg transformer goes close to core saturation from an injected current of approximately $I_{DC} = 0.8$ A. When the magnetic field is passing from the core material into the air, the sensor receives a much greater magnetic field, in comparison to an idle transformer state. For this reason, the measurable amplitude becomes larger. The transition of the flux measurement from the main flux to the leakage flux is not linear and must therefore be taken into account when calibrating the sensor. Further explanations about this topic are given in section 2.2.2

4.3 Long superimposed DC Test

Due to the previously stepwise increased induced DC current, each amplitude rise forces a change in the magnetic flux. With each step, balancing processes also occur in the core. These are reflected a certain amount in the measured signal, which makes it difficult to interpret the signal waveform. For a better interpretation of the sensor behavior and the measurement signals, the step response of the measured magnetic flux is considered. For this purpose, the direct current is superimposed for approximately five minutes once to a current amplitude of 1 A and once of -1 A. Figure 44 depicts the measured and processed direct flux signal (blue curve) and the two superimposed DC steps (orange curve).

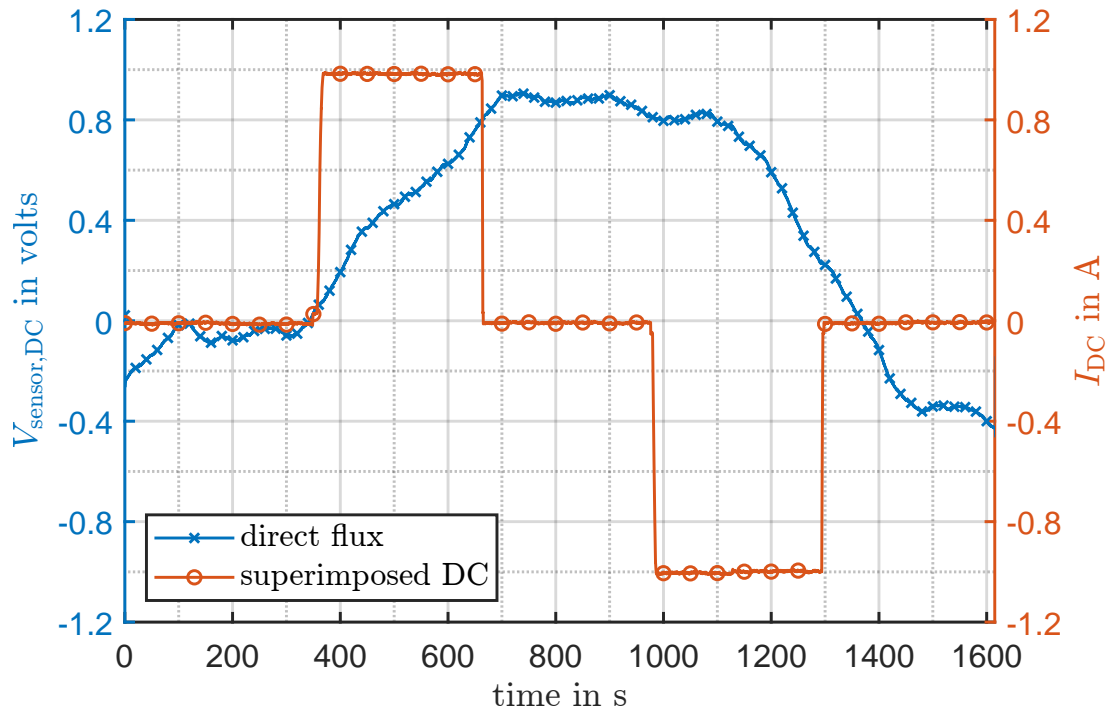


Figure 44: Superimposed DC step.

This measurement provides a clearer picture of how the measured voltage, equivalent to the external magnetic field of the transformer, behaves during the current superposition. Towards the end of the test, the voltage signal adjusts to a lower static value. Despite the demagnetization, a certain remanent flux must therefore still have been present in the core material. Due to the superimposed current this remanent flux is expected to be affected.

Alternating magnetic Flux Investigation

During the laboratory tests, the induced voltages across the search coils, one wound around the transformer yoke, and one around one sensor half are compared. Figure 45 depicts the amplitude comparison between the magnetic flux inside the transformer core and the magnetic flux through one sensor rod. In this case, the 50 Hz flux is considered, therefore root mean square (RMS) values are depicted.

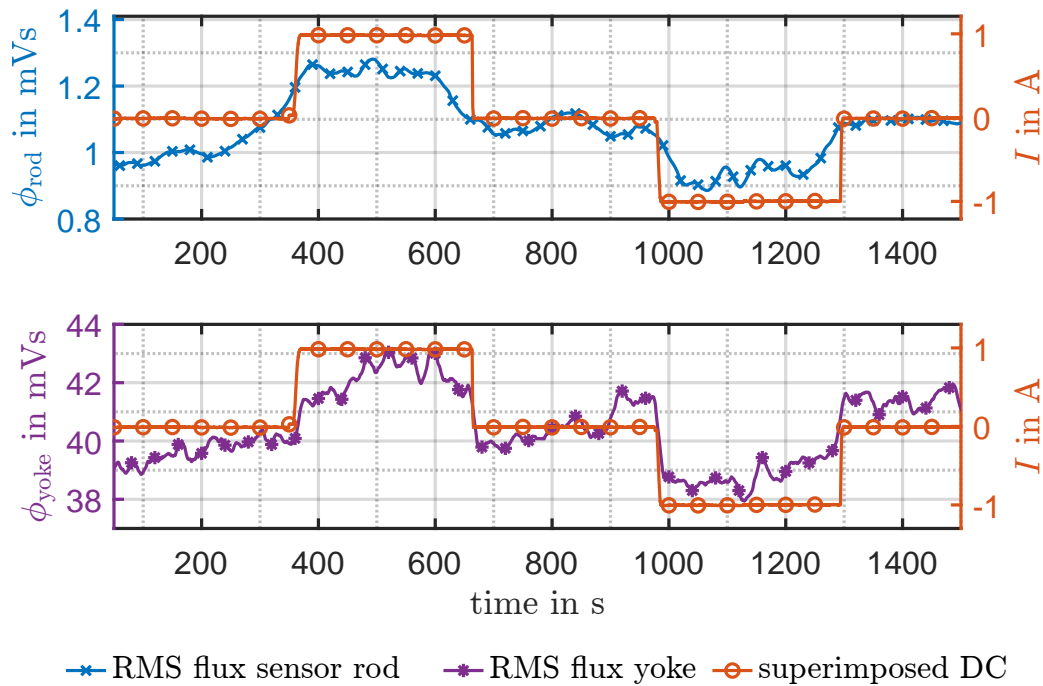


Figure 45: Comparison between alternating flux through transformer yoke and sensor rod.

The comparison showed that both amplitudes of the induced voltages increase in a similar ratio during a superimposed DC. The amplitude of the voltage signal from the sensor search coil is on average lower by a factor of 39. This ratio can be improved by a more suitable geometrical sensor shape (see Chapter 2.2.4).

Phase Shift Investigation

Figure 46 shows the waveforms of the induced voltages across the search coils. This measurement can only be performed when the sensor is not excited, otherwise, the superposition of the external magnetic flux and magnetic flux of the excitation would be measured and therefore no conclusion on the phase shift could be drawn, as described in Chapter 2.

A phase shift between the two signal waveforms is observed. This may be due to the different magnetic field types experienced by the search coils. The winding around the transformer yoke observes the main flux of the transformer. Only a part of the main flux runs through the parallel path of the fluxgate sensor and the larger part is the leakage flux of the transformer. The amplitude depends on the saturation state of the transformer. This can be determined via the operating point in the hysteresis curve. The main flux can be divided into a normal and a tangential component. Whereby the sensor experiences more of the tangential component compared to the yoke winding.

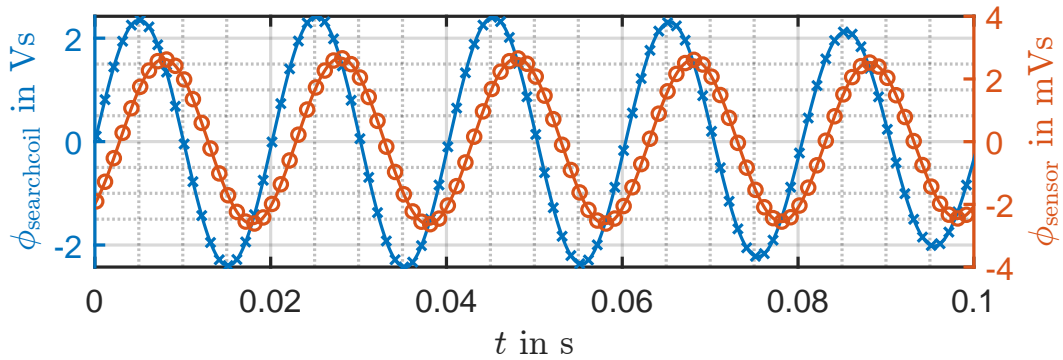


Figure 46: Phase shift between two search coils, wound around transformer yoke and sensor rod.

The phase shift of the two waveforms can be calculated with the following Equation 62.

$$\Delta t = 0.008 \text{ s} \rightarrow \varphi = \frac{\Delta t}{\frac{T}{2} \cdot \pi} = \frac{0.008 \text{ s}}{0.01} \cdot \pi = 2.51 \text{ rad} \triangleq 144^\circ \quad (62)$$

The past signal recording represents only one operating point of the transformer. In order to investigate the phase shift in more detail, another measurement is carried out. A DC current will also be injected via the neutral points. Both transformers are not energized. Figure 47 shows the phase shift of the induced voltage φ_{yoke} across the yoke search coil and the induced voltage φ_{rod} across the search coil wound around one sensor rod.

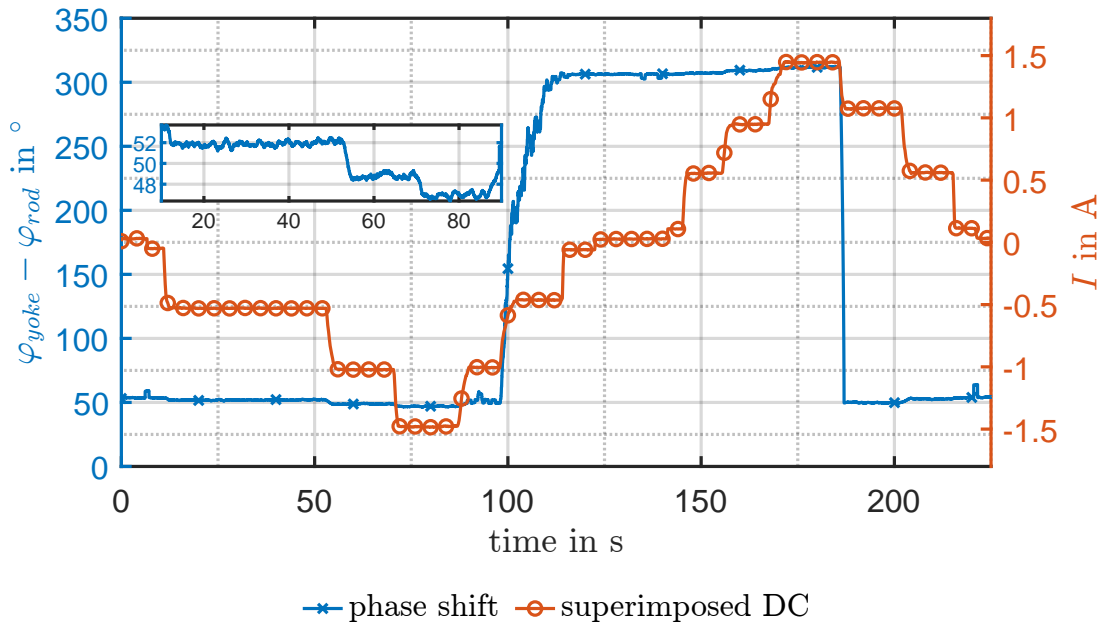


Figure 47: Phase shift between induced voltages across the search coil around the transformer yoke and the search coil around one sensor rod.

For each amplitude increase of the superimposed DC the phase shift between φ_{yoke} and φ_{rod} changes. As soon as the sign of the slope of the superimposed DC changes, it is clearly visible how the phase shift rotates by 360° , with a small delay. When the sign of the slope changes again, the phase shift rotates again by 360° to the original angle. The absolute value of the phase shift also depends on the magnitude of the superimposed current. From experience, it is known that the five-leg transformer is already in the non-linear range of the hysteresis curve with a superimposed current of $I_{\text{DC}} = 0.8$ A. This would also explain why the change of the phase shift is higher, the higher the amplitude of the superimposed DC is.

The phase shift has to be caused by the different flux types, as explained in more detail in Chapter 2.2.4. The leakage flux causes a higher shift between φ_{yoke} and φ_{rod} than part of the main flux.

Moreover, it must be taken into account that the stray reactances L_σ of the transformer are not linear. This implies that the higher the magnetic field strength H , the wider, in geometrical terms, the field curves become. A longer field path means a longer magnetic path l_m , which leads to a higher reluctance R_m . It can be assumed that the leakage reactance L_σ of the transformer depends on the magnetic field strength H , as shown in the following equation:

$$L_\sigma = f(H). \tag{63}$$

5 Conclusion and Outlook

5.1 Conclusion

By means of the fluxgate principle and control by a H-bridge it is possible to measure a constant and alternating magnetic flux in power transformers. It is important that suitable ferromagnetic materials are used for the sensor rods, which can be quickly driven into saturation and generate a high-quality measurement signal. A benefit of this measurement method is the ability to measure constant magnetic flux without an alternating flux, in case of a de-energized operation state. In addition, the transformer design is not affected by the sensor. Additional benefits of the sensor include the following:

1. possibility of alternating, direct and remanent flux monitoring,
2. non-invasive method for the transformer,
3. very low temperature dependence,
4. very compact sensor size,
5. low material usage compared to conventional measuring methods (Chapter 2).

The investigated nanocrystalline cores convinced by their magnetic properties. They enabled to build the sensor by using the fluxgate principle. Furthermore, the cores would be ideally suited for use in power transformers due to their oil resistance, very low-temperature drift, small size, and low influence on the magnetic properties due to external forces, according to the datasheet (Appendix B.1) and [21]. If the transformer core material and its dimensions are known, the sensor can be optimally matched to the transformer in order to achieve the highest possible sensitivity.

The proof-of-concept test (Chapter 4) has shown that the sensor has to be calibrated to the transformer to obtain a correct value of the magnetic flux. Using a lookup table (LUT), the sensor can be calibrated to the transformer and the mentioned non-linear transition (Chapter 2.2.2) between a part of the main flux and much higher leakage flux, experienced by the rods, can be taken into account.

5.2 Future Research and Improvements

In the thesis, it was proved that the sensor can be used for direct and alternating magnetic fluxes in transformers. For the most accurate and reliable indication of the flux conditions, the following improvements should be applied to the sensor:

- additional feedback winding for zero flux state inside sensor rods,
- investigation of the influence of the sensor placement on the transformer core,

- fabrication of a surface mounted devices (SMD) PCB to increase EMC,
- implementation of a field programmable gate array (FPGA) that controls the excitation and handles the signal processing,
- use of an even higher permeable magnetic core material to achieve greater reluctance difference between sensor rod and transformer yoke.

Remanent Flux Minimization

A future investigation could be the reduction of an existing remanent flux in order to keep the inrush current within certain limits during the energizing of large transformers. For this purpose, fluxgate sensors are placed in each yoke, as shown in Figure 48.

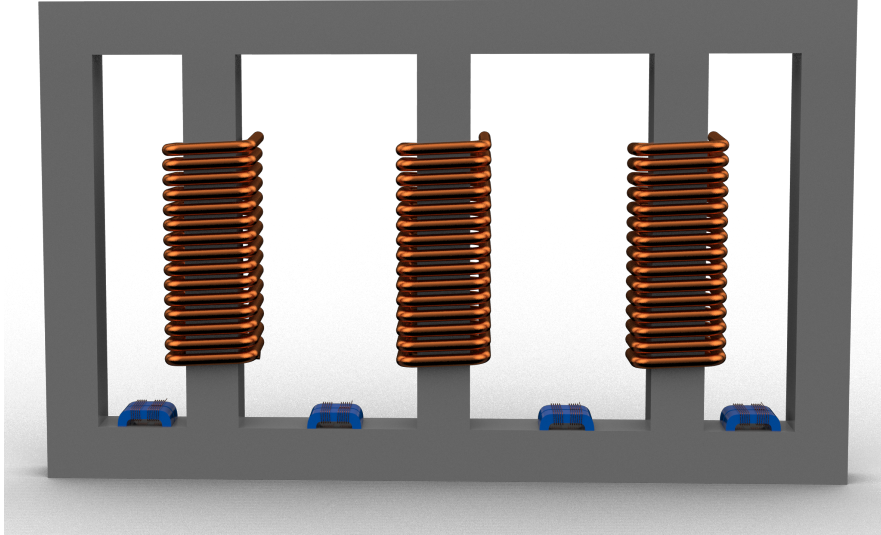


Figure 48: Five-leg transformer with flux sensor in each yoke.

Using the equation system, shown in Equation 64 which is formed from the magnetic node equations, all magnetic flux paths can be determined mathematically after measurement with the four sensors. The green underlined sums show the known values. Figure 49 depicts the used nodes A to F in the schematic representation of the five-leg laboratory transformer.

$$\begin{aligned}
 \phi_1 &= \phi_{01} + \phi_{AB} = \phi_{01} + \phi_{DE} \\
 \phi_2 &= \phi_{BC} - \phi_{AB} = \phi_{EF} - \phi_{DE} \\
 \phi_3 &= \phi_{02} - \phi_{BC} = \phi_{02} - \phi_{EF}
 \end{aligned} \tag{64}$$

With the measured flux conditions in the core, the remanent flux can be reduced with the help

of additional windings around each yoke. For this purpose, a pulsed current induces a flux in the opposite direction (see Chapter 2.1.4), which counteracts the remanent flux.

The advantage of this method is that with a reduced remanent flux, the amplitudes of the inrush currents are in the normal range during the switching-on process of the transformer. A direct flux inside the core can also be reduced by this method. Without a remanent and directional flux the transformer can exploit its full transmission power. In addition, the effects described in Chapter 2 due to unbalanced fluxes are avoided.

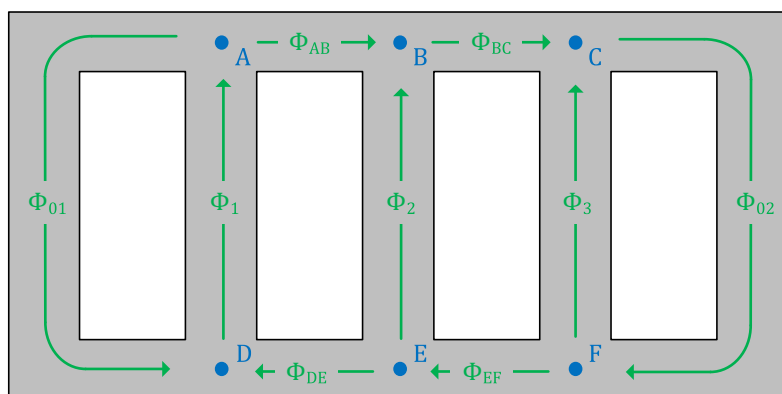


Figure 49: Magnetic flux paths inside five-leg transformer.

Feedback Winding and Zero Flux Condition

The stability of the sensor can be improved by an additional feedback winding. This coil causes a magnetic flux in the sensor rods, which counteracts the flux caused by an external field. In this case, a zero flux state is achieved, in which the measurement signal is derived from the magnitude of the opposing induced flux. A schematic block diagram of the sensor with this additional feedback coil is shown in Figure 50.

In addition, a large part of the excitation control and signal processing could be handled by an FPGA. As shown in the orange area in Figure 50. The advantage of this is a more flexible development and implementation of additional functionalities. In addition, the signal processing can be carried out more precisely, directly after an analog-digital conversion. Digital filters can also enable even better signal processing. The sensor signal could be presented directly on a display by the FPGA and it could also be processed for communication with a supervisory control and data acquisition (SCADA) system.

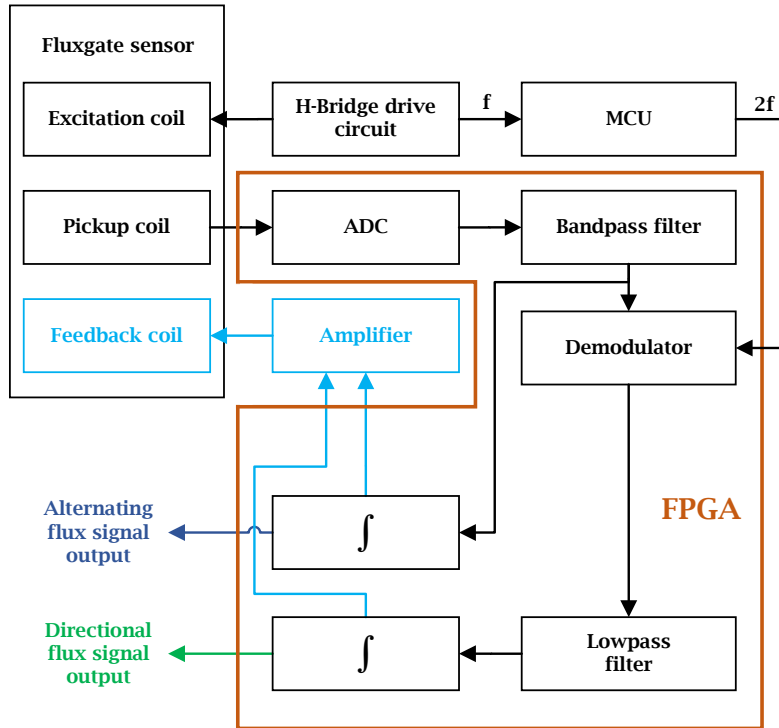


Figure 50: Schematic sensor control and signal processing with a FPGA.

PCB Design Improvements

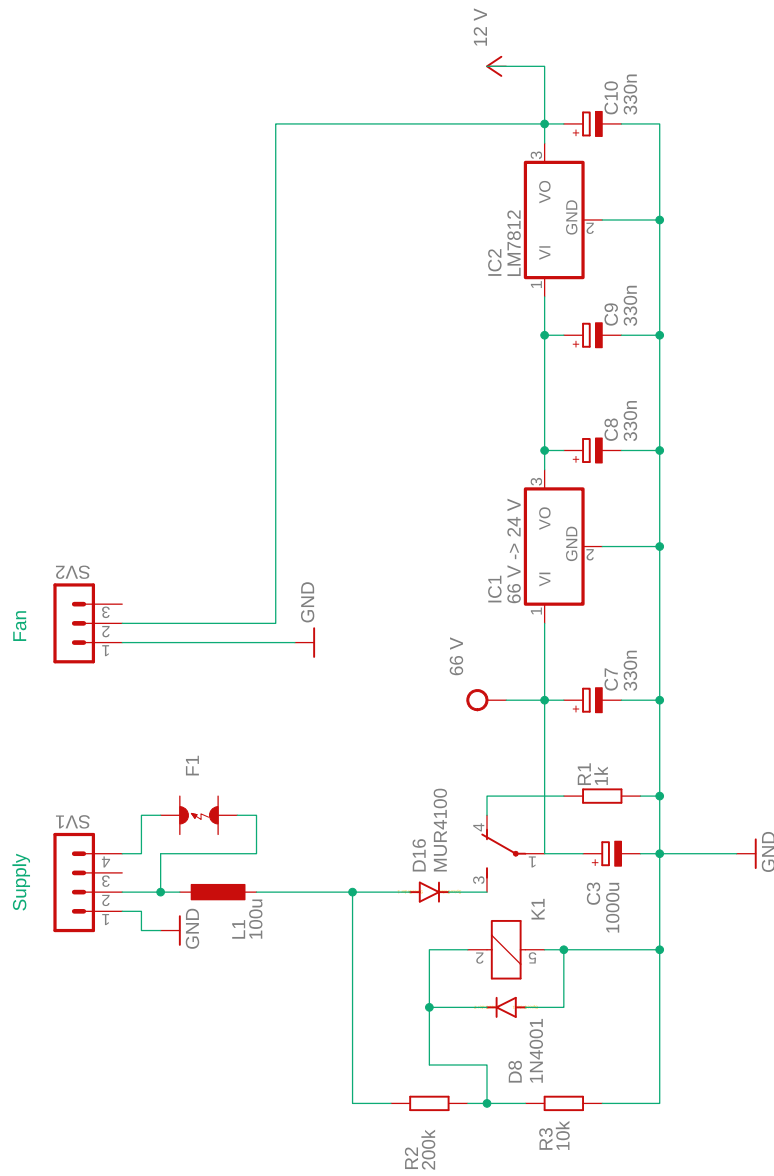
A further recommendation for improvement concerns the electronic circuit. Ideally, the circuit should not be mounted on a breadboard, but rather be manufactured on a PCB considering a SMD design. The previously mentioned FPGA, which takes over the tasks of excitation control and signal processing, can also be mounted directly on the board. The design should use the shortest possible wire paths and smaller components. A continuous ground layer would be necessary to improve the EMC.

The connection between the sensor and board will be several meters in real use, so for this connection, it is recommended to use shielded cables with twisted wire pairs, which keep the parasitic inductances as small as possible.

The circuit board could be modified so that the H-bridge generates a sinusoidal excitation voltage by using PWM. This has the advantage of eliminating many side effects of the square voltage. Since a square waveform is a superposition of infinite sine signals, higher frequencies cause interference in the measurement.

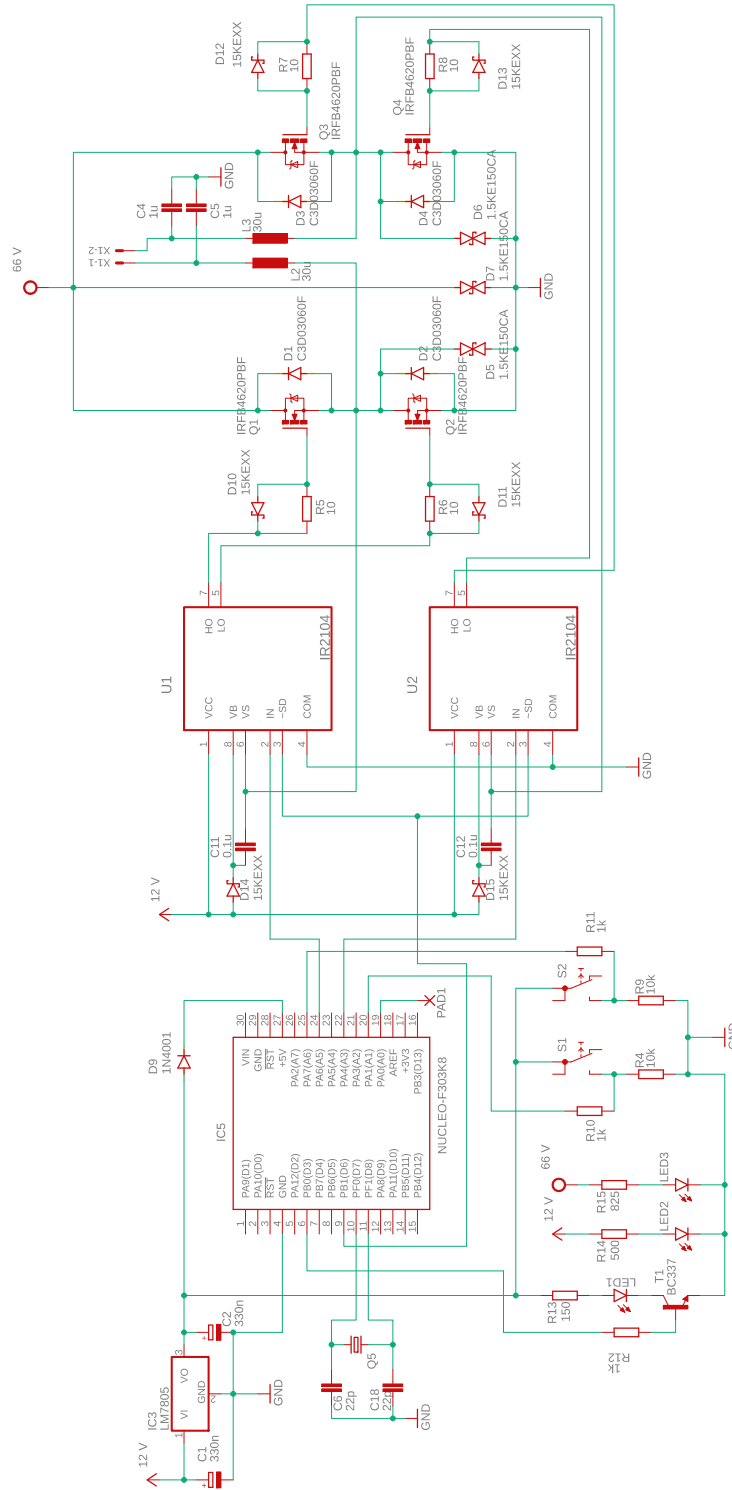
A Circuit schematic and electronic components

A.1 Supply Board



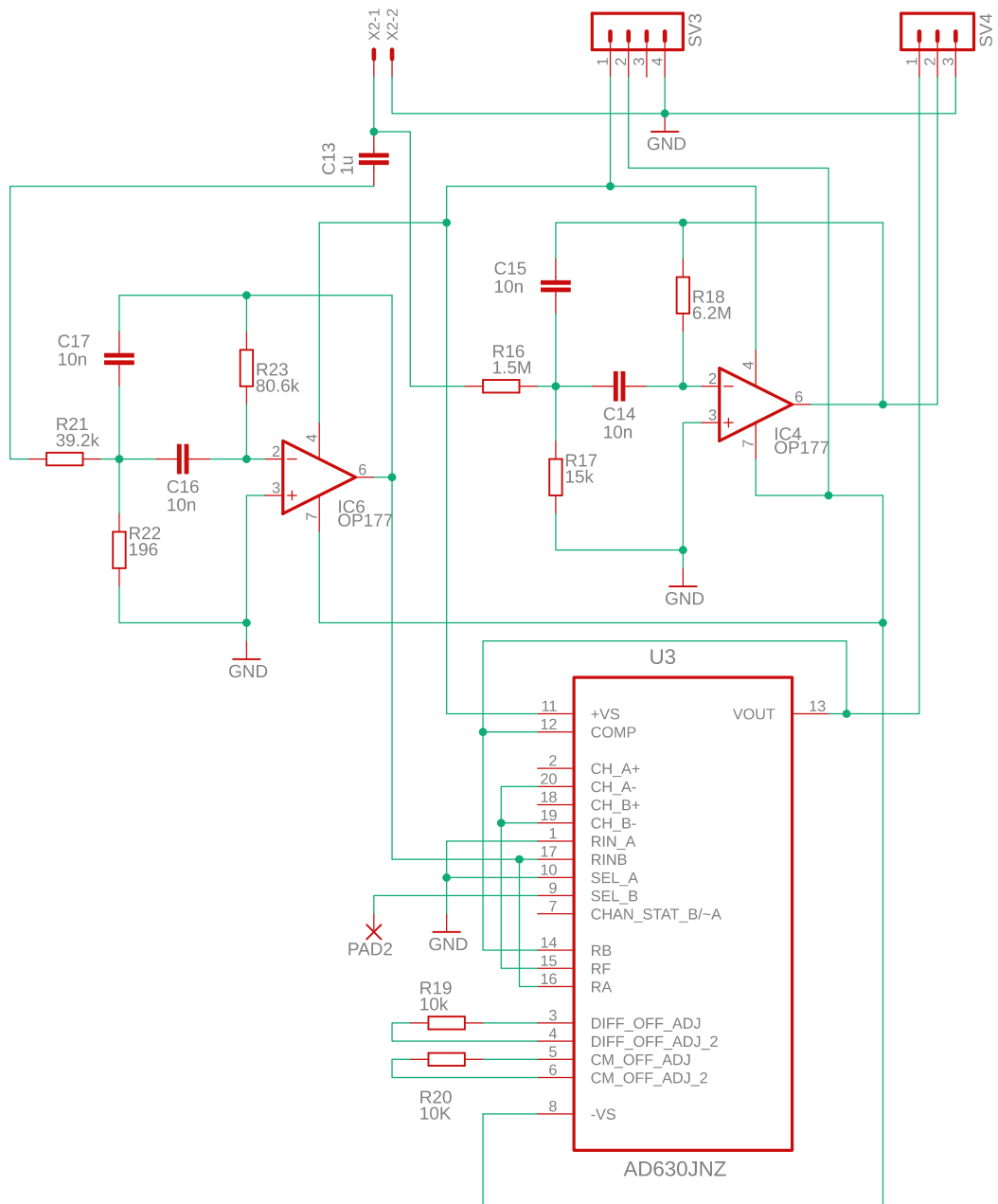
Appendix A.1: Supply circuit.

A.2 H-bridge Board



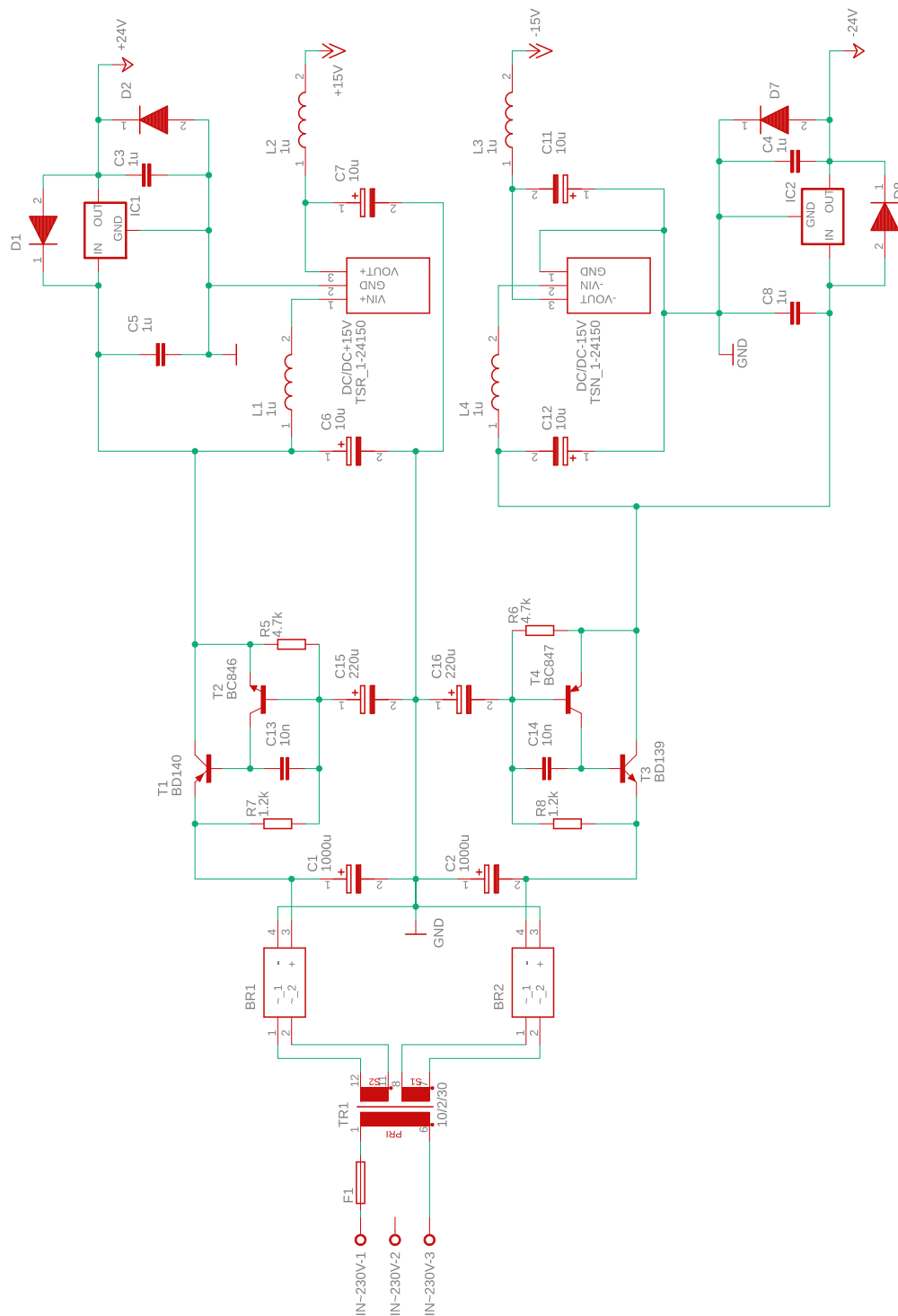
Appendix A.2: H-Bridge circuit.

A.3 Signal Processing Board



Appendix A.3: Signal processing circuit.

A.4 Symmetrical Voltage Supply Board



Appendix A.4: Symmetrical voltage supply circuit.

A.5 Electrical Components

Appendix 5: Used components of prototype board.

Part	Type	Manufacturer	Name/Value/Model	Price (each) excl. VAT	Order-Nr.	Shop	
C1, C2, C7-C10	capacitor	Würth Electronic	330nF $\pm 20\%$ / 50V	€ 0,06	839-6605	RS	
C3		RS Pro	1000 μ F $\pm 20\%$ / 100V DC	€ 5,44	711-1769	RS	
C4-C5		RS Pro	Ceramic Capacitor 1 μ F, 50V	€ 0,15	180-5107	RS	
C6, C18		KEMET	22pF $\pm 5\%$ / 200V	€ 0,32	538-1461	RS	
C11-C13	diode	Vishay	199D 1 μ F, 35V dc	€ 1,25	830-9958	RS	
C14-C17		KEMET	THT 10nF $\pm 10\%$ / 100V	€ 0,31	538-1411	RS	
D1, D4		Wolfspeed	SiC-Schottky 600V / 5A, TO-220	€ 2,30	809-9023	RS	
D5-D7		Vishay	TVS bi-directional 207V 143V	€ 0,84	638-8716	RS	
D8, D9		Vishay	1N4001 50V / 1A	€ 0,25	628-8931	RS	
D14, D15, D10-D13		Vishay	ultrafast rectifiers diode 600V 1A	€ 0,63	700-3964	RS	
D16		onsemi	THT MUR4100 1000V / 4A	€ 1,01	625-5357	RS	
F1		gas discharge tube	EPCOS EHV	20kA, 90V	€ 3,41	191-1535	RS
IC1		step down converter	RS Pro	In: 36 - 90V DC / Out: 24V DC	€ 7,93	236-9853	RS
IC2		voltage regulator	STMicroelectronics	LM7812 1A, 1 TO-220, 3-Pin	€ 0,94	298-8586	RS
IC3	STMicroelectronics		LM7805 1A, 1 TO-220, 3-Pin	€ 0,94	298-8508	RS	
IC4, IC6	Analog Devices		Precision, Op Amp, 600kHz	€ 15,65	522-9385	RS	
IC5	MCU	STMicroelectronics	STM32 Nucleo-64 MCU STM32L412KB	€ 10,54	182-7763	RS	
K1	relay	TE Connectivity	24 V DC Power Relay - 16A	€ 6,41	515-559	RS	
L1	inductance	RS Pro	PowerCore, 100 μ H, $\pm 15\%$, 5A	€ 1,53	104-8443	RS	
L2, L3		Tamura	Ferrite Inductor 5A Idc, 27m Ω Rdc, GLA-05	€ 7,53	154-1202	RS	
R1		TE Connectivity	SQM5 1k Ω , $\pm 5\%$, metaloxid, 5W	€ 0,77	199-7832	RS	
R2		TE Connectivity	200k Ω , $\pm 0,1\%$, metal film 0.25W	€ 0,64	754-8789	RS	
R3, R4, R9, R19, R20	resistor	RS PRO	10k Ω $\pm 5\%$ carbon film 0.25W	€ 0,20	707-7745	RS	
R5-R8		TE Connectivity	10 Ω , $\pm 0,1\%$, thin film 0.25W	€ 0,56	137-2768	RS	
R10-R12		RS PRO	1k Ω $\pm 0,5\%$ / 0.25W	€ 0,06	174-3038	RS	
R13		TE Connectivity	150 Ω $\pm 0,1\%$ / 0.25W	€ 0,64	755-0934	RS	
R14		Arcol	499 Ω $\pm 0,1\%$ / 0.25W	€ 1,55	487-5511	RS	
R15		TE Connectivity	825 Ω $\pm 0,1\%$ / 0.25W	€ 0,64	754-6960	RS	
R16		Vishay	1.5M Ω $\pm 5\%$ / 0.25W	€ 0,16	683-5275	RS	
R17		TE Connectivity	15k Ω $\pm 0,1\%$ / 0.25W	€ 0,64	755-0959	RS	
R18		Vishay	6, 2M Ω $\pm 1\%$ 0.6W	€ 0,06	506-5894	RS	
R21		Arcol	39.2k Ω $\pm 0,1\%$ / 0.25W	€ 0,80	487-7781	RS	
R22	TE Connectivity	196 Ω $\pm 0,1\%$ / 0.25W	€ 0,64	755-1072	RS		
R23	TE Connectivity	80.6k Ω $\pm 0,1\%$ / 0.25W	€ 0,64	754-6954	RS		
S1, S2	switch	Omron	plunger 24V DC 50 mA	€ 0,35	794-4055	RS	
T1	transistor	onsemi	BC337 45 V / 800 mA 100 MHz	€ 0,29	671-1116	RS	
U1, U2	half bridge driver	International Rectifier	IR 2104 high and low side half bridge, 600 V	€ 1,13	IR 2104	Reichelt	
U3	demodulator	Analog Devices	AD630JNZ 2MHz	€ 33,70	183-1922	RS	
Q1-Q4	MOSFET	Infineon	IRFB4620PBF N-Kanal	€ 0,32	257-9353	RS	
Q5	oscillator	QANTEK	16MHz $\pm 20ppm$, 18pF	€ 0,24	814-9440	RS	

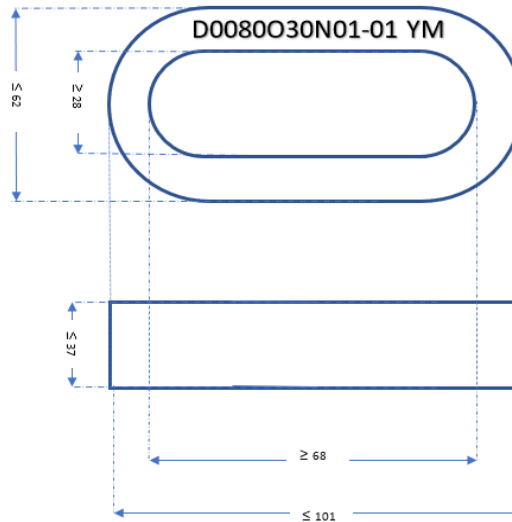
B Datasheet

D0080030N01-01 YM (YM is Year / Month)

House	Material	Permability:	Frequency	H peak	Lfe	Afe	Packaging
Cased	Nanocrystalline	30000	10 kHz	3,12	22,4	1,9	6 pcs. each layer
Round	Nominal values			mA/cm	cm	cm ²	12 pcs. Pr. box

Inspection values	Measurement limits	Frequency	leff x N (mA x turns)
AL (uH)	24,1 - 48,2	10 kHz	10 kHz
AL (uH)	12 - NA	100 kHz	100 kHz

Dimensions in mm	Round core	Outer	Inner	Height	Weight in gram
Nominal values	80x63x30				335



Index	Revision	Comments	Date
01	01	Product released	16-02-2021

More information
<http://www.blueferrite.com>

	Created	Approved	Quality	Released
Name	HJP	MRO		HJP/MRO
Date	16-02-2021			



Appendix B.1: Data sheet of nanocrystalline oval core.

C Programming

```
#include "main.h"

/* Variables and constants -----*/
TIM_HandleTypeDef htim2;
TIM_HandleTypeDef htim3;

void SystemClock_Config(void);
static void MX_GPIO_Init(void);
static void MX_TIM2_Init(void);
static void MX_TIM3_Init(void);

int main(void)
{
    /* MCU Configuration -----*/
    HAL_Init();

    /* Configure the system clock */
    SystemClock_Config();

    MX_GPIO_Init();
    MX_TIM2_Init();
    MX_TIM3_Init();

    /* Start PWM Timers */
    HAL_TIM_PWM_Start(&htim2, TIM_CHANNEL_1);
    HAL_TIM_PWM_Start(&htim3, TIM_CHANNEL_1);
    HAL_TIM_PWM_Start(&htim3, TIM_CHANNEL_2);

    while (1)
    {
        if (HAL_GPIO_ReadPin(GPIOA, GPIO_PIN_1) == GPIO_PIN_SET) {
            HAL_GPIO_WritePin(GPIOB, GPIO_PIN_0, GPIO_PIN_SET);
            HAL_GPIO_WritePin(GPIOB, GPIO_PIN_1, GPIO_PIN_SET);
            HAL_Delay(100);
        }
        if (HAL_GPIO_ReadPin(GPIOA, GPIO_PIN_7) == GPIO_PIN_SET) {
            HAL_GPIO_WritePin(GPIOB, GPIO_PIN_0, GPIO_PIN_RESET);
            HAL_GPIO_WritePin(GPIOB, GPIO_PIN_1, GPIO_PIN_RESET);
        }
        HAL_Delay(10);
    }
}

void SystemClock_Config(void)
{
    RCC_OscInitTypeDef RCC_OscInitStruct = {0};
    RCC_ClkInitTypeDef RCC_ClkInitStruct = {0};

    RCC_OscInitStruct.OscillatorType = RCC_OSCILLATORTYPE_HSE;
    RCC_OscInitStruct.HSEState = RCC_HSE_ON;
    RCC_OscInitStruct.HSEPredivValue = RCC_HSE_PREDIV_DIV1;
    RCC_OscInitStruct.HSIState = RCC_HSI_ON;
    RCC_OscInitStruct.PLL.PLLState = RCC_PLL_ON;
    RCC_OscInitStruct.PLL.PLLSource = RCC_PLLSOURCE_HSE;
    RCC_OscInitStruct.PLL.PLLMUL = RCC_PLL_MUL4;
    if (HAL_RCC_OscConfig(&RCC_OscInitStruct) != HAL_OK)
        {Error_Handler();}
    /** Initializes the CPU, AHB and APB buses clocks
    */
    RCC_ClkInitStruct.ClockType = RCC_CLOCKTYPE_HCLK|RCC_CLOCKTYPE_SYSCLK
        |RCC_CLOCKTYPE_PCLK1|RCC_CLOCKTYPE_PCLK2;
    RCC_ClkInitStruct.SYSCLKSource = RCC_SYSCLKSOURCE_PLLCLK;
    RCC_ClkInitStruct.AHBCLKDivider = RCC_SYSCLK_DIV1;
    RCC_ClkInitStruct.APB1CLKDivider = RCC_HCLK_DIV2;
    RCC_ClkInitStruct.APB2CLKDivider = RCC_HCLK_DIV1;
    if (HAL_RCC_ClockConfig(&RCC_ClkInitStruct, FLASH_LATENCY_2) != HAL_OK)
        {Error_Handler();}
}

static void MX_TIM2_Init(void)
{

```

```

TIM_ClockConfigTypeDef sClockSourceConfig = {0};
TIM_MasterConfigTypeDef sMasterConfig = {0};
TIM_OC_InitTypeDef sConfigOC = {0};

htim2.Instance = TIM2;
htim2.Init.Prescaler = 15;
htim2.Init.CounterMode = TIM_COUNTERMODE_CENTERALIGNED1;
htim2.Init.Period = 500;
htim2.Init.ClockDivision = TIM_CLOCKDIVISION_DIV1;
htim2.Init.AutoReloadPreload = TIM_AUTORELOAD_PRELOAD_DISABLE;
if (HAL_TIM_Base_Init(&htim2) != HAL_OK)
    {Error_Handler();}
sClockSourceConfig.ClockSource = TIM_CLOCKSOURCE_INTERNAL;
if (HAL_TIM_ConfigClockSource(&htim2, &sClockSourceConfig) != HAL_OK)
    {Error_Handler();}
if (HAL_TIM_PWM_Init(&htim2) != HAL_OK)
    {Error_Handler();}
if (HAL_TIM_OC_Init(&htim2) != HAL_OK)
    {Error_Handler();}
sMasterConfig.MasterOutputTrigger = TIM_TRGO_RESET;
sMasterConfig.MasterSlaveMode = TIM_MASTERSLAVEMODE_DISABLE;
if (HAL_TIMEx_MasterConfigSynchronization(&htim2, &sMasterConfig) != HAL_OK)
    {Error_Handler();}
sConfigOC.OCMode = TIM_OC_MODE_PWM1;
sConfigOC.Pulse = 250;
sConfigOC.OCpolarity = TIM_OCPOLARITY_HIGH;
sConfigOC.OCFastMode = TIM_OCFAST_ENABLE;
if (HAL_TIM_PWM_ConfigChannel(&htim2, &sConfigOC, TIM_CHANNEL_1) != HAL_OK)
    {Error_Handler();}
sConfigOC.OCMode = TIM_OC_MODE_ACTIVE;
sConfigOC.OCFastMode = TIM_OCFAST_DISABLE;
if (HAL_TIM_OC_ConfigChannel(&htim2, &sConfigOC, TIM_CHANNEL_2) != HAL_OK)
    {Error_Handler();}
HAL_TIM_MspPostInit(&htim2);
}
static void MX_TIM3_Init(void)
{
    TIM_ClockConfigTypeDef sClockSourceConfig = {0};
    TIM_SlaveConfigTypeDef sSlaveConfig = {0};
    TIM_MasterConfigTypeDef sMasterConfig = {0};
    TIM_OC_InitTypeDef sConfigOC = {0};

    htim3.Instance = TIM3;
    htim3.Init.Prescaler = 15;
    htim3.Init.CounterMode = TIM_COUNTERMODE_CENTERALIGNED1;
    htim3.Init.Period = 1000;
    htim3.Init.ClockDivision = TIM_CLOCKDIVISION_DIV1;
    htim3.Init.AutoReloadPreload = TIM_AUTORELOAD_PRELOAD_DISABLE;
    if (HAL_TIM_Base_Init(&htim3) != HAL_OK)
        {Error_Handler();}
    sClockSourceConfig.ClockSource = TIM_CLOCKSOURCE_INTERNAL;
    if (HAL_TIM_ConfigClockSource(&htim3, &sClockSourceConfig) != HAL_OK)
        {Error_Handler();}
    if (HAL_TIM_PWM_Init(&htim3) != HAL_OK)
        {Error_Handler();}
    sSlaveConfig.SlaveMode = TIM_SLAVEMODE_DISABLE;
    sSlaveConfig.InputTrigger = TIM_TS_ITR1;
    if (HAL_TIM_SlaveConfigSynchro(&htim3, &sSlaveConfig) != HAL_OK)
        {Error_Handler();}
    sMasterConfig.MasterOutputTrigger = TIM_TRGO_RESET;
    sMasterConfig.MasterSlaveMode = TIM_MASTERSLAVEMODE_DISABLE;
    if (HAL_TIMEx_MasterConfigSynchronization(&htim3, &sMasterConfig) != HAL_OK)
        {Error_Handler();}
    sConfigOC.OCMode = TIM_OC_MODE_PWM1;
    sConfigOC.Pulse = 250;
    sConfigOC.OCpolarity = TIM_OCPOLARITY_HIGH;
    sConfigOC.OCFastMode = TIM_OCFAST_ENABLE;
    if (HAL_TIM_PWM_ConfigChannel(&htim3, &sConfigOC, TIM_CHANNEL_1) != HAL_OK)
        {Error_Handler();}
    sConfigOC.Pulse = 750;
    sConfigOC.OCpolarity = TIM_OCPOLARITY_LOW;
    if (HAL_TIM_PWM_ConfigChannel(&htim3, &sConfigOC, TIM_CHANNEL_2) != HAL_OK)
        {Error_Handler();}
    HAL_TIM_MspPostInit(&htim3);
}

```

```

}

static void MX_GPIO_Init(void)
{
    GPIO_InitTypeDef GPIO_InitStruct = {0};

    /* GPIO Ports Clock Enable */
    __HAL_RCC_GPIOF_CLK_ENABLE();
    __HAL_RCC_GPIOA_CLK_ENABLE();
    __HAL_RCC_GPIOB_CLK_ENABLE();

    /*Configure GPIO pin Output Level */
    HAL_GPIO_WritePin(GPIOB, GPIO_PIN_0|GPIO_PIN_1, GPIO_PIN_RESET);

    /*Configure GPIO pins : PA1 PA2 PA3 PA5 */
    GPIO_InitStruct.Pin = GPIO_PIN_1|GPIO_PIN_2|GPIO_PIN_3|GPIO_PIN_5;
    GPIO_InitStruct.Mode = GPIO_MODE_INPUT;
    GPIO_InitStruct.Pull = GPIO_NOPULL;
    HAL_GPIO_Init(GPIOA, &GPIO_InitStruct);

    /*Configure GPIO pins : PB0 PB1 */
    GPIO_InitStruct.Pin = GPIO_PIN_0|GPIO_PIN_1;
    GPIO_InitStruct.Mode = GPIO_MODE_OUTPUT_PP;
    GPIO_InitStruct.Pull = GPIO_NOPULL;
    GPIO_InitStruct.Speed = GPIO_SPEED_FREQ_LOW;
    HAL_GPIO_Init(GPIOB, &GPIO_InitStruct);
}

void Error_Handler(void)
{
    __disable_irq();
    while (1){ }
}

#ifdef USE_FULL_ASSERT
void assert_failed(uint8_t *file, uint32_t line)
#endif
#endif

```

Listing 1: MCU C-code to drive the H-bridge.

List of Figures

1	Overview of flux sensing methods adopted from [7].	4
2	Schematic of saturation detection adopted from [7].	5
3	Schematic of dynamic flux measurement.	5
4	Basic transformer equivalent circuit.	6
5	Schematic of continuous flux sensing methods adopted from [7].	7
6	Schematic of orthogonal flux.	7
7	Schematic of hall effect sensor adopted from [18] and sensor application inside magnetic cores.	8
8	Schematic of magnetic ear adopted from [7].	9
9	Schematic representation of the voltage and field characteristics while the sensor experiences a constant external magnetic field H_{ext} , which leads to a magnetic flux B_{ext} inside the sensor rods.	11
10	Schematic representation of the voltage and field characteristics while the sensor experiences an alternating external magnetic field H_{ext} , which leads to a magnetic flux B_{ext} inside the sensor rods.	12
11	Magnetic flux line comparison between normal operation and saturated transformer core.	13
12	Geometric design of sensor core to achieve low reluctance R_m adopted from [7].	16
13	Two sensor rods with both windings.	17
14	Schematic five-leg transformer with flux sensor laying in one yoke.	18
15	Sensor design approach.	19
16	Nanocrystalline and ferrite core (dimensions in mm).	20
17	Schematic representation of the different material hysteresis curves.	21
18	Measured impedance spectrum of the used materials.	22
19	Schematic of excitation time $t_{\text{excitation}}$ and period time T_P	24
20	Sensor equivalent circuit.	26
21	Comparison between the time constants τ_{sensor} and τ_{sensor,R_1} in dependence of an additional resistor.	26
22	Rectangular and PWM produced sine signals.	27
23	H-bridge equivalent circuit.	28
24	Half bridge driver IR2104 [25].	29
25	Circuit of external crystal oscillator.	30
26	H-bridge excitation signals.	32
27	H-bridge supply voltage, supply- and pickup-current.	33
28	Hysteresis loop of the fluxgate sensor.	34
29	Nanocrystalline cross-section inclusive excitation coil (dimensions in mm). The datasheet can be found in Appendix B.1.	35

30	Magnetic circuit of transformer with sensor laying on the transformer yoke. . . .	35
31	Cross section of five-leg transformer with two two-layer windings (dimensions in mm). The inner coil is the low voltage and the outer the high voltage winding [30].	37
32	Synchronous demodulation: difference between sine and rectangle demodulation.	38
33	Schematic of signal processing.	39
34	Band pass filter 2 nd order.	39
35	Spice circuit of bandpass filters.	41
36	Simulated signal waveforms of bandpass filters.	42
37	Discharge switch circuit.	43
38	Top view of prototype PCB.	45
39	Prototype sensor setup.	45
40	Schematic of measurement setup with two transformers and a superimposed DC.	46
41	Schematic of SFRA measurement setup [32].	47
42	Hysteresis model of connected five- and three-leg transformers [10].	48
43	Superimposed DC ramp test.	49
44	Superimposed DC step.	50
45	Comparison between alternating flux through transformer yoke and sensor rod. .	51
46	Phase shift between two search coils, wound around transformer yoke and sensor rod.	52
47	Phase shift between induced voltages across the search coil around the transformer yoke and the search coil around one sensor rod.	52
48	Five-leg transformer with flux sensor in each yoke.	55
49	Magnetic flux paths inside five-leg transformer.	56
50	Schematic sensor control and signal processing with a FPGA.	57
A.1	Supply circuit.	58
A.2	H-Bridge circuit.	59
A.3	Signal processing circuit.	60
A.4	Symmetrical voltage supply circuit.	61
B.1	Data sheet of nanocrystalline oval core.	63

List of Tables

1	Properties of used materials for the fluxgate sensor from [20], [21] and Appendix B.1.	20
2	Comparison between the used materials, showing some significant points of the impedance spectrum.	23
3	Connected pins of STM32 Nucleo microcontroller.	30
4	Timer 1 and 2 settings on MCU.	31
5	Used components of prototype board.	62

References

- [1] J. Raith, “Risk assessment of power transformers under the influence of geomagnetically induced currents (gic),” PhD Thesis, TU Graz, Graz, 2019. [Online]. Available: <https://diglib.tugraz.at/risk-assessment-of-power-transformers-under-the-influence-of-geomagnetically-induced-currents-gic-2019>
- [2] R. S. Girgis and K. B. Vedante, “Impact of gics on power transformers: Overheating is not the real issue,” *IEEE Electrification Magazine*, vol. 3, no. 4, pp. 8–12, 2015.
- [3] C. T. Gaunt, “Reducing uncertainty – responses for electricity utilities to severe solar storms,” *Journal of Space Weather and Space Climate*, vol. 4, no. 4, p. A01, 2014.
- [4] Y. V. Afanassiev and G. Musmann, Eds., *Fluxgate magnetometers for space research*. Norderstedt: Books on Demand, 2010.
- [5] L. Bolduc, M. Granger, G. Pare, J. Saintonge, and L. Brophy, “Development of a dc current-blocking device for transformer neutrals,” *IEEE Transactions on Power Delivery*, vol. 20, no. 1, pp. 163–168, 2005.
- [6] H. Passath, G. Leber, P. Hamberger, and F. Bachinger, “Direct current compensation – field experience under service conditions,” *Journal of Energy - Energija*, vol. 63, no. 1-4, pp. 3–12, 2014.
- [7] G. Ortiz, L. Fassler, J. W. Kolar, and O. Apeldoorn, “Flux balancing of isolation transformers and application of “the magnetic ear” for closed-loop volt-second compensation,” *IEEE Transactions on Power Electronics*, vol. 29, no. 8, pp. 4078–4090, 2014.
- [8] J. Cao, S. Cheng, and R. Khan, “Online detection approach for direct current flux of power transformer,” *Electronics Letters*, vol. 53, no. 22, pp. 1489–1491, 2017.
- [9] P. Schachinger, D. Albert, and H. Renner, “Low frequency currents source identification,” in *2022 20th International Conference on Harmonics & Quality of Power (ICHQP)*, IEEE, Ed. IEEE, 2022, pp. 1–6.
- [10] D. Albert, *Analysis of Power Transformers under DC/GIC Bias*. Verlag der Technischen Universität Graz, 2023.
- [11] X. Chen, Z. Wang, and B. Wang, “Research on dynamic magnetic flux measurement under dc-biased magnetization by the type-c transducer,” *IEEE Magnetics Conference INTERMAG*, p. 1, 2015.
- [12] D. Wilson, “A new pulsewidth modulation method inherently maintains output transformer flux balance,” *International Solid-State Power Electronics Conference*, pp.

- pp. 27–30, 1981. [Online]. Available: https://jglobal.jst.go.jp/en/detail?JGLOBAL_ID=200902030980370702
- [13] J. A. Melkebeek, *Electrical machines and drives: Fundamentals and advanced modelling / Jan A. Melkebeek*, ser. Power systems. Cham, Switzerland: Springer, 2018.
- [14] Alexander Gertsman and Sam Ben-Yaakov, “Zeroing transformer’s dc current in resonant converters with no series capacitors,” *2010 IEEE Energy Conversion Congress and Exposition*, pp. 4028–4034, 2010. [Online]. Available: https://www.researchgate.net/publication/224188430_Zeroing_Transformer%27s_DC_Current_in_Resonant_Converters_with_No_Series_Capacitors
- [15] Franz Stögerer Johann W. and Kolar Uwe Drogenik, “A novel concept for transformer volt second balancing of a vienna rectifier iii based on direct magnetizing current measurement,” *Proceedings of the IEEE Nordic Workshop on Power and Industrial Electronics*, pp. 134–140, 2000. [Online]. Available: <https://www.semanticscholar.org/paper/A-Novel-Concept-for-Transformer-Volt-Second-of-a-on-Drogenik/6a38e6524c12877ebdb71a14d1d48c72905c253b>
- [16] Policka W. M., Cucconi A., Cuk S., “Detection of magnetic saturations in switching converters.” *Proc. Power Conver. Int. Conf.*, pp. 584–597, 1982.
- [17] A. Aganza-Torres, J. Pfeiffer, and P. Zacharias, “Interleaved buck converter with coupled inductors as auxiliary bias-current source for controllable magnetic devices,” in *PCIM Europe digital days 2020; International Exhibition and Conference for Power Electronics, Intelligent Motion, Renewable Energy and Energy Management*, 2020, pp. 1–8.
- [18] U. Tietze, C. Schenk, and E. Gamm, *Halbleiter-Schaltungstechnik*, 15th ed. Berlin [u.a.]: Springer Vieweg, 2016.
- [19] P. Hamberger, G. Leber, H. Passath, H. Pregartner, and A.-K. Schrammel, “Messanordnung zum erfassen eines magnetischen gleichflusses im kern eines transformators,” Patent EP 2 952 997 B1, 2017. [Online]. Available: <https://patentimages.storage.googleapis.com/ee/b4/e8/c743062828b620/EP2952997B1.pdf>
- [20] TDK Electronics AG, “Ferrites and accessories: U 101/76/30 core b67370.” [Online]. Available: https://product.tdk.com/system/files/dam/doc/product/ferrite/ferrite/ferrite-core/data_sheet/80/db/fer/u_101_76_30.pdf
- [21] D. Pöss Hans-Joachim, “Kristalline musterkerne: Mail,” 14.09.2022.
- [22] G. Kapp, *Transformatoren für Wechselstrom und Drehstrom: Eine Darstellung ihrer Theorie, Konstruktion und Anwendung*. Berlin, Heidelberg: Springer Berlin Heidelberg and Imprint and Springer, 1907.

- [23] J. Specovius, *Grundkurs Leistungselektronik: Bauelemente, Schaltungen und Systeme*, 5th ed., ser. Studium. Wiesbaden: Vieweg+Teubner Verlag and Imprint, 2011. [Online]. Available: <https://link.springer.com/content/pdf/10.1007%2F978-3-8348-8270-7.pdf>
- [24] Texas Instruments Incorporated, “Bootstrap circuitry selection for half-bridge configurations.”
- [25] Infineon Technologies Americas Corp., “Irfb4620pbf: Hexfet power mosfet,” 2008. [Online]. Available: <https://www.infineon.com/dgdl/irfb4620pbf.pdf?fileId=5546d462533600a401535616630a1e44>
- [26] Qantek Technology Corporation, “Qcl series: Hc-49/u-s,” 2023. [Online]. Available: https://www.qantek.com/tl_files/products/crystals/QCL.pdf
- [27] STMicroelectronics, “An2867 application note: Oscillator design guide for stm8af/al/s, stm32 mcus and mpus,” 2023. [Online]. Available: https://www.st.com/resource/en/application_note/cd00221665-oscillator-design-guide-for-stm8afals-stm32-mcus-and-mpus-stmicroelectronics.pdf
- [28] —, “An4013 application note: Stm32 cross-series timer overview,” 2023.
- [29] Stalprodukt S.A., “Electrical steels: Et_110-30_ls,” 2022. [Online]. Available: http://www.stalprodukt.com.pl/wp-content/uploads/2023/01/ET_110-30_LS.pdf
- [30] D. Albert, “5-Schenkel Labortransformator: Projekt: Nf-Sternpunkt 2, Internal Report.”
- [31] A. Fröhlich, “Versuchsaufbau zur präzisen Messung von Transformatorsternpunktströmen,” Bachelorarbeit, Graz University of Technology, Graz, 11.2021.
- [32] M. A. Habibi, A. A. Zain, F. A. P. Sudarto, A. Kusumawardana, S. Wibawanto, L. Gumilar, and H. Wicaksono, “The study of sweep frequency response analysis for inspecting the performance of transformer,” *Journal of Physics: Conference Series*, vol. 1595, no. 1, p. 012016, 2020.